Advanced Techniques In Clutter Mitigation And Calibration For Weather Radars

Yin, Jiapeng

DOI
10.4233/uuid:b70159a0-bc30-4889-8421-ba965885bcab

Publication date
2019

Document Version
Final published version

Citation (APA)
Yin, J. (2019). *Advanced Techniques In Clutter Mitigation And Calibration For Weather Radars*. [Dissertation (TU Delft), Delft University of Technology]. https://doi.org/10.4233/uuid:b70159a0-bc30-4889-8421-ba965885bcab

Advanced Techniques in Clutter Mitigation and Calibration for Weather Radars

ADVANCED TECHNIQUES IN CLUTTER MITIGATION AND CALIBRATION FOR WEATHER RADARS

Dissertation

for the purpose of obtaining the degree of doctor
at Delft University of Technology,
by the authority of the Rector Magnificus, prof. dr. ir. T.H.J.J. van der Hagen,
chair of the Board for Doctorates,
to be defended publicly on
Tuesday 28 May 2019 at 15:00 o'clock

by

Jiapeng YIN

Bachelor of Science in Information Engineering,
National University of Defense Technology, Changsha, China,
born in Wenzhou, Zhejiang, China.

This dissertation has been approved by the promotor.

Composition of the doctoral committee:

Rector Magnificus,	chairperson
Prof. dr. ir. H.J.W. Russchenberg,	Delft University of Technology, promotor
Independent members:	
Prof. dr. A.G. Yarovoy,	Delft University of Technology
Prof. dr. ir. G.J.T Leus,	Delft University of Technology
Prof. dr. V. Chandrasekar,	Colorado State University, USA
Dr. M. Haeffelin,	Ecole Polytechnique, France
Dr. H. Leijnse,	Royal Netherlands Meteorological Institute
Other members:	
Prof. ir. P. Hoogeboom,	Delft University of Technology
Prof. dr. ir. R.F. Hanssen,	Delft University of Technology, reserve member

Ir. C. M. H. Unal has contributed significantly to the preparation of this dissertation.

Keywords: weather radar, radar polarimetry, spectral polarimetry, clutter mitigation, radar calibration

Printed by: ProefschriftMaken

Cover design: byscene.com

ISBN 978-94-6380-365-6
Dissertation at Delft University of Technology
Advanced Techniques in Clutter Mitigation and Calibration for Weather Radars

An electronic version of this dissertation is available at
http://repository.tudelft.nl/.

To my family

CONTENTS

SUMMARY

Weather observation is becoming more important than ever because extreme weather, such as tropical cyclones, thunderstorms and heavy rain, is more common nowadays. To observe and forecast the atmospheric phenomena at high spatial and temporal resolution, weather radar is well recognized as an effective tool. The prerequisite of using weather radar data is sufficient measurement accuracy. The focus of this thesis is to propose advanced techniques in clutter mitigation and calibration for weather radars to improve radar measurement accuracy.

To separate radar target and moving clutter, a novel technique based on a combination of the low-rank matrix optimization (LRMO) and a decision tree is introduced in Chapter 2. Making use of different motion variation of radar target and clutter in the range-Doppler spectrogram sequence, the proposed separation method can be very general. In this chapter, it is specifically designed for narrow-band moving clutter suppression in weather radar. This is the first time LRMO has been introduced in the context of weather radar clutter mitigation. In addition, LRMO does not require the polarimetric measurements of weather radar, making the single-polarization clutter mitigation technique broadly applicable.

The technique described in Chapter 2 can remove moving narrow-band clutter and keep weak precipitation, but it is computationally expensive, which makes it difficult to implement in real-time. Observed in the Doppler domain, the narrow-band clutter includes: 1) stationary clutter such as ground clutter and 2) nonstationary clutter such as artifacts caused by the radar system itself or external sources. These artifacts are difficult to remove, because they are not confined to specific azimuth and range bins. To develop a real-time technique which can mitigate the narrow-band clutter, Chapter 3 introduces a new clutter suppression method named the moving double spectral linear depolarization ratio (MDsLDR) filter for full-polarimetric weather radar. Taking advantage of the difference of the spectral polarimetric features and spectral continuity of precipitation and clutter, the MDsLDR filter generates a filtering mask implementing on the range-Doppler spectrogram to remove the clutter and noise, and keep the precipitation.

The technique described in Chapter 3 can only be used in polarimetric weather radar with cross-polar measurements. For application to dual-polarization radar systems, Chapter 4 introduces one filter named the object-orientated spectral polarimetric (OBSpol) filter to remove the same clutter mentioned in Chapter 3. Based on the spectral polarimetric features and spectral continuity of precipitation and clutter, the OBSpol filter generates a filtering mask implementing on the range-Doppler spectrogram to remove the clutter. Due to the more advanced signal processing method used in the OBSpol filter design, it can achieve good clutter mitigation performance and keep weaker precipitation.

Chapter 3 and Chapter 4 describe the real-time clutter mitigation techniques which are specifically designed for narrow-band clutter removal for polarimetric weather radar.

Chapter 5 extends the application of the mentioned clutter mitigation techniques to the radio frequency interference (RFI). Observed in the spectral domain, RFI are broad-band clutter, acting as additional noise over the whole spectra. In this chapter, RFI mitigation techniques for polarimetric weather radar with and without cross-polar measurements are presented.

From Chapter 2 to Chapter 5, the clutter mitigation methods are discussed, with which we are expecting to obtain "clean" precipitation measurements. However, for weather radar applications, it is also important to quantitatively get the "correct" precipitation estimation. The novel radar calibration technique presented in Chapter 6 is for the purpose. The unmanned aerial vehicle (UAV) aided radar calibration technique is a general method which can adapt to different radar systems.

SAMENVATTING

Weermetingen worden steeds belangrijker door de toename van extreme weersituaties zoals tropische cyclonen, onweersbuien en hevige neerslag. Voor de observatie en voorspelling van deze weersverschijnselen op hoge ruimtelijke en temporele resolutie is de weerradar een gangbaar en effectief middel. Een belangrijke voorwaarde voor het gebruik van weerradar data is echter dat de nauwkeurigheid van de meting goed genoeg is. De focus van dit proefschrift is om geavanceerde technieken te ontwikkelen voor het filteren en calibreren van weerradar data om meetruis te onderdrukken en de nauwkeurigheid van de radar meting te verbeteren.

Om het radardoel en bewegingsruis te splitsen, is er een nieuwe techniek ontwikkeld gebaseerd op low-rank matrix optimalisatie (LRMO) en een beslissingsboom, die word geïntroduceerd in hoofdstuk 2. Door gebruik te maken van het verschil in bewegingsverandering tussen het radardoel en de ruis in de range-Doppler spectrogram series is deze methode breed toepasbaar. Dit onderzoek is de eerste dat de LRMO techniek wordt toegepast voor het onderdrukken van ruis in weerradars. Daarnaast is er geen polarimetrische data nodig voor LRMO, wat een brede toepassing van ruisonderdrukking voor weerradars met enkele polarisatie mogelijk maakt.

De techniek beschreven in hoofdstuk 2 kan bewegende ruis over een kleine bandbreedte verwijderen en lichte neerslag behouden, maar het vraagt veel rekenkracht, waardoor het lastig is om het real-time te gebruiken. De ruis over een kleine bandbreedte in het Doppler domein bestaat onder andere uit de volgende componenten: 1) stationaire ruis door objecten op de grond en 2) niet-stationaire ruis vanwege effecten die veroorzaakt worden door het radarsysteem zelf of externe factoren. Deze effecten zijn lastig te verwijderen omdat ze zich niet binnen een bepaalde range van azimuthintervallen bevinden. Om een real-time techniek te ontwikkelen om ruis over een kleine banbreedte te onderdrukken, introduceren we in Hoofdstuk 3 een nieuwe methode om ruis te onderdrukken, het bewegende dubbel spectraal lineaire depolarisatie ratio (MDsLDR) filter voor volledige polarimetrische weerradars. Door gebruik te maken van de spectraal polarimetrische eigenschappen en spectrale continuiteit van neerslag en ruis creëert het MDsLDR algoritme een filter voor het range-Doppler spectrogram om ruis en het neerslag signaal te scheiden.

De techniek beschreven in Hoofdstuk 3 kan alleen gebruikt worden in polarimetrische weerradars met cross-polar metingen. Voor tweevoudig gepolariseerde radar systemen introduceren we in hoofdstuk 4 een ander filter, het object georienteerde spectraal-polarimetrische (OBSpol) filter om dezelfde ruis te verwijderen als in Hoofdstuk 3. Gebaseerd op de spectraal-polarimetrische eigenschappen en spectrale continuiteit van neerslag en ruis, creëert het OBSpol algorithme een filter voor het range-Dopple spectrogram om ruis te verwijderen. Door de meer geavanceerde methode voor signaalverwerking in het OBSpol filter kan het goed de ruis verwijderen en lichte neerslag behouden.

Hoofdstuk 3 en 4 beschrijven de real-time ruis-reductietechnieken die specifiek ontworpen zijn voor het verwijderen van ruis over een kleine bandbreedte voor een polarimetrische weerradar. Hoofdstuk 5 breidt de toepassing van de genoemde ruis-reductietechnieken uit naar de radio frequency interferentie (RFI). Vanuit het spectrale domein bezien is RFI breedband ruis, dat ruis veroorzaakt over het hele spectrum. In Hoofdstuk 5 worden verschillende RFI technieken besproken voor ruisonderdrukking van polarimetrische radars met en zonder cross-polair metingen.

Van hoofdstuk 2 tot 5 zijn verschillende methoden besproken om ruis te onderdrukken, die naar verwachting 'schone' neerslag metingen zullen opleveren. Voor weerradar toepassingen is het echter ook belangrijk om de juiste kwantitatieve waarden voor neerslag te benaderen. De nieuw ontwikkelde techniek die in Hoofdstuk 6 gepresenteerd wordt, is met dat doel ontwikkeld. Deze radar-kalibratietechniek die gebruik maakt van UAV's is een algemene methode die werkt voor verschillende radarsystemen.

1

INTRODUCTION

1.1. BACKGROUND

Climate change is becoming one of the largest challenges of mankind. As so often nowadays, floods and storms bring in disasters with great harms to the society, which has aroused amounting concern, especially in the urban areas (Douglas *et al.*, 2008). For example, the medium and large-sized cities of Asia are undergoing rapid growth, but they are unable to develop a sustainable method to deal with the urban floods. The reason behind these disasters is the extremely intense precipitation, with rainfall intensities typically higher than 20 mm/h and time duration for a few hours. Hence, rainfall information is a critical component to effectively monitor and forecast this type of disastrous weather (Cannon *et al.*, 2008). To observe and forecast such atmospheric phenomena at high spatial and temporal resolution, weather radar is well recognized as an effective tool (Morin *et al.*, 2003).

The prerequisite of using weather radar data is sufficient measurement accuracy. The primary error source of radar data derives from unwanted echoes, termed as "clutter" (Skolnik, 1970). The radar environment is so complicated that it contains different types of clutter, such as ground clutter, insects and birds, radio frequency interference, wind turbine clutter and radar artifacts generated from radar system itself etc.. This clutter significantly affects both the quality of the measurement and the observation of precipitation areas. Specifically, the presence of clutter may lead to weather signals undetected or introduce bias on radar measurements (Bringi and Chandrasekar, 2001). Hence, it is important to find a way to mitigate all the unwanted echoes.

In addition, the radar system bias, which may come from any radar component, will add inestimable uncertainty in radar measurements. The system bias should be quantified, and this process is named "calibration" (Atlas, 2002). Current calibration methods either use a metal sphere hanging underneath a tethered balloon (Williams *et al.*, 2013) or a trihedral corner reflector locating on the top of a tower or mast (Bharadwaj *et al.*, 2013). However, there are some problems with these methods: (1) They are location bound. The calibrator should be placed in the far-field, which seems impossible

1

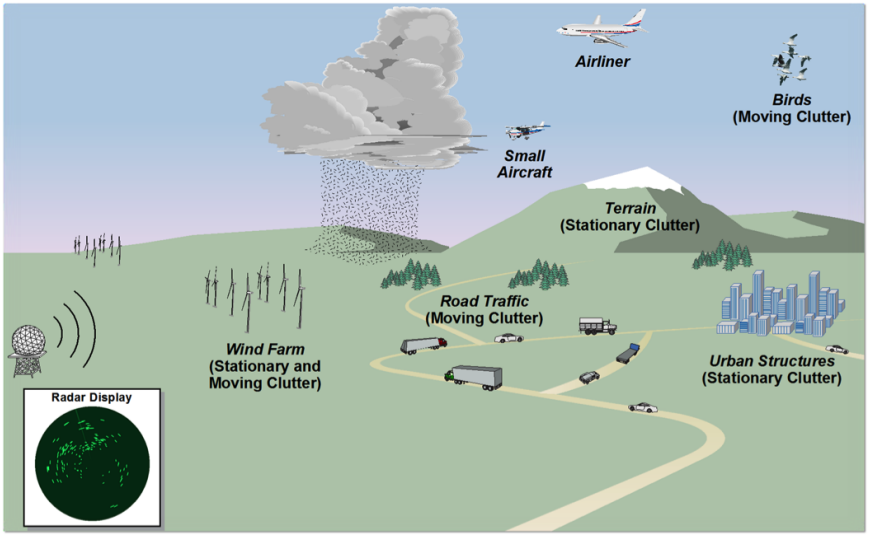

Figure 1.1: A schematic illustration of weather radar clutter. Picture is taken from https://www.windpowereng ineering.com/policy/teaching-wind-turbines-radar-play-nice/, under the "fair use" clause for research purposes.

for some radars located on the top of high buildings or towers. (2) It is relatively costly for tower setup or helium balloon purchase. (3) It is not easy to repeat the calibration process for mobile radars, especially for some fieldwork campaigns in complex terrain. (4) For vertically pointing cloud radars, the current methods cannot be used to calibrate them. Based on the aforementioned reasons, a portable, cost-effective and repeatable solution to replace the current calibration techniques is highly demanded.

To obtain effective information about microphysical properties of meteorological scatterer, such as the size, shape, and orientation, upgrading weather radar to polarimetric measurement capability is more desirable (Zhang, 2016). The information obtained by the polarimetric weather radar can be used for further application, such as improving warnings (Stensrud *et al.*, 2009), short-term forecasts (Dixon and Wiener, 1993), and quantitative precipitation estimation (Wang and Chandrasekar, 2010). Upgrading from single-polarization to dual-polarization, it will no doubt increase radar system complication because of the addition of another radar receiver. Polarimetric weather radar can be divided into dual-polarization radar and full-polarimetric radar based on the availability of cross-polar measurements. To guarantee the radar measurement accuracy, the corresponding techniques in clutter mitigation and calibration should be developed.

This dissertation investigates the advanced techniques in clutter mitigation and calibration for weather radar to improve radar measurement accuracy. On the one hand, clutter mitigation techniques for signal-polarization, dual-polarization without cross-polar measurements and full-polarimetric radar systems are proposed to mitigate different types of clutter. On the other hand, a novel radar calibration technique is developed. With clutter suppression and techniques, clean and correct weather radar measurements are expected to be obtained.

1.2. RESEARCH OBJECTIVE AND QUESTIONS

This dissertation aims to develop advanced techniques in clutter mitigation and calibration for weather radars to improve radar measurement accuracy. To achieve these objectives, the following research questions will be addressed:

(1) How can narrow-band moving clutter be mitigated in single-polarization weather radars?

(2) How can narrow-band moving clutter be mitigated in real-time in full-polarimetric weather radars?

(3) How can narrow-band moving clutter be mitigated in real-time in dual-polarization weather radars without cross-polar measurements?

(4) How can radio frequency interference be mitigated in real-time in polarimetric weather radars?

(5) How to improve calibration for weather radar systems that have fixed locations (e.g., in high tower) or fixed beams (e.g., vertically pointing cloud radars and slantwise pointing research radars)?

1.3. OUTLINE OF THE DISSERTATION

The dissertation contains 7 chapters and the schematic diagram of the structure is displayed in Table 1.1. From this table, we learn that the dissertation mainly investigates two aspects, namely clutter mitigation technique and calibration technique. In the category of clutter mitigation technique, different techniques are proposed to mitigate different types of clutter in different radar systems. In this table, clutter types are listed as 4 types and the applicability of each mitigation technique in filtering different clutter types is also given. As for the calibration aspect, a general technique is proposed for all types of weather radar systems.

Table 1.1: The schematic diagram of the dissertation structure. The filtering clutter types contain: 1. Narrow-band moving artifacts; 2. Ground clutter; 3. Noise; 4. Radio frequency interference.

Clutter Mitigation Technique					**Calibration technique**
Radar system	Single-polarization	Full-polarimetric	Dual-polarization	Polarimetric	UAV-aided technique (**Chapter 6**)
Name	LRMO (**Chapter 2**)	MDsLDR (**Chapter 3**)	OBSpol (**Chapter 4**)	MDsLDR OBSpol (**Chapter 5**)	
Filtering clutter types	1, 3	1, 2, 3	1, 2, 3	3, 4	

Chapter 2, 3, 4 and 5 focus on clutter mitigation and all the processing is conducted in the spectral domain. The terms “narrow-band” refers to spectral width. Chapter 2 presents a technique for single-polarization weather radar to mitigate narrow-band moving clutter and noise. Chapter 3 proposes a technique for full-polarimetric weather radar to remove narrow-band clutter (i.e., ground clutter and narrow-band moving clutter) and noise. Mitigating the same clutter, Chapter 4 addresses a technique for dual-polarization weather radar without cross-polar measurements. Extending the filter application in narrow-band clutter mitigation, Chapter 5 discusses the application of the proposed techniques in radio frequency interference. Chapter 6 presents the UAV-aided calibration technique. Finally, Chapter 7 concludes the dissertation with the main contributions and directions for future research.

2

Radar Target and Moving Clutter Separation based on the Low-rank Matrix Optimization

---

This chapter has been published as:

Jiapeng Yin, Christine Unal, Marc Schleiss and Herman Russchenberg. "Radar Target and Moving Clutter Separation based on the Low-rank Matrix Optimization", *IEEE Trans. Geosci. Remote Sens.*, 56(8):4765-4780, 2018.

To separate radar target and moving clutter, a novel technique based on a combination of the low-rank matrix optimization (LRMO) and a decision tree is introduced. Making use of different motion variation of radar target and clutter in the range-Doppler spectrogram sequence, the proposed separation method can be very general. In this chapter, it is specifically designed for narrow-band moving clutter suppression in weather radar. This is the first time LRMO has been introduced in the context of weather radar clutter mitigation. In addition, LRMO does not require the polarimetric measurements of weather radar, making the single-polarization clutter mitigation technique broadly applicable.

Except the introduction is given in Section 2.1, the reminder of this chapter is organized as follows. In Section 2.2, the details of the proposed method are provided, including the range-Doppler spectrogram sequence generation and the optimization method. Further, the LRMO technique is applied to weather radar data in Section 2.3. Specifically,

the IDRA artifacts are introduced, the detail procedures of the technique are discussed, and a decision tree is designed to produce the filtering mask. In addition, parameters for the decision tree and the spectrogram sequence are selected. In Section 2.4, the performance verification and parameter sensitivity analysis are given. Finally, Section 2.5 draws the conclusions and discusses some other potential application of this technique.

2.1. INTRODUCTION

Radar, as an effective remote sensing platform, is designed to detect and track targets using electromagnetic waves (Skolnik, 1970). According to different targets of interest and applications, radar is configured with various waveforms, wavelengths, scanning strategies, etc.. Radar clutter, which is defined as an interfering radar echo from other objects (Eaves and Reedy, 2012), is a relative concept for different radar systems. For instance, air traffic control radar (Nolan, 2010) and marine radar (Briggs, 2004) regard vehicles (e.g., airplanes and ships) as targets and precipitation as clutter. While for weather radar (Bringi and Chandrasekar, 2001), the opposite is the case.

Sometimes, "clutter" may also be valuable. One example is the Doppler weather surveillance radar network (WSR-88D) also known as NEXRAD which consists of 159 high-resolution S-band polarimetric Doppler weather radars (Crum and Alberty, 1993). The primary function of NEXRAD is to detect and track precipitation and help predict the atmospheric threats to life and property. So precipitation will be the target for NEXRAD. However, using the same radar system, ornithologists can also track bird echoes and conduct studies about bird migration (Stepanian *et al.*, 2016). Hence, for multi-functional radar systems, target and clutter separation techniques may be more compelling than clutter mitigation. Indeed, with proper radar target and clutter separation, clutter mitigation is normally easily fulfilled. Another benefit of target and clutter separation is radar target feature extraction. For example, fuzzy logic algorithms, which can reach distinct decisions based on overlapping or "noise contaminated" measurements, are widely used for hydrometeor classification in weather radar (Liu and Chandrasekar, 2000). The performance of fuzzy-logic-based classification largely depends on the hydrometeor feature extraction which is time-consuming for manual selection. Last but not least, when signal and clutter overlap, such as precipitation buried by wind turbine clutter (Uysal *et al.*, 2016), good separation techniques are needed to retrieve the target signal. Apart from precipitation, vehicles, birds, and wind turbines, other echoes from buildings, moving sea waves, and changeable radio frequency interference, can also be sensed by radar.

This paper focuses on weather radar. The weather radar clutter, which significantly affects both the quality of the measurement and the observation of targets, can be divided into stationary and non-stationary clutter according to their Doppler velocity. Methods of stationary clutter (e.g., ground clutter) mitigation can mainly be divided into two types, namely the time-domain and the Doppler-domain methods. Regression filters (Torres and Zrnic, 1999) in the temporal domain and the Gaussian model adaptive processing (GMAP) (Siggia and Passarelli Jr, 2004) in the spectral domain, are specifically designed to remove the clutter centered around $0\,\mathrm{m\,s^{-1}}$. However, when these techniques are applied to radar data not contaminated by ground clutter, this will lead to signal loss. Hence, proper clutter detection algorithm should be implemented before clutter filtering. Recently, the Clutter Environment Analysis using Adaptive Processing (CLEAN-AP),

which is based on the phase of the auto-correlation spectral density, has been proposed (Warde and Torres, 2014). CLEAN-AP integrates clutter detection and filtering in one algorithm, and this filter uses both magnitude and phase for improved notch width determination that results in smaller biases. Further, it has a better clutter suppression performance, and the variance of estimates is reduced (Torres *et al.*, 2012). However, while CLEAN-AP can deal with normal-propagation (NP) and anomalous-propagation (AP) clutter, it is not a mitigation technique for moving clutter such as airplanes, ships, cars or wind turbines.

Non-stationary clutter has also attracted a lot of interest in the past years. The characteristics of birds and insects are presented by Stepanian and Horton (2015); Zrnic and Ryzhkov (1998); Melnikov *et al.* (2014, 2015). Besides, Alku *et al.* (2015) demonstrates the effectiveness of the image processing techniques together with the fuzzy logic algorithm to mitigate other clutter, such as sea and chaff clutter. Wind turbine clutter (WTC) is both stationary and non-stationary. It significantly deteriorates radar system performance because of the large-intensity back-scattering from the tower and the moving blades (Yin *et al.*, 2017a). The undesirable effect of WTC on weather radar is illustrated by Isom *et al.* (2009); Norin and Haase (2012), on air traffic control radar by Webster (2005), and on marine radar by Rashid and Brown (2007). Methods such as interpolation (Kong *et al.*, 2012; Nai *et al.*, 2013), signal decomposition (Uysal *et al.*, 2014, 2016) and machine learning (Nepal *et al.*, 2015), have been investigated to mitigate the WTC. Last but not least, radio frequency interference (RFI) arising from the Radio Local Area Network (RLAN) is an increasing concern for the radar community, for example, the C-band European operational weather radar network (EUMETNET/OPERA Radar Network) (Huuskonen *et al.*, 2014). Disturbances, such as dots, spokes and spikes, are brought in the radar plan position indicator (PPI) by RFI, which severely lowers the quality of radar data (Saltikoff *et al.*, 2016). Comparably, artifacts caused by the radar system itself also affect the usage of radar data (Yin *et al.*, 2017b, 2019). Most of the time, artifacts are speckles along the whole range bins in some azimuth directions in the PPI. Moreover, these speckles are non-stationary when observed in the Doppler domain, making it impossible to mitigate them with conventional clutter suppression methods. These artifacts affect not only the reflectivity but also the Doppler and polarimetric measurements. For example, artifacts have been shown to influence the display of the polarimetric Doppler X-band radar IRCTR Drizzle Radar (IDRA) since its installation in 2007. Also, the high-resolution polarimetric Doppler X-band radar MESEWI suffers from an analogous problem (Krasnov and Yarovoy, 2016). So do the Bonn X-band radar systems. Yin *et al.* (2016) puts forward a polarimetric optimization (POLO) method to remove the artifacts in IDRA. This technique can improve the suppression of the clutter while keeping most of the precipitation. However, it cannot completely mitigate all artifacts, and will lose weak signals below -2 dBZ. Therefore, drizzle measurements may be suppressed.

Taking advantage of the different motion variation of radar target and clutter in the spectrogram sequence, we propose a novel algorithm to separate radar target and moving clutter based on the low-rank representation. The low-rank matrix optimization (LRMO) (Liu *et al.*, 2013) has been successfully adopted in many applications, such as video denoising (Ji *et al.*, 2010), keyword extraction (Min *et al.*, 2010), image alignment (Peng *et al.*, 2012) and automated video analysis (Zhou *et al.*, 2013). Additionally, the

low-rank representation has been used to suppress in-wall clutter for through-the-wall radar (Zhang and Xia, 2016). However, it has never been used for weather radar target and moving clutter separation. The proposed technique can be used in different radar systems as long as radar target and clutter have different motion properties in the spectrogram sequence.

2.2. LOW-RANK MATRIX OPTIMIZATION IN RADAR

This section discusses the details of how to implement the proposed radar target and moving clutter separation method. The technique is mainly based on different motion behavior of target and clutter in the range-Doppler spectrogram sequence. The rationale for using the range-Doppler spectrograms is that they integrate both range and velocity information (including both the radial Doppler velocity and its change), which are normally different for radar target and clutter. This makes it easier to distinguish between them. However, the trade-off is the difficulty of implementation. This is where the LRMO technique comes into play. In the framework of the LRMO, the separation between radar target and moving clutter can be represented as the problem of detecting contiguous outliers in the low-rank representation. The separation implementation will be accomplished on a range-Doppler spectrogram sequence. In this case, radar target can be seen as the foreground while moving clutter will represent the background which has nonzero Doppler velocity but is relatively fixed at the same Doppler velocity in the spectrogram sequence. More details will be given in the clutter analysis section.

2.2.1. SPECTROGRAM SEQUENCE GENERATION

Suppose that the radar transmits a coherent burst of P pulses as

$$s_T(t) = \sum_{p=0}^{P-1} x(t - pT_r) \cdot e^{j2\pi f_c t} \tag{2.1}$$

where t is the time, $x(t)$ is the complex envelope of one pulse, T_r is the pulse repetition interval (PRI), and f_c is the center frequency. Correspondingly, the received echo can be expressed as

$$s_R(t) = a \cdot s_T[t - \tau(t)] = a \cdot s_T\left[t - (\tau_0 - \frac{2v}{c}t)\right] \tag{2.2}$$

where a is the attenuated amplitude, $\tau(t)$ is the round-trip time delay, $\tau_0 = \frac{2R_0}{c}$ is the initial time delay, R_0 is the initial range of the target, c is the speed of light, and v is the target Doppler velocity. Substituting Eq. (2.1) into Eq. (2.2), we get

$$s_R(t) = \tilde{a} \cdot \sum_{p=0}^{P-1} x[(1 + \frac{2v}{c})t - \tau_0 - pT_r] \cdot e^{j2\pi f_c(1+\frac{2v}{c})t} \tag{2.3}$$

where the constant phase term $e^{-j2\pi f_c \tau_0}$ is included in the complex amplitude $\tilde{a} = a \cdot e^{-j2\pi f_c \tau_0}$. By introducing the fast-time $t_f = t - pT_r$ in Eq. (2.3) and demodulating into base-band, the signal is expressed as

$$s_R(t_f, p) = \tilde{a} \cdot x[(1 + \frac{2v}{c})t_f - \tau_0 + \frac{2v}{c}pT_r] \cdot e^{j2\pi f_c \frac{2v}{c}(t_f + pT_r)} \tag{2.4}$$

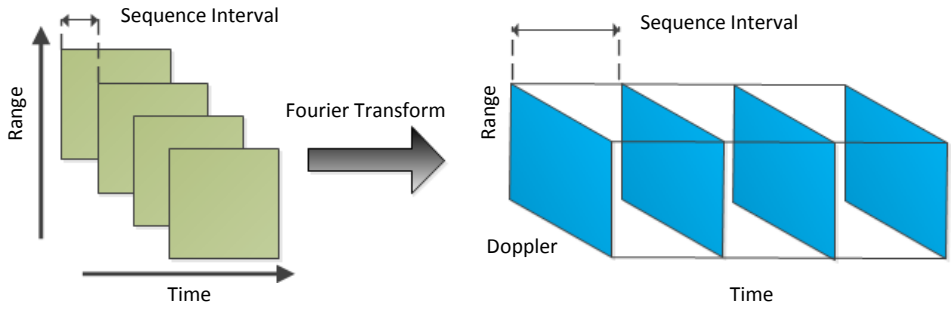

Figure 2.1: The schematic diagram of the range-Doppler spectrogram sequence generation.

In radar, target velocity is assumed to be constant in one pulse duration T_r and we have $vT_r \ll \Delta R$, where ΔR is the range resolution. This means that the Doppler effect in the fast-time and the contribution of $\frac{2v}{c} t_f$ in the amplitude are negligible, thus removing the term $\frac{2v}{c} t_f$, Eq. (2.4) can be expressed as

$$s_R(t_f, p) = \tilde{a} \cdot x(t_f - \tau_0 + \frac{2v}{c} pT_r) \cdot e^{j2\pi f_c \frac{2v}{c} pT_r} \tag{2.5}$$

To simplify the derivation, replacing the discrete slow-time pT_r with t_s in (2.5), we have

$$s_R(t_f, t_s) = \tilde{a} \cdot x(t_f - \tau_0 + \frac{2v}{c} t_s) \cdot e^{j2\pi f_c \frac{2v}{c} t_s} \tag{2.6}$$

Then, applying the short time Fourier transform (STFT) over slow-time t_s in Eq. (2.6), we can obtain the range-Doppler spectrogram sequence as

$$X(t_f, f_d, n) = \left| STFT(s_R(t_f, t_s)) \right|^2 \tag{2.7}$$

where t_f relates with the range bin, and f_d represents the Doppler bin whose size is related to the STFT window length, and n represents the n^{th} frame of the spectrogram sequence.

Finally, discretizing the spectrogram sequence, we obtain $X(r, d, n) = [X_1, \cdots, X_N]$, where r, d and n represent the range bin, the Doppler bin and the sequence number, respectively. If the number of range bins is R, the number of Doppler bins is D, and the sequence number is N, we have $X \in \mathbb{R}^{Q \times N}$, where $Q = R \times D$.

The above process can be visualized via the schematic diagram in Fig. 2.1. Given one range-time data, we move forward and backward by L sequence interval in the slow-time to obtain N range-time data. Further, by the Fourier transform, N range-Doppler spectrograms are obtained. Next, the LRMO can be used to separate radar target from moving clutter based on the spectrogram sequence. The sequence interval L and the sequence number N are important parameters. Their selection is discussed in more details in Section 2.5.1.

2.2.2. LOW-RANK MATRIX OPTIMIZATION

In this paper, the capital letters representing numbers are cardinal and their lower-case formats are ordinal. The low-rank matrix optimization is employed in this paper, following the same notations as by Zhou *et al.* (2013). Assuming that $X_n \in \mathbb{R}^Q$ denotes the n^{th} frame of the range-Doppler spectrogram sequence, the q^{th} pixel in the n^{th} frame is denoted as qn. While $B = [B_1, \cdots, B_N] \in \mathbb{R}^{Q\times N}$ represents their corresponding background images and $S = [S_1, \cdots, S_N] \bullet \in \{0,1\}^{Q\times N}$ is a binary matrix denoting the foreground support:

$$S_{qn} = \begin{cases} 0, & \text{if } qn \text{ is background} \\ 1, & \text{if } qn \text{ is foreground} \end{cases} \tag{2.8}$$

$P_S(X)$ represents the orthogonal projection of a matrix X onto the linear space of matrices supported by S,

$$P_S(X)(q,n) = \begin{cases} 0, & \text{if } S_{qn} = 0 \\ X_{qn}, & \text{if } S_{qn} = 1 \end{cases} \tag{2.9}$$

and $P_{S^\perp}(X)$ is its complementary projection. Then we have $P_S(X) + P_{S^\perp}(X) = X$.

In the spectrogram sequence, we model radar target as the foreground areas, and moving clutter as the background. Background areas are relatively fixed among the produced spectrogram sequence, which means they are highly correlated with each other, forming a low-rank matrix B. This constraint on B can be expressed as

$$rank(B) \leq K \tag{2.10}$$

where K is a constant to be predefined.

The foreground areas, on the other hand, are defined as radar targets that move differently from the background. They act as the outliers in the low-rank representation. The binary states of entries in the foreground support S can be modeled by a Markov random field (Li, 2009). Considering a graph $G = (\nu, \epsilon)$, where ν is the set of vertices denoting all the pixels in the sequence and ϵ is the set of edges connecting neighboring pixels, and assuming that we have no additional prior knowledge about the locations of objects, the energy of S is given by the Ising model (Li, 2009) as

$$\beta \sum_{qn\in\nu} S_{qn} + \gamma \sum_{(qn,pm)\in\epsilon} \left|S_{qn} - S_{pm}\right| \tag{2.11}$$

where $\beta > 0$ represents the potential of S_{qn} being 0 or 1, and $\gamma > 0$ controls the strength of dependency between S_{qn} and S_{pm}.

Finally, we consider the signal model that describes the formation of X. On the one hand, in the foreground where $S_{qn} = 1$, X_{qn} equals to the foreground intensity and X_{qn} is not constrained. On the other hand, in the background where $S_{qn} = 0$, $X_{qn} = B_{qn} + \epsilon_{qn}$, where ϵ_{qn} denotes independent and identically distributed Gaussian noise. Thus, B_{qn} should be the best fit to X_{qn} in the least squares sense in this case.

Combining the above background, foreground and signal models, the objective function to estimate B and S is given by:

$$\begin{aligned} \underset{B,S_{qn}\in\{0,1\}}{min} \quad & \frac{1}{2} \sum_{qn:S_{qn}=0} \left(X_{qn} - B_{qn}\right)^2 + \beta \sum_{qn\in\nu} S_{qn} + \gamma \sum_{(qn,pm)\in\epsilon} \left|S_{qn} - S_{pm}\right| \\ \text{subject to} \quad & rank(B) \leq K. \end{aligned} \tag{2.12}$$

To make Eq. (2.12) tractable, the rank operator on B is relaxed with the nuclear norm (Recht *et al.*, 2010). Rewriting Eq. (2.12) in the dual form and with the matrix operators, we obtain the following problem:

$$\min_{B,S_{qn}\in\{0,1\}} \quad \frac{1}{2}\|P_{S^\perp}(X-B)\|_F^2+\alpha\|B\|_*+\beta\|S\|_1+\gamma\|A\cdot vec(S)\|_1 \tag{2.13}$$

where $\|\cdot\|_F$ is the Frobenius norm, $\|\cdot\|_*$ is the nuclear norm, $\|\cdot\|_1$ is the $\ell 1$ norm. A is the node-edge incidence matrix of G, and vec means the vectorization of matrix S. The parameter $\alpha>0$ relates with the background low-rank K. Actually, the parameters α, β and γ are the weights of background low-rank, foreground sparsity and foreground smoothness in the LRMO. To minimize the LRMO, they should be adjusted properly.

The objective of the optimization in Eq. (2.13) is to estimate B and S. For details about the estimation, we refer to Zhou *et al.* (2013). As for the selection of the parameters α, β and γ, it is also well discussed by Zhou *et al.* (2013), and they are set to the same values in this paper. Specifically, α is initialized to be the second largest singular value of X and is reduced by a factor $1/\sqrt{2}$ until $rank(B)>K$. A similar procedure is followed for β, starting at a relatively large value, and then reducing by a factor 0.5 after each iteration until β reaches $4.5\sigma^2$ where σ^2 is the estimated noise level calculated by the variance of $X-B$. Overall, only two parameters, i.e., K and γ need to be chosen. The optimization algorithm is empirically configured by setting $K=\lfloor\sqrt{N}\rfloor$ and $\gamma=5\beta$, where $\lfloor\cdot\rfloor$ means the lower integer part. The influence of K and γ on the LRMO performance will be discussed in Section 2.5.2.

2.3. APPLICATION TO WEATHER RADAR

In this section, the proposed method will be applied to the field of weather radar. Specifically, we will address the problem of artifacts contaminating the PPI of the polarimetric Doppler weather radar IRCTR Drizzle Radar (IDRA) documented by Figueras i Ventura (2009). The features of artifacts are firstly analyzed to show the necessity to separate artifacts from precipitation in IDRA. Further, the details of the LRMO applied to mitigate artifacts are discussed, including a general LRMO separation and a specific filtering mask design based on a decision tree. Finally, parameters for the decision tree and the spectrogram sequence are discussed.

2.3.1. CLUTTER ANALYSIS

The IDRA radar continuously scans the atmosphere, and its measurements are displayed in near-real time. IDRA rotates horizontally at a speed of 1 rpm with a fixed elevation angle 0.5°. The specifications of the polarimetric Doppler weather radar are shown in Table 2.1. All the radar data recorded from April 2009 until now are freely accessible to the public on the website named 4TU.centre for Research Data. These data provide a long-term observation to monitor the trends in precipitation change. The Doppler velocity resolution corresponds to 512 samples used for Doppler processing, and in this paper, 512 samples are kept for all the processing.

The raw PPI of one radar measurement at 02:00 UTC on 1st July 2011 is shown in Fig. 2.2(a). Artifacts whose intensity is larger than the background noise level on the PPI are

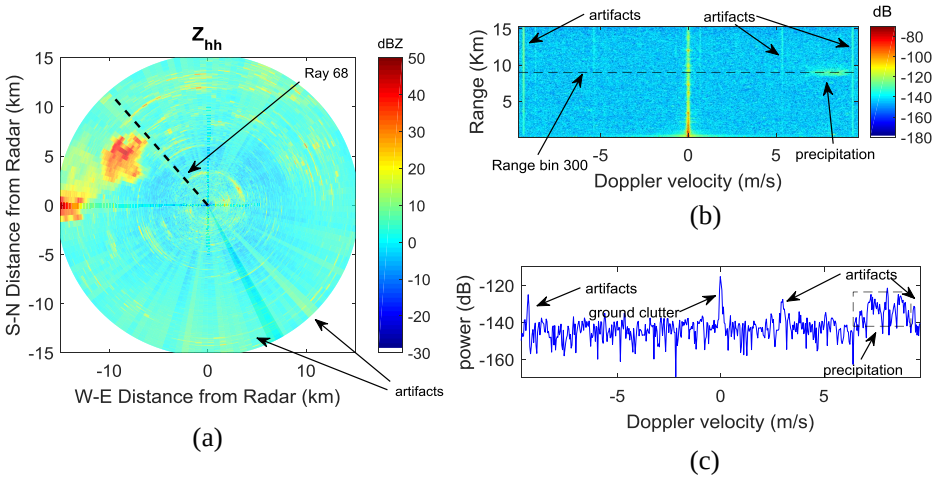

Figure 2.2: Radar artifact analysis. (a) Raw PPI. (b) Raw spectrogram of Ray 68. (c) Raw Doppler spectrum of range bin 300.

visible in some azimuths, and labeled in the figure. Note that the azimuths displaying artifacts are not fixed among different PPIs. To take a closer look at the raw range-Doppler spectrogram (i.e., one ray in radar PPI), Ray 68 is extracted as shown in Fig. 2.2(b). Some artifacts are visible along the whole range bins, and they have different nonzero Doppler velocities. Further, range bin 300 (e.g., 9 km) is considered and its Doppler spectrum is plotted as shown in Fig. 2.2(c). We can see that the power intensity of the precipitation is weaker or has the same order of magnitude as the one of artifacts and ground clutter. After integrating the whole Doppler bins, resulting in one reflectivity value, the true reflectivity of precipitation will be biased by the artifacts and ground clutter. Several methods for dealing with the ground clutter have been proposed. The artifacts, however, are harder to mitigate. The exact phenomena responsible for producing the artifacts in the radar data remain unknown at this point. As mentioned in the introduction, such artifacts are not unique to the IDRA radar system. Morse *et al.* (2002) observe similar artifacts in the range-Doppler spectrogram, and attribute them to RFI. However, Cho (2017) states that "in the Doppler spectral domain, Wi-Fi interference in weather radars presents as white noise". This makes us believe that the artifacts observed in this study may not necessarily come from RFI. Since we do not know what they are, we prefer to refer to artifacts as narrow-band moving clutter, due to the fact that they are narrow-band in the Doppler domain with random Doppler velocity values however fixed during a small amount of time. Finally, when we take Ray 68 and generate the range-Doppler spectrogram sequence according to Fig. 2.1, it can be observed that artifacts have the same Doppler velocity over the sequence, while precipitation Doppler velocities vary slightly. The motion variation in the spectrogram sequence will be used as a key feature for the proposed separation method.

Note that artifacts present in IDRA data are narrow-band and their intensity is mod-

Table 2.1: IDRA Specifications (Figueras i Ventura, 2009). The boldface indicates parameters used for the operational mode.

Radar type	Linear FM-CW
Polarization	Fully polarimetric
Center frequency (GHz)	**9.475**
Transmitted power (W)	1, 2, 5, 10, **20**
Range resolution (m)	3, 6, 15, **30**
Scanning rate (rpm)	**1**
Sweep time (μs)	204.8, **409.6**, 8192.2, 1638.4, 3276.8
Frequency excursion (MHz)	**5**, 10, 20, 50
Antenna beamwidth (∘)	**1.8**
Elevation angle (∘)	**0.5**

erate. So when there is heavy precipitation with wide spectral width and large reflectivity, the impact of artifacts is negligible. Hence, artifacts (i.e., narrow-band moving clutter) and precipitation separation in IDRA mentioned in this paper is mainly aimed at moderate, light precipitation and drizzle.

2.3.2. LRMO APPLIED TO ARTIFACT REMOVAL

The LRMO technique is very general and has been successfully used in many applications. In this paper, it is specifically designed for narrow-band moving clutter mitigation in weather radar. Observed in the range-Doppler spectrogram sequence, the multiple spectra of the same range bin (Range bin 290 is taken as an example) from different spectrograms are shown in Fig. 2.3.

Precipitation which has small variation in its Doppler velocity interval because the radar scans and the precipitation advects over time can be modeled in the foreground, while artifacts which have the same Doppler velocity over the sequence can be modeled in the background. As for ground clutter, it will also remain in the foreground, and the reasons are related to two aspects. One is that spectrograms in the sequence are generated from different time sample (i.e., corresponding to different azimuth angles for a rotating radar), which may contain stationary targets (e.g., buildings and trees) of different spectral widths. The other is related to the spectral leakage of FMCW radar (Melzer *et al.*, 2015), especially those range bins near the radar. The ground clutter with different spectral widths forms a high-rank matrix in the spectrogram sequence, leading to its appearance in the foreground. Finally, noise will retain in the background because of the signal model provided in the first part of Eq. (2.12). Specifically, when $S_{qn} = 0$, $\frac{1}{2}\sum_{qn:S_{qn}=0}\left(X_{qn} - B_{qn}\right)^2$ should be minimized, thus noise will be built into background. In addition, the values of parameter β and γ are adaptively obtained and they are positively related to the estimated noise level. When the estimated noise level is larger, namely smaller SNR, to minimize Eq. (2.13), more data will be built into the background, which may lead to some precipitation loss. More discussion of the impact of SNR will be given in Section 2.5.3.

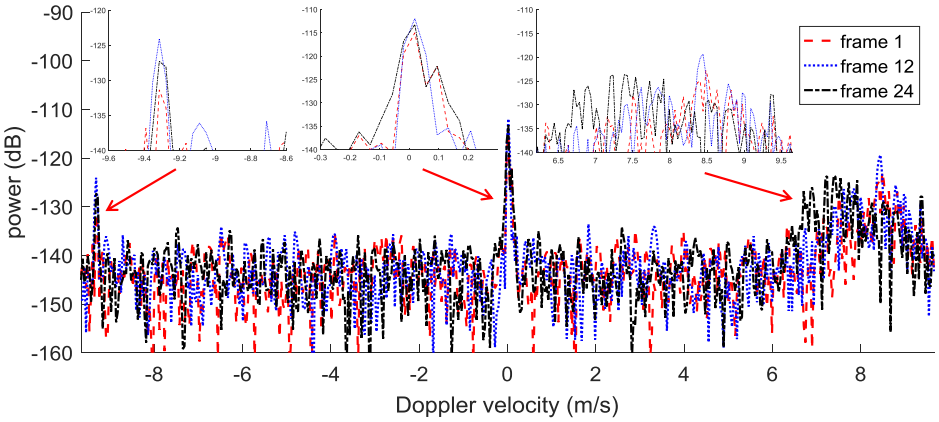

Figure 2.3: The multiple spectra of the same range bin from different spectrograms.

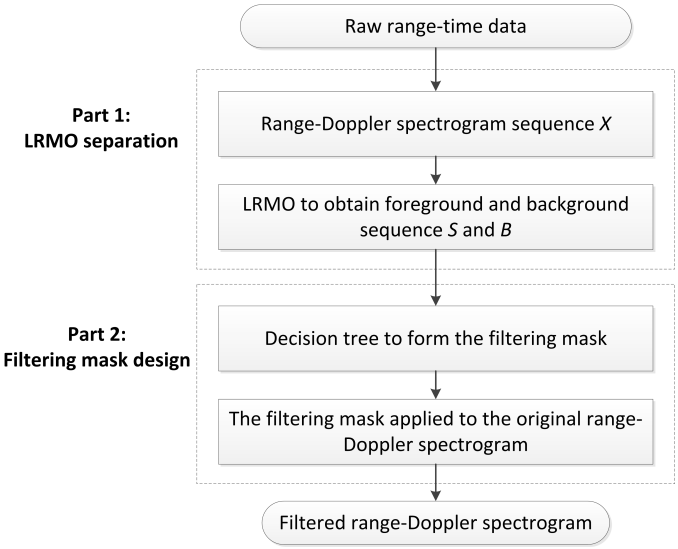

Figure 2.4: The flowchart of the low-rank matrix optimization applied to weather radar to mitigate the narrow-band moving clutter.

The flowchart which consists of the LRMO separation (i.e., the general part) and the filtering mask design (i.e., the specific part) is shown in Fig. 2.4. First, the input of this technique is the raw range-time data. Then, in Part 1, the range-Doppler spectrogram sequence X is generated according to Fig. 2.1. Note that the spectrogram sequence expressed in dB scale should be normalized in the interval of [0, 255]. Such normalization will improve the performance of the algorithm. Next, the foreground sequence S and background sequence B can be separated using the LRMO.

In Part 2, a filtering mask based on a decision tree is applied to remove the narrow-band moving clutter and noise in weather radar. The details of the decision tree will be discussed next. The filtering mask can be applied to the raw spectrogram obtained from the raw range-time data by the Fourier transform to select the precipitation and mitigate the narrow-band moving clutter. The detailed parameter determination will be discussed in Section 2.3.4.

2.3.3. FILTERING MASK DESIGN

After the application of the LRMO, most of the precipitation should be in the foreground. However, sometimes, there may be observations wrongly attributed into the foreground (thereafter refer to as excess background). Therefore, we design a decision tree to detect those observations. Once the excess background has been identified, a filtering mask is applied to the raw spectrogram (i.e., $X_{N/2}$) to select the precipitation part. Note that ground clutter will also be kept in the filtering mask, but can be mitigated later with another technique.

The filtering mask design is given by a decision tree shown in Fig. 2.5. The input of the decision tree is the foreground frequency and the spectral width, both of which are derived from the foreground sequence S after the LRMO. The foreground frequency, defined as the sum of the foreground sequence, is positively related to the probability of precipitating areas. The spectral width helps to recognize the precipitation which is the distributed target in the view of weather radar, thus its spectral width should be distributed along a moderate number of Doppler bins. The excess background will be categorized by large spectral width and small to moderate foreground frequency, or small spectral width and small foreground frequency. Finally, a filtered foreground is obtained, which acts as a filtering mask on the raw spectrogram. Next, the details of the decision tree will be discussed. We start with the input, namely the foreground frequency and the spectral width. The foreground frequency F is defined as the sum of the foreground sequence S:

$$F(r,d) = \sum_{i=1}^{N} S_i(r,d) \tag{2.14}$$

where $r \in [1,R]$ and $d \in [1,D]$ represent the range bin and Doppler bin, respectively. The larger the values of the foreground frequency, the more likely the area contains precipitation. Based on the foreground frequency F, the mask index M which indicates precipitation or ground clutter can be obtained

$$M(r,d) = \begin{cases} 0, & F(r,d) = 0 \\ 1, & F(r,d) \neq 0 \end{cases} \tag{2.15}$$

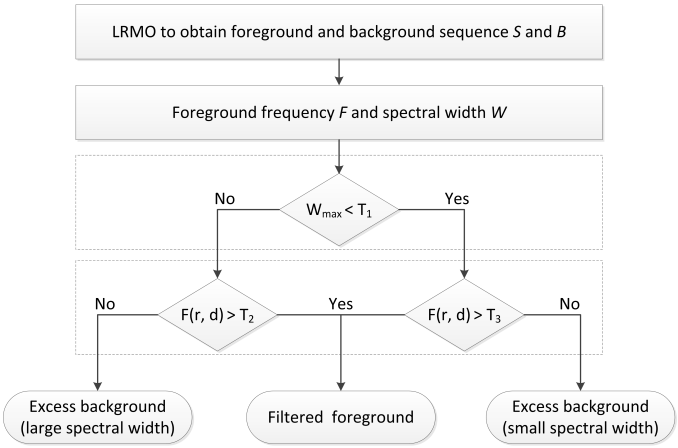

Figure 2.5: The decision tree to form a filtering mask for the raw range-Doppler spectrogram.

Further, by adding up the mask index M along its Doppler axis, the spectral width W in each range bin is obtained

$$W(r) = \sum_{d=1}^{D} M(r,d) \tag{2.16}$$

A proper threshold T_1 should be set to make a comparison with the calculated maximum W which is expressed as W_{max} to further check the existence of excess background. If $W_{max} > T_1$, it means excess background may be present. However, with the different environment (e.g., wind) and radar configuration (e.g., antenna scanning strategy), it will result in different Doppler broadening which finally influences the observed spectral width of precipitation W^{prec}. Hence, it is more reliable to study the real radar measurements to estimate the threshold T_1 which is defined as

$$T_1 = \max\left(W^{prec}\right) \tag{2.17}$$

where max(·) means the maximum value. Such estimations are done by using radar data in Section 2.3.4.

The spectral width W can help to detect the existence of excess background. Then, the way to mitigate the excess background should also be explored. One way to do this is to use the foreground frequency F. Typically, the mask index M in Eq. (2.15) indicates the precipitation areas, which should be used as the filtering mask. On the one hand, if there is excess background with large spectral width in the foreground, all the precipitation should be selected in the foreground sequence. Then, if the corresponding F is larger than one large-value threshold T_2, the mask index M can be kept as the filtering mask. Otherwise, the mask index M should be excluded. On the other hand, if there are no excess background with large spectral width in the foreground, all the mask index related to $M = 1$ should be kept as the final filtering mask. Thus, we set the corresponding F larger than one small-value threshold T_3 to further remove the excess background with small spectral width.

Table 2.2: Precipitation cases used to analyze the spectral width.

Case No	Date & Time	Rain Type
1	2011-07-01 02:00	moderate
2	2011-07-01 12:00	moderate
3	2014-08-22 13:00	moderate
4	2016-01-15 12:00	light

In summary, the detection and mitigation of excess background in the foreground, as well as the filtering mask generation, can be visualized as a decision tree shown in Fig. 2.5. If $W_{max} > T_1$, it means that the background separation is not sufficient. In this case, all the precipitation will remain in the foreground sequence S, which means that the foreground frequency indicating precipitation is large. Next if $F(r,d) > T_2$, the corresponding $M(r,d)$ indicates precipitation. Otherwise, it is excess background with large spectral width. On the other hand, if $W_{max} < T_1$, we should keep all non-zero areas in F but add one extra condition $F(r,d) > T_3$, where T_3 is a small value, to further remove the excess background with small spectral width.

2.3.4. PARAMETER SELECTION

The basis of the proposed narrow-band moving clutter removal method is the spectrogram sequence originating from one range-time dataset. In this section, the choices of the sequence number N and sequence interval L are discussed. With $K = \lfloor \sqrt{N} \rfloor$ in the LRMO (Zhou *et al.*, 2013), the selection of the sequence number N relates with the low-rank property of the background. Normally, K can be predefined after several target and clutter separation scenario studies, and then the value interval of N can be given. Because calculation time increases with N, the smallest possible value should be selected. However, if N is too small, the precipitation change in the spectrogram sequence may be very small, making it difficult to put the precipitation in the foreground in the LRMO. On the contrary, when N is too large, the background may not be easy to detect as it changes too much, leading to excess background appearing in the foreground. As for the sequence interval L, it determines the correlation between the neighboring spectrograms. If L is set too large, the correlation of artifacts between the neighboring spectrograms is too small, making it impossible to model the artifacts as the low-rank matrix in the background. On the other hand, if the sequence interval is too small, the precipitation in the foreground between the neighboring spectrograms is almost the same, meaning it will end up in the background. Hence, the values of N and L should be well balanced. Moreover, they should meet the principle that the detection probability of precipitation P_d in the filtering mask should be close to 1 and that of artifacts and excess background P_{fa} (i.e., false alarm rate) in the filtering mask as low as possible. P_d is defined as the area of the precipitation in the filtering mask divided by that of the true precipitation, and P_{fa} the area of the background in the filtering mask divided by that of the true background. Note that the true area of precipitation and background are obtained by manual selection. P_{fa} quantifies the excess background in the foreground, and its removal can be done following the decision tree as discussed in Section 2.3.3.

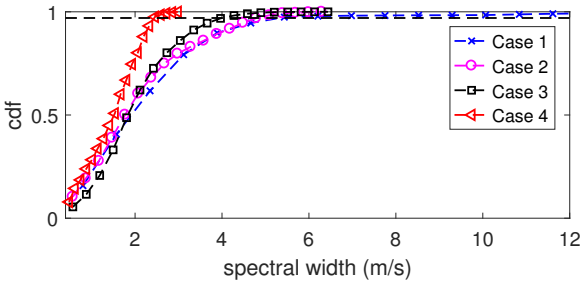

Figure 2.6: Cumulative distribution function of precipitation spectral width.

The sequence number N and the sequence interval L are chosen based on IDRA data. A sensitivity analysis of N and L will be given in Section 2.5.1. To calculate the detection probability in the filtering mask, the thresholds T_1, T_2 and T_3 in Fig. 2.5 should firstly be estimated. According to Eq. (2.17), T_1 should be selected based on the radar data. Aiming at suppressing artifacts in the moderate, light precipitation and drizzle, 4 cases of IDRA data collected during 2011 - 2016 are selected as shown in Table 2.2. The relation between the spectral width and cumulative distribution functions are shown in Fig. 2.6. The black dash line is 0.97 and it indicates that almost all the spectral widths are within $5.5\,\mathrm{m\,s^{-1}}$ which corresponds to 146 Doppler bins for operational IDRA configuration (Doppler velocity resolution is $3.8\,\mathrm{cm\,s^{-1}}$). Considering the co-existence of the ground clutter, the threshold can be set to $T_1 = 160$. The thresholds T_2 and T_3 are chosen to remove the background appearing in the foreground. As it is also discussed in Section.2.3.3, T_2 should be large while T_3 small. The spectrogram sequence N is obtained by moving the raw data forward and backward equally in the slow-time. Hence, in the case of excess background with large spectral width in the foreground sequence, $T_2 = N/2$ can be set to eliminate the excess background adjacent to the precipitation in $X_{N/2}$. As for the excess background with small spectral width, it appears randomly in the spectrogram sequence. So, the removal can be done by setting $T_3 = 2$ for the IDRA measurements. Note that the noise is eliminated with the thresholding of T_2 and T_3.

After the choice of the thresholds in the decision tree, the sequence number N and the sequence interval L can be selected through the detection probability and the false alarm rate in the filtering mask. After the statistical analysis of 10 cases (each case contains more than 140 rays) during the time from 2011 to 2016, the sequence number was empirically set to $N = 24$, which correspondingly predefines $K = 4$. More discussion of the N selection will be given later. The selection of the sequence interval L should fulfill the following condition: the detection probability of precipitation P_d is close to 1 and the false alarm rate P_{fa} is as low as possible. Setting L in the interval of $[16, 26]$, we used Ray 68 of IDRA data measured at 02:00 UTC on 1st July 2011, to calculate the P_d and P_{fa} which are shown in Fig. 2.7. Normally, with the increase of the sequence interval L, which will decrease the correlation between neighboring spectrograms, P_d and P_{fa} should also increase. This is observed when $L \in [16, 24]$. However, this is not true for $L = 26$. The reason is that the larger sequence interval L will reduce the foreground frequency F, meaning that the decrease of P_d and P_{fa} is due to the decision tree mitigation.

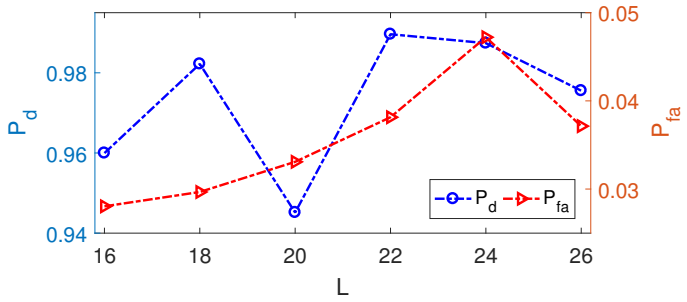

Figure 2.7: Detection probability of precipitation and background with different sequence intervals.

Based on the result in Fig. 2.7, the deviation of P_d and P_{fa} obtained from different L selection is not too large, which means that it should be possible to use the same value of L for other data. Finally, we choose the sequence interval $L = 22$ which gives a good detection probability of precipitation P_d even though P_{fa} is not optimal. Indeed, P_{fa} can be further mitigated by the decision tree, which leads to acceptable values.

2.4. PERFORMANCE VERIFICATION

The IDRA data are used to verify the performance of the proposed precipitation and narrow-band moving clutter separation method. Firstly, we check the extracted foreground and background for a given range-time dataset. Ray 68 at 02:00 UTC on 1st July 2011 is used to define the raw range-Doppler spectrogram $X_{N/2}$ in Fig. 2.2(b). Then the raw spectrogram expressed in dB scale is normalized in the interval of [0 255] as shown in Fig. 2.8(a). The corresponding low-rank background $B_{N/2}$ and the foreground $S_{N/2}$, as shown in Fig. 2.8(b) and Fig. 2.8(c), are extracted by performing the LRMO in Eq. (2.13). We can observe that all the artifacts remain in the background areas while the precipitation as well as the ground clutter are in the foreground areas, which is consistent with the analysis in Section 2.3.2. However, there is some signal loss at the boundaries of the precipitating areas which corresponds to regions with lower SNR. These areas can be recovered by using the foreground frequency F displayed in Fig. 2.8(d). With the considered data, the decision tree generates the filtering mask with the condition $W_{max} < T_1$ and $F(r,d) > T_3$, as shown in Fig. 2.8(e). Finally, the filtering mask can be applied to the raw spectrogram to mitigate the artifacts and noise. Note that the low-rank matrix optimization is carried out using Matlab 2016b in a Window 7 desktop PC with a 3.6 GHz Intel Xeon E5-1620 CPU and 16 GB RAM, and the time elapsed for this separation is 69 s, which currently may be difficult to implement in real time for operational weather radar, but could be significantly reduced using dedicated software.

Additionally, the proposed method is compared with the polarimetric optimization (POLO) method described by Yin *et al.* (2016). As shown in Fig. 2.9(a) and Fig. 2.9(b), there are some artifacts remaining in the POLO method while the LRMO can mitigate all of them. Apart from this, the LRMO has better performance in noise removal. There is excess background in the filtered spectrogram based on the POLO. Moreover, there is some signal loss at the boundaries of the precipitating areas while the LRMO can avoid

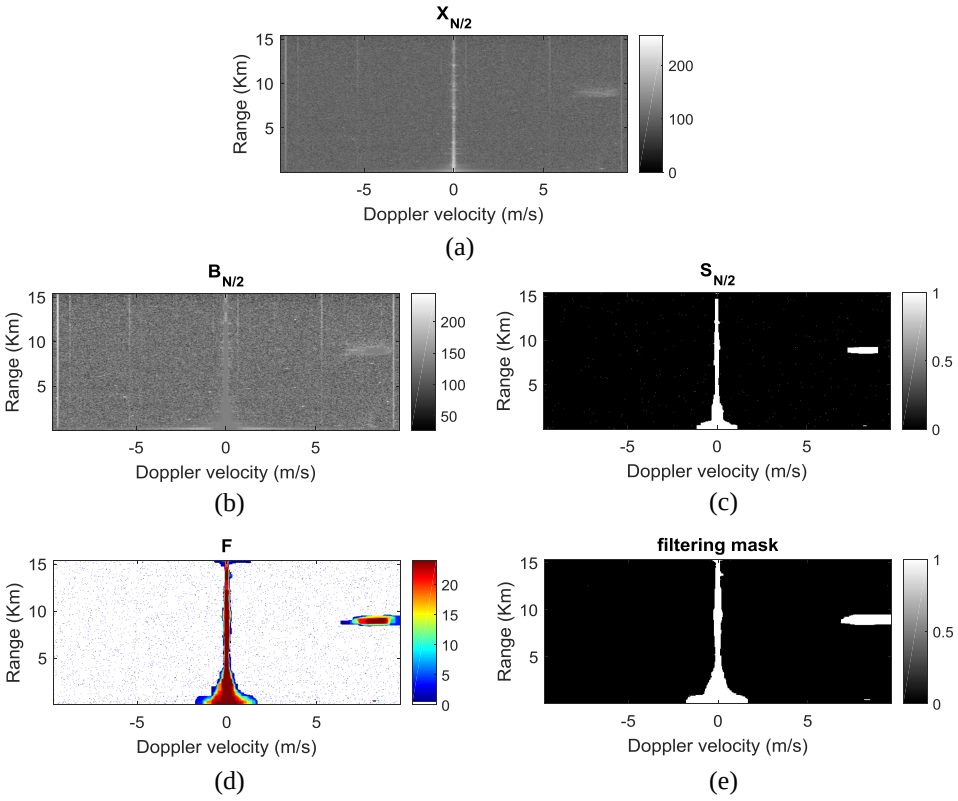

Figure 2.8: Background and foreground extraction based on the low-rank matrix optimization. (a) Raw spectrogram $X_{N/2}$ scaled in [0 255]. (b) Low-rank background $B_{N/2}$. (c) Foreground $S_{N/2}$. (d) Foreground frequency F. (e) Filtering mask.

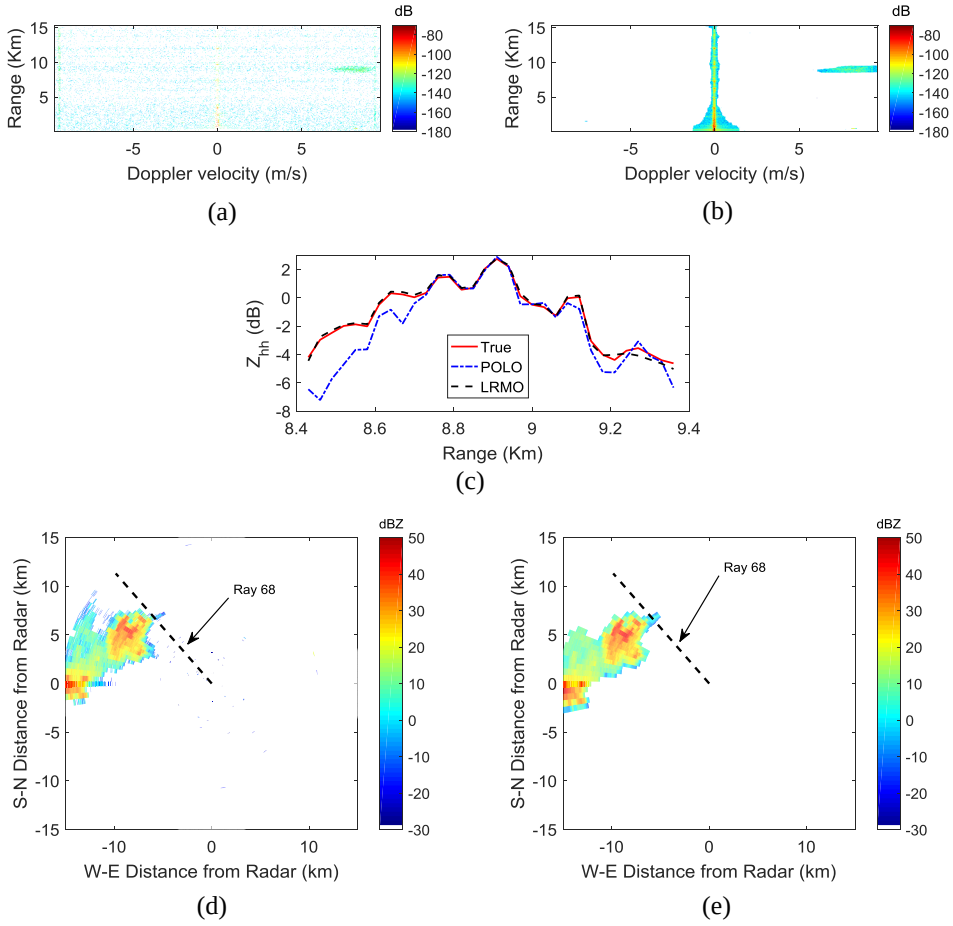

Figure 2.9: Performance comparison between the polarimetric optimization and low-rank matrix optimization. Data measured at 02:00 UTC on 1st July 2011. (a) Spectrogram after the polarimetric optimization. (b) Spectrogram after the low-rank matrix optimization. (c) Reflectivity quantitative comparison. (d) Reflectivity PPI after the polarimetric optimization. (e) Reflectivity PPI after the low-rank matrix optimization.

this problem by using more data during the processing, that is, N spectrograms instead of one for the POLO. Additionally, LRMO does not require the polarimetric measurements, making it broadly applicable.

The quantitative performance of the two methods is compared using the true reflectivity in the 8.4 - 9.4 km range. The results are shown in Fig. 2.9(c). Legend "True" refers to the true values of reflectivity, which are manually selected. The maximum deviation between the POLO based Z_{hh} and the true Z_{hh} is 4.2 dB, while that between the LRMO Z_{hh} and the true Z_{hh} is 0.5 dB. Both reflectivity deviations are calculated based on the assumption that the ground clutter can be completely mitigated by another technique. Note that the true Z_{hh} is around -2 dBZ, corresponding to weak precipitation. This shows

that the proposed LRMO technique is particularly promising for weak signal preservation.

Apart from the spectrogram comparison, the PPI assessment is also necessary. The results are shown in Fig. 2.9(d) and (e). Note that the PPIs are obtained by using the notch filter centered around $0\,\mathrm{m\,s^{-1}}$ to completely remove the ground clutter. The LRMO filtered PPI tends to have larger reflectivity values than the POLO ones. This is because of the better performance in weak precipitation preservation for the LRMO approach. In addition, the PPI contains 146 rays, and the PPI output also conforms the robustness of the chosen parameters for precipitation and narrow-band moving clutter separation.

Finally, the performance of the proposed separation technique can also be verified by other data measured of different times as shown in Fig. 2.10. Note that the parameter selection for the LRMO separation approach applied to these measurements is the same as in the study case, Ray 68 (measured at 02:00 UTC on 1st July 2011). Here Ray 41 and Ray 61 from 18:00 UTC on 5th July 2012 and Ray 51 and Ray 70 from 13:00 UTC on 22nd August 2014 are considered. From Fig. 2.10, we can see that the proposed artifact removal method is effective for both weak small-scale and moderate large-scale precipitation with different velocities ranging from $0\,\mathrm{m\,s^{-1}}$ to the maximum unambiguous Doppler velocity. Note that the very weak precipitation areas in Fig. 2.10(a) are also successfully extracted by the proposed technique.

2.5. PARAMETER SENSITIVITY ANALYSIS

2.5.1. SPECTROGRAM SEQUENCE PARAMETER SELECTION

To explore the influence of N and L, a simulation was conducted by setting N in the interval of $[4,40]$ in a step of 2 and L in the interval of $[16,26]$ with the same step. This was done for Ray 68 of IDRA data measured at 02:00 UTC on 1st July 2011. Then, the detection probability P_d and the false alarm rate P_{fa} were calculated with different combinations of N and L. The results are shown in Fig. 2.11.

As stated in Section 2.3.4, the selection of N and L should meet the requirement that P_d is close to 1 while P_{fa} is as low as possible. From Fig. 2.11, it can be observed that P_d and P_{fa} tend to increase with larger values of N and L. However, when N and L are too large (i.e., $N > 24$ and $L > 22$), the increase of P_{fa} will be dominant while P_d is already close to 1, which means most of the precipitation is in the foreground and more excess background is appearing. On the other hand, when N and L are smaller than 20, P_d is relatively small, except when $N = 14$ for which we get some promising P_d. However, this may be a local optimum specific to the used data. Therefore, we decided to use $N = 24$ and $L = 22$.

Next, we made a comparison between different values of N for a fixed value of $L = 22$. From Fig. 2.11, we conclude that fixing $L = 22$, with $N = 14$, $N = 24$ and $N = 34$, leads to similar P_d and P_{fa} values. Taking another case, namely Ray 41 of the measurement at 18:00 UTC on 5th July 2012 shown in Fig. 2.10(a), we applied the LRMO with parameter setting $N = 14$, $N = 24$ and $N = 34$. Note that the ray used in this experiment is related to very weak precipitation. The corresponding filtered spectrograms are shown in Fig. 2.12(c), Fig. 2.10(a) and Fig. 2.12(d), respectively. Additionally, the results of F with different parameter sets are shown in Fig. 2.12. The computation time depends non-

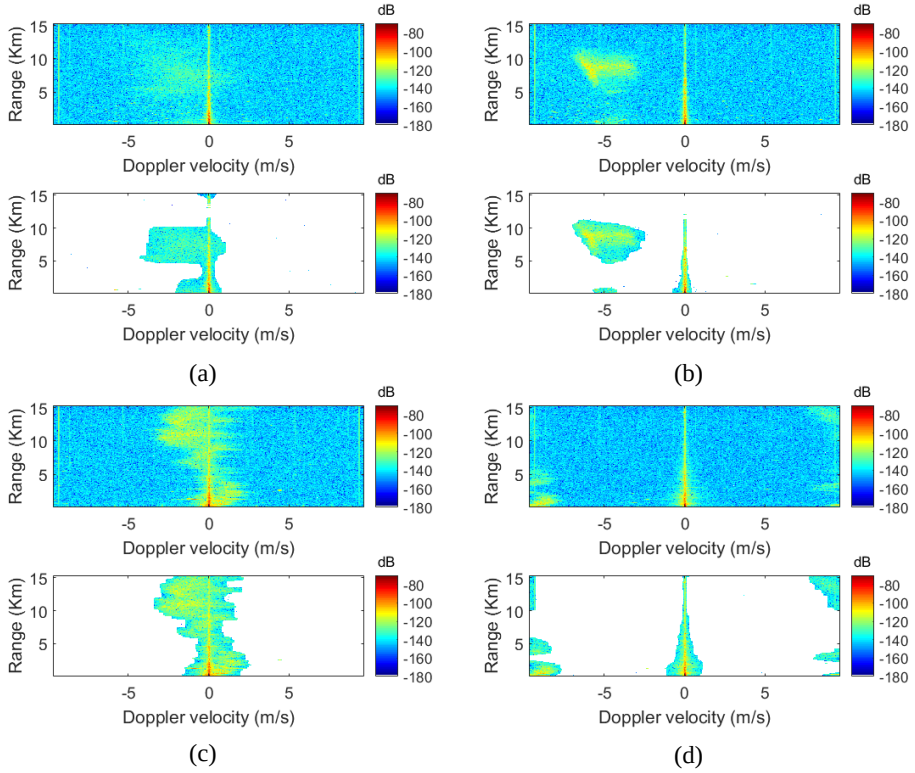

Figure 2.10: Performance verification with two other cases. (a) Ray 41 and (b) Ray 61 are from 18:00 UTC on 5th July 2012. (c) Ray 51 and (d) Ray 70 are from 13:00 UTC on 22nd August 2014.

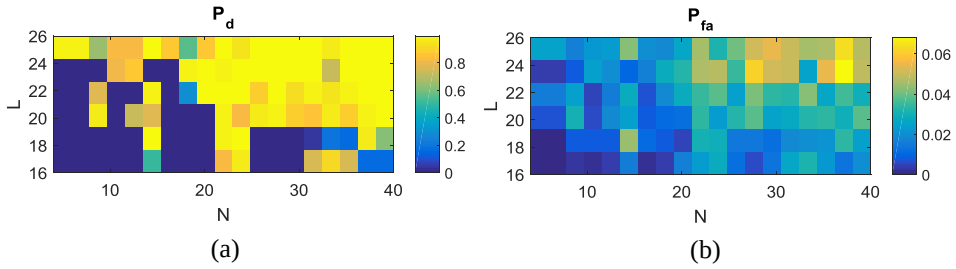

Figure 2.11: Parameter selection for the spectrogram sequence: (a) Detection probability P_d. (b) False alarm rate P_{fa}.

linearly on N, so the smaller the N, the faster the LRMO will be performed. In this case, the elapsed time for different N is 41 s, 115 s and 133 s. However, as is stated in Section 2.3.4, N should not be too small, otherwise it is difficult to put the precipitation in the foreground, as illustrated by Fig. 2.12(a) and (c). On the other hand, when N is large, more background will appear in the foreground because the background is no longer

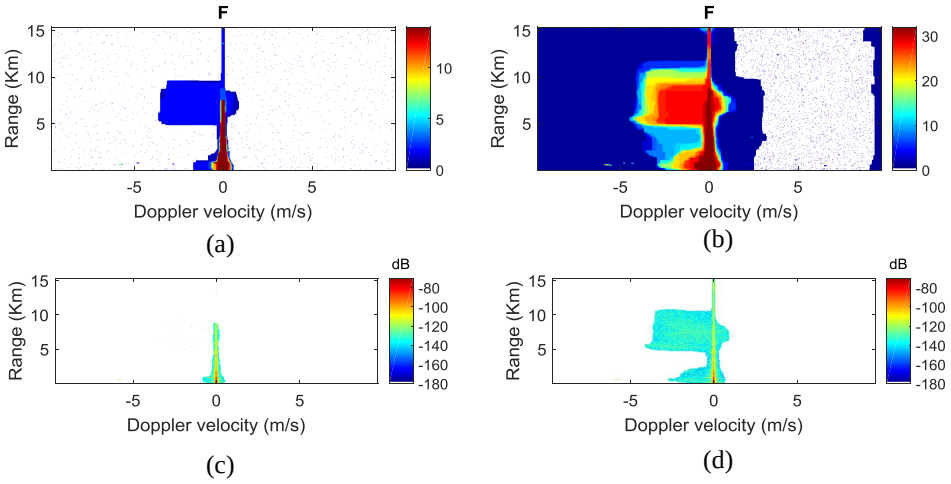

Figure 2.12: Parameter selection for the spectrogram sequence. (a) F with $N = 14$ and $L = 22$. (b) F with $N = 34$ and $L = 22$. (c) Filtered spectrogram with $N = 14$ and $L = 22$. (d) Filtered spectrogram with $N = 34$ and $L = 22$.

fixed for a long spectrogram sequence, as shown in Fig. 2.12(b) and (d).

In summary, both the sequence number N and the sequence interval L should be well balanced. When applying this technique to other radar signal and clutter scenarios, the detection probability and the false alarm rate can be used to select the best combination.

2.5.2. LRMO PARAMETER SELECTION

As stated in Section 2.2.2, the parameter tuning for the low-rank matrix optimization consists of the selection of K and γ since α and β can be dynamically adjusted during the calculation procedure. Coming back to Ray 68 measured at 02:00 UTC on 1st July 2011, the sensitivity of the results with respect to the choice of K and γ selection is discussed. By default, K and γ are set to 4 (i.e., $\lfloor\sqrt{N}\rfloor$) and 5β, respectively. Firstly, we fix $\gamma = 5\beta$, and change K which takes the values 3 and 5; then K is fixed to 4, and γ takes the values 4β and 6β. The results of the corresponding $S_{N/2}$ and F are displayed in Fig. 2.13.

We first explore the influence of K on the LRMO performance by fixing $\gamma = 5\beta$. Making a comparison with the results of the default setting as shown in Fig. 2.8(c) and Fig. 2.8(d), we observe that when K is too small, there is less precipitation in the background (the one with lower SNR). However, this comes at the cost of more excess background (in that case noise) in the foreground. Hence, more details can be preserved as observed in the F of Fig. 2.13(a). Note that in this case, it is still possible to achieve good clutter filtering performance with larger F thresholding, which shows the flexibility in parameter selection for the proposed technique. On the other hand, when K is larger, more precipitation will end up in the background, disappearing from $S_{N/2}$ and F as shown in Fig. 2.13(b). From the above analysis, we can conclude that the LRMO performance is sensitive to the selection of K. When $K = 4$, and γ changes from 4β to 6β, there is only a

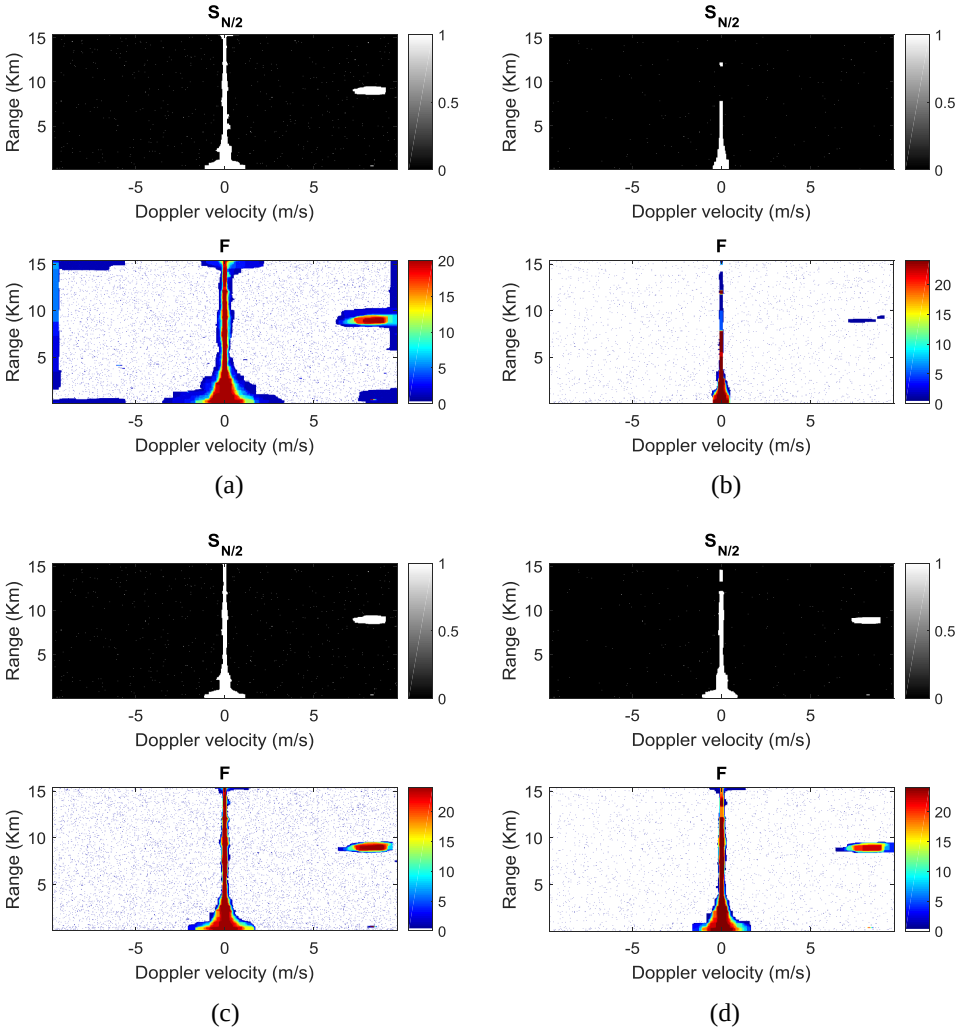

Figure 2.13: Parameter selection for the low-rank matrix optimization. (a) $K = 3, \gamma = 5\beta$. (b) $K = 5, \gamma = 5\beta$. (c) $K = 4, \gamma = 4\beta$. (d) $K = 4, \gamma = 6\beta$.

slight decrease of the extent of the precipitating areas and excess background in $S_{N/2}$ and F as shown in Fig. 2.13(c) and Fig. 2.13(d). This is because γ controls the smoothness of the foreground, which means that the increase of γ will inevitably reduce the excess background and the size of the precipitating areas in the optimization. From the above analysis, it is concluded that the LRMO performance is not too sensitive to the selection of γ.

In summary, the LRMO performance is sensitive to the background low-rank K but not too much to the foreground smoothness γ. This means the parameter K should be

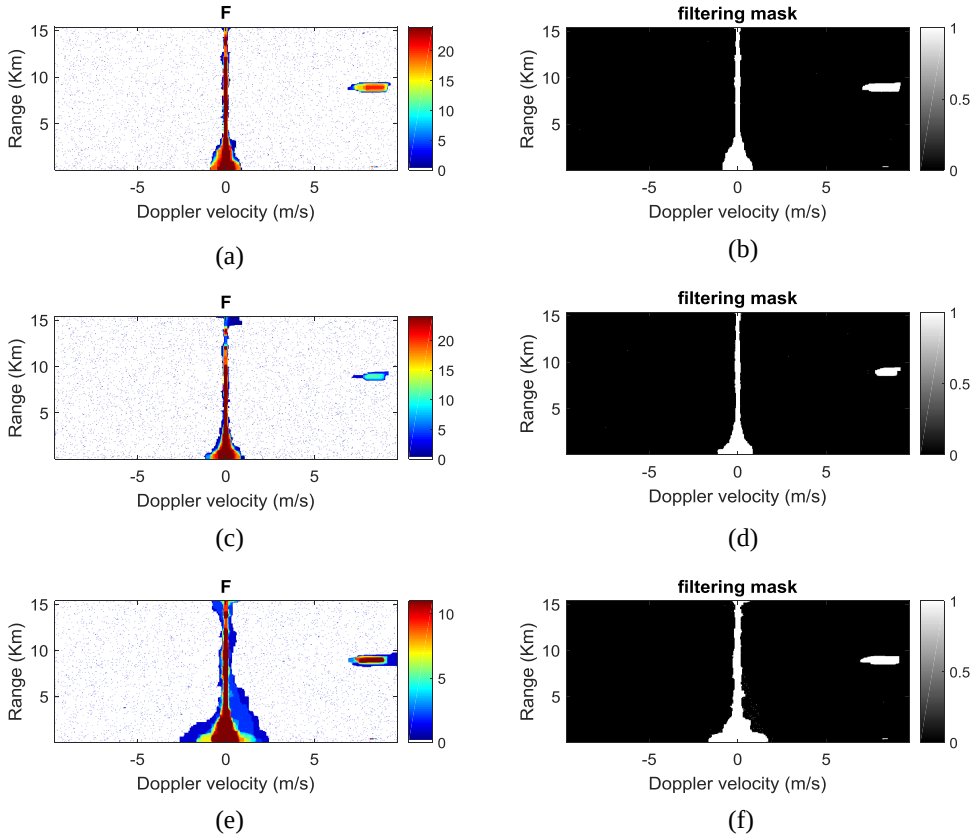

Figure 2.14: Different SNR for the low-rank matrix optimization. (a) F with $K = 4$ and noise floor 10 dBW. (b) filtering mask with $K = 4$ and noise floor 10 dBW. (c) F with $K = 4$ and noise floor 20 dBW. (d) filtering mask with $K = 4$ and noise floor 20 dBW. (e) F with $K = 3$ and noise floor 20 dBW. (f) filtering mask with $K = 3$ and noise floor 20 dBW.

well predefined. Normally, we can start with the default setting, and then K is tuned around $\lfloor\sqrt{N}\rfloor$ until a satisfactory result is obtained. Finally, γ can be tuned to further improve the results.

2.5.3. IMPACT OF SNR

To explore the impact of SNR on the proposed technique, we simulated signals by adding different noise levels to the original IQ data. The data used are also Ray 68 of IDRA measurements collected at 02:00 UTC on 1st July 2011. The simulated noise levels are 10 dBW and 20 dBW, and the corresponding F and filtering mask are displayed in Fig. 2.14(a) - Fig. 2.14(d). Comparing with the situation without additional noise as shown in Fig. 2.8(d) and (e), as the intensity of the noise increases, we see that more and more weak precipitation is removed from the foreground. The reason has been explained in Section 2.3.2, namely that with the decrease of SNR, more data will be built into background due

to the optimization equation, leading to some precipitation loss. This undesired outcome can be avoided by proper parameter tuning in the LRMO, for example by setting the value of K to 3 instead of $K = 4$ as shown in Fig. 2.14(e) and (f). For the same noise level (i.e., 20 dBW), when K changes from 4 (i.e., Fig. 2.14(d)) to 3 (i.e., Fig. 2.14(f)), the lower K retains more precipitation in the foreground, demonstrating that a large part of the precipitation can still be recovered with this technique, even for lower signal to noise ratios.

2.6. CONCLUSION

A novel radar target and moving clutter separation technique based on a combination of the low-rank matrix optimization and a decision tree has been proposed. The technique is primarily based on different motion variation of target and clutter in the range-Doppler spectrogram sequence. The technique is very general but the focus of this paper is on narrow-band moving clutter suppression in weather radar. Although the low-rank matrix optimization has been widely used in many applications, this is the first application for weather radar clutter mitigation.The first step of this algorithm is the range-Doppler spectrogram sequence generation which consists of the selection of the sequence interval and the sequence number. The low-rank matrix optimization is then applied to the sequence to separate precipitation and moving clutter into foreground and background. An additional decision tree based on the foreground frequency and spectral width is designed to generate a filtering mask to keep precipitation and remove clutter and noise. Several precipitation cases measured by the radar IDRA are used to assess the proposed radar target and clutter separation method.

The proposed technique has several advantages. It is a good mitigation technique for narrow-band moving clutter and noise, and it can also preserve weak signals. Additionally, it fully takes advantage of motion properties of radar target and clutter. However, there are also some limitations. Firstly, the performance is sensitive to the predefined low-rank value K, which requires proper parameter tuning. Secondly, it is not a complete mitigation method. In the case of IDRA, the ground clutter remains in the final filtered spectrogram, which means another filtering method (e.g., GMAP) is necessary to fully remove all the unwanted echoes. To prevent signal loss, ground clutter detection algorithms (e.g., CMD (Hubbert *et al.*, 2009a)) should be implemented before ground clutter filtering. Since the presence of moving clutter may bias the ground clutter detection accuracy, we recommend to first mitigate the moving clutter, then the ground clutter. Finally, the proposed algorithm is computationally expensive, and for now cannot be implemented in real-time for operational radar systems. However, this could be feasible using optimized dedicated software.

It is foreseeable that the LRMO method could be extended to the wind turbine clutter mitigation in weather radar, or to other radar systems such as air traffic control radar and marine radar if target and clutter have different motion variation. In other scenarios, the decision trees can be adapted to mitigate other forms of clutter. For example, in the case of wind turbine clutter mitigation in weather radar, wind turbine clutter may be attributed to the category of excess background with large spectral width. Because wind turbine clutter has a large spectral width, but small foreground frequency due to the fast-changing Doppler velocity. Furthermore, the separation technique may also be

extended to include different clutter echoes in various background layers (Stauffer and Grimson, 1999), with the interested target in the foreground. More research can be done in these directions in the future.

3

NARROW-BAND CLUTTER MITIGATION IN SPECTRAL DOMAIN FOR POLARIMETRIC WEATHER RADAR

This chapter has been published as:

Jiapeng Yin, Christine Unal, and Herman Russchenberg. "Narrow-band clutter mitigation in spectral polarimetric weather radar", *IEEE Trans. Geosci. Remote Sens.*, 55(8):4655 - 4667, 2017.

The technique described in Chapter 2 can remove moving narrow-band clutter and keep weak precipitation, but it is computationally expensive, which makes it difficult to implement in real-time. Observed in the Doppler domain, the narrow-band clutter includes: 1) stationary clutter such as ground clutter and 2) nonstationary clutter such as artifacts caused by the radar system itself or external sources. These artifacts are difficult to remove, because they are not confined to specific azimuth and range bins. To develop a real-time technique which can mitigate the narrow-band clutter, this chapter introduces a new clutter suppression method named the moving double spectral linear depolarization ratio (MDsLDR) filter for full-polarimetric weather radar. Taking advantage of the difference of the spectral polarimetric features and spectral continuity of precipitation and clutter, the MDsLDR filter generates a filtering mask implementing on the range-Doppler spectrogram to remove the clutter and noise, and keep the precipitation.

Except the introduction is given in Section 3.1, the reminder of this chapter is organized as follows. In Section 3.2, the IDRA system, its standard clutter suppression processing, and its artifacts are introduced. The details of the newly proposed method are provided in Section 3.3. In Section 3.4, the parameter setting, the detailed implementation, and performance analysis are discussed. Furthermore, the MDsLDR filter is applied using different Doppler velocity resolutions. Then, two more cases are used to further verify the effectiveness of this newly proposed method in Section 3.5. Finally, some conclusions are drawn in Section 3.6.

3.1. INTRODUCTION

The presence of clutter may lead to misdetection of weather echoes or introduce bias on weather radar observables, which has aroused extensive attention in radar meteorology (Fukao *et al.*, 2014). The radar environment is so complicated that it contains different sources of clutter, such as ground clutter, insects and birds, radio frequency interference (RFI), and radar artifacts etc.. These clutter significantly affect both the quality of the measurement and the observation of precipitation areas. Hence, it is important to find a way to suppress all the unwanted echoes.

For ground clutter suppression, the conventional method is the narrow notch filter centered around $0\,\mathrm{m\,s^{-1}}$ (Groginsky and Glover, 1980) whose performance depends on the spectral width of ground clutter. However, the spectral width is variable because of the change of environment and observation conditions. Moreover, sometimes the radial velocities of precipitation and ground clutter will overlap, leading to the loss of the target signal. To cope with these problems, the Gaussian model adaptive processing (GMAP) is introduced by Siggia and Passarelli Jr (2004). The adaptive ground clutter suppression filter can recursively interpolate over the removed clutter component to recover the overlapping precipitation signal. Moreover, GMAP can dynamically adjust the window type according to the calculated clutter to signal ratio (CSR). However, when GMAP is applied on non-contaminated gates, the reflectivity will be underestimated. Hence, it is necessary to detect the existence of clutter before the application of this suppression method. Combining with three discriminants — clutter phase alignment, texture of reflectivity, and spin, the clutter mitigation decision (CMD) is proposed to identify the nonmeteorological echo (Hubbert *et al.*, 2009a,b) in real time. Associating the GMAP with CMD, it results in significant improvements in ground clutter suppression on WSR-88D (Ice *et al.*, 2009). Nevertheless, there will be some signal loss due to the false detections along zero isodop by using CMD technique. Additionally, there is also the problem of spatial irregularities in data fields with such combination.

Similar to CMD, a spectrum clutter identification (SCI), combining both the power and phase in the spectral domain, uses a Bayesian classifier to detect ground clutter mixed with weather signals (Li *et al.*, 2013). The performance of SCI is better than CMD mostly in the low CSR. Likewise, the spectrum-time estimation and processing (STEP) algorithm integrates SCI, bi-Gaussian clutter filtering, and multi-lag moment estimation to fulfill clutter identification, clutter filtering and noise reduction, respectively (Cao *et al.*, 2012). The STEP algorithm requires large computational resources, and further optimization should be conducted to implement in real time.

Recently developed Clutter Environment Analysis using Adaptive Processing (CLEAN-

AP) (Warde and Torres, 2014) is based on the phase of the auto-correlation spectral density. Compared with the combination of CMD and GMAP, CLEAN-AP uses both magnitude and phase for improved notch width determination that results in smaller biases, and it has more clutter suppression and less variance of estimates (Torres *et al.*, 2012). However, while CLEAN-AP can deal with normal-propagation (NP) and anomalous-propagation (AP) clutter, it is not a mitigation technique for moving clutter such as airplanes, cars.

The CMD technique mentioned above is one of the fuzzy logic algorithms adopted in the clutter identification. Others include the hydrometeor classification algorithm (HCA) (Liu and Chandrasekar, 2000; Park *et al.*, 2009; Mahale *et al.*, 2014) and non-meteorological echoes recognition proposed by Moisseev and Chandrasekar (2009); Ye *et al.* (2015). The fuzzy logic algorithms are mainly based on the dual-polarization measurements which provide additional echo features for classification. However, its robustness and effectiveness can not be guaranteed because of different radar configurations and variable weather conditions.

In addition to ground clutter, other types of clutter are also reported in many publications. The characteristics of birds and insects are presented by Stepanian and Horton (2015); Zrnic and Ryzhkov (1998); Melnikov *et al.* (2014, 2015). Besides, Alku *et al.* (2015) demonstrates the effectiveness of the image processing techniques together with fuzzy logic to mitigate other clutter, such as sea and chaff clutter.

Apart from the clutter mentioned above, artifacts also affect the application of weather radar data. The artifacts are caused by the radar system itself or external sources displaying in the radar plan position indicator (PPI). Most of the time, artifacts are speckles along the whole range bins in some azimuth directions in the PPI. Consequently, these speckles are not confined to some range bins and further they are non-stationary when observed in the Doppler domain, making it impossible to mitigate them with the conventional clutter suppression methods. These artifacts not only affect the reflectivity, but also the Doppler and polarimetric measurements. For example, artifacts have influenced the display of the polarimetric X-band radar IRCTR Drizzle Radar (IDRA) since its installation in 2007. Also, the high-resolution X-band radar MESEWI, which is currently under development at the Delft University of Technology, suffers from the similar problem (Krasnov and Yarovoy, 2016). Additionally, the C-band meteorological radars of the European operational weather radar network (EUMETNET/OPERA Radar Network, (Huuskonen *et al.*, 2014)) increasingly becoming infected with the Radio Local Area Network (RLAN) need effective and real-time artifact removal techniques (Joe *et al.*, 2005). The artifact signatures such as dots, spokes, or stripes manifesting on the radar images caused by wireless technology are well documented by Saltikoff *et al.* (2016).

To deal with the dilemma of narrow-band clutter including stationary ground clutter and non-stationary artifacts, this paper puts forward a method named the moving double spectral linear depolarization ratio (MDsLDR) filter to keep almost all the precipitation while removing the artifacts, ground clutter as well as noise. Based on the spectral-polarization property and the spectral continuity, the newly proposed clutter suppression method implements its filtering in the range-Doppler spectrogram (i.e. one ray in radar PPI). MDsLDR filter adopts moving window to remove the unwanted clutter, and then the mathematical morphology method (Najman and Talbot, 2013) is applied to recover the removed precipitation. The ray by ray clutter mitigation technique can

be used regardless of different Doppler velocity resolutions. Furthermore, MDsLDR is proven to be computationally efficient and can be applied in real time.

3.2. RESEARCH WEATHER RADAR OBSERVATION

3.2.1. DATA COLLECTION

The horizontally scanning polarimetric X-band IDRA was installed in the Dutch meteorological observatory, Cabauw Experimental Site for Atmospheric Research (CESAR) in 2007 (Figueras i Ventura, 2009; Otto and Russchenberg, 2014). On top of the 213-meter atmospheric measurement mast, IDRA is the second highest location in the surroundings. IDRA is a linear frequency modulated continuous wave (FMCW) radar with the center frequency 9.475 GHz. Moreover, this compact X-band radar is a polarimetric Doppler radar whose spectral polarimetric information can significantly improve the performance of signal processing and data processing. Additionally, IDRA rotates horizontally at the speed of 1 round per minute with the fixed elevation angle 0.5°. The specifications of this polarimetric X-band radar are shown in Table 3.1. Note that sweep, which is the terminology for FMCW radar, is equivalent to pulse for pulse radar.

Table 3.1: IDRA Specifications. The boldface indicates parameters used for the operational mode.

Radar type	Linear FMCW
Polarization	Fully polarimetric
Center frequency (GHz)	9.475
Transmitted power (W)	1, 2, 5, 10, **20**
Range resolution (m)	3, 6, 15, **30**
Sweep time (μs)	204.8, **409.6**, 8192.2, 1638.4, 3276.8
Frequency sweep (MHz)	**5**, 10, 20, 50
Antenna beamwidth (◦)	1.8
Elevation angle (◦)	0.5

This compact X-band radar can provide a higher resolution precipitation map compared to lower frequency radars, such as S-band and C-band radars. All the radar data recorded from April 2009 until now are freely accessible to the public on the website named 4TU.centre for Research Data. These data provide a long-term observation to monitor the trends in precipitation change. The range resolution and the Doppler velocity resolution are 30 m and 3.8 cm s^{-1} respectively in the standard processing.

3.2.2. STANDARD CLUTTER SUPPRESSION PROCESSING

Currently, the standard clutter suppression processing of IDRA is carried out in the range-Doppler domain. It consists of a narrow notch filter centered around 0 m s^{-1} and the double spectral linear depolarization ratio (DsLDR) filter (Unal, 2009). Further, a noise clipping technique is implemented. It keeps the Doppler bins related to a spectral reflectivity at least 3 dB above the Doppler noise level. Finally, isolated Doppler bins and Doppler spectra containing less than 2% of Doppler bins are discarded. The DsLDR filter

is based on the different distribution of the spectral-polarimetric parameter — spectral linear depolarization ratio (sLDR) (Yanovsky, 2011) of precipitation and clutter.

These spectral polarimetric parameters are defined as (Unal, 2009)

$$\begin{aligned} sLDR^{hh}(v,r) &= 10log_{10}\left(\frac{|S_{vh}(v,r)|^2}{|S_{hh}(v,r)|^2}\right) \\ sLDR^{vv}(v,r) &= 10log_{10}\left(\frac{|S_{hv}(v,r)|^2}{|S_{vv}(v,r)|^2}\right) \end{aligned} \tag{3.1}$$

where $S_{xy}(v,r)$ represents the complex range-Doppler spectrogram with a transmitted y polarization and a receiving x polarization, x and y being horizontal or vertical polarization. Further v and r are the Doppler velocity and the range respectively. The assumption on the reciprocity condition $S_{vh} = S_{hv}$ is applied, which is true in theory and should be verified by measurements. Currently, for IDRA, only S_{vh} is measured.

Combining simultaneous Doppler and polarimetric information, it can improve the understanding of the microstructure of precipitation (Yanovsky, 2012). On the one hand, the Doppler information indicates the moving behavior of the precipitation scatterers that are within the resolution volume but are moving with different velocities. The spectral width of precipitation is an important feature to discriminate from other targets. On the other hand, linear depolarization ratio (LDR), which is the ratio between the cross-polar power and the co-polar one, is widely used to classify different hydrometeors because of its sensitivity to their shape and orientation (Doviak and Zrnic, 2014). Currently, some weather radar systems, such as IDRA and POLDIRAD (Hagen and Meischner, 2000), and cloud radars (Li *et al.*, 2004; Sato and Okamoto, 2006; Beauchamp and Chandrasekar, 2016), are capable of measuring LDR. Normally, for cloud and precipitation targets, the cross-polar signal level is typically only 10^{-2} - 10^{-3} of the co-polar level (LDR is in the interval of $[-20, -30]$ dB). Additionally, LDR measurements are prone to contamination from noise and clutter, leading to the increase of its values. Hence, sLDR can be used to distinguish the precipitation from noise and clutter. As a single spectral polarimetric parameter, it has been shown by Unal (2009) that it was the most efficient in reducing different types of clutter.

DsLDR filter has been proposed for an atmospheric radar slantly or vertically profiling the troposphere and its full discussion can be referred to Unal (2009). For horizontally profiling weather radar, the technique has to be combined with another clutter suppression method. Its shortcoming lies in that the sLDR of precipitation and clutter overlap, making it impossible to thoroughly separate them. Moreover, it is not desirable that the narrow notch filter may suppress the precipitation whose radial velocity is around $0\,\mathrm{m\,s^{-1}}$ and the noise clipping may remove the light precipitation.

3.2.3. ARTIFACT ANALYSIS

The IDRA radar continuously scans the atmosphere, and its measurements are displayed in real time. Considering one radar measurement which occurred at 02:00 UTC on 1st July 2011, and applying the standard clutter suppression filtering method, the raw PPI and resulting PPI are shown in Fig. 3.1(a) and Fig. 3.1(b). This technique can reduce ground clutter, noise and part of the artifacts. However, the mitigation of artifacts is not sufficient, which may also conduct a relatively high false alarm in the radar PPI. In

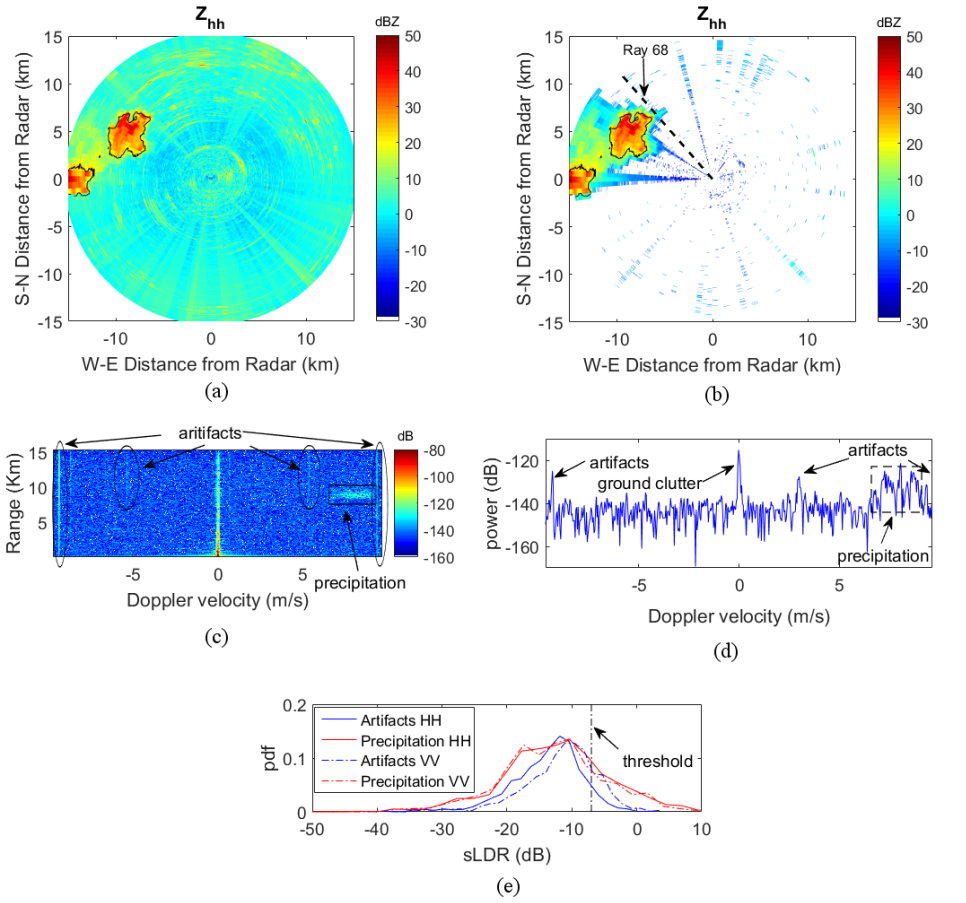

Figure 3.1: IDRA artifacts observation. Data measured at 02:00 UTC on 1st July 2011. (a) the raw reflectivity PPI display; (b) the reflectivity PPI display after the standard processing; (c) the raw range-Doppler spectrogram of Ray 68; (d) the raw Doppler spectrum of Range bin 300 (e.g. 9 km); (e) the distributions of *sLDR* of artifacts and precipitation.

the standard processing, the threshold of the DsLDR filter is set to −7 dB. It means that the Doppler bins related to a spectral linear depolarization ratio larger than −7 dB are discarded.

Considering the raw range-Doppler spectrogram of Ray 68 displayed in Fig. 3.1(c), some artifacts are along the whole range bins, and they are non-stationary and their Doppler velocities vary. Further, Range bin 300 (e.g. 9 km) is taken and its Doppler spectrum is plotted as shown in Fig. 3.1(d). We can see that the intensity of the precipitation is weaker compared with the artifacts and ground clutter. After integrating the whole Doppler bins resulting in one reflectivity value, the true reflectivity of precipitation will be biased by the artifacts and ground clutter. Moreover, the artifacts and precipitation are extracted and their $sLDR^{hh}$ and $sLDR^{vv}$ are calculated based on Eq.(3.1) as shown

in Fig. 3.1(e). From Fig. 3.1(e), the $sLDR$ distribution value of the precipitation indicated as the red line are [−40 dB, 12 dB] while these of the artifacts are [−30 dB, 0 dB], it is thus impossible to remove the artifacts when the threshold shown as the black dash line is set to −7 dB. Note that the $sLDR$ distribution of the precipitation in this case are largely increased by the effect of the low signal to noise ratio (SNR). In fact, in the case of low SNR precipitation, the cross-pol signal, $S_{hv}(v,r)$ and $S_{vh}(v,r)$, is not measured anymore, and only noise is measured. It means that $sLDR^{hh}$ and $sLDR^{vv}$ become an estimate of noise to signal ratio (NSR).

The spectral width property of the clutter and precipitation provides a way to remove all these clutter. After the statistical analysis of 10 cases (each case contains more than 140 rays) during the time period from 2011 to 2016, we come to the conclusion that the spectral width of artifacts is always 3-4 Doppler resolution bins (about 15 $\mathrm{cm\,s^{-1}}$) while that of ground clutter is 11-13 Doppler resolution bins (about 50 $\mathrm{cm\,s^{-1}}$). The ground clutter spectra after the DsLDR filter, are not fully removed. The remaining ground clutter spectra are discontinuous because of the partial removal of ground clutter Doppler bins, which is desirable for the newly-designed filter. As for the precipitation, its spectral width is generally large and the Doppler spectrum is continuous. However, after the DsLDR filter, some points inside the spectra will be missing. This is mainly attributed to the fact that the low SNR will lead to the increase of the $sLDR^{hh}$ and $sLDR^{vv}$ value. Fortunately, the missing part can be compensated by the mathematical morphology method which will be explained later. The details of the newly proposed filter in narrow-band clutter mitigation are discussed in the next section.

3.3. FILTER DESCRIPTION

The spectral properties can be used to distinguish precipitation from the narrow-band clutter in weather radar. Precipitation tends to be continuous across several range and Doppler bins in the range-Doppler domain. As for the feature of ground clutter, it is always static and centered around 0 ms^{-1} Doppler bin. While the artifacts of IDRA radar, exhibiting a spectral width less than 5 Doppler bins, appear continuously along the range bins and have an unpredictable position in one range-Doppler spectrogram. Based on all these features, the MDsLDR filter is proposed to remove the narrow-band clutter in spectral polarimetric radar. The method is mainly divided into four steps as shown in Fig. 3.2. The newly proposed filter is based on the range-Doppler spectrogram, thus it is a ray-by-ray process for radar PPI.

1. Step 1, the DsLDR filter is applied on the chosen spectrogram. The mask $M^{DsLDR} \in \{0,1\}$ that characterizes precipitation is expressed as

$$M^{DsLDR} = \begin{cases} 1, & if\ sLDR^{hh} < T_1,\ sLDR^{vv} < T_1 \\ 0, & otherwise \end{cases} \tag{3.2}$$

   where T_1 is the set threshold which can be related in function of the radar configuration and its environment. $M^{DsLDR} = 1$ represents the potential areas of precipitation.

   After the DsLDR filter, however, the majority of the radar artifacts remains. This is because their sLDR values are smaller than the threshold T_1 which has been illus-

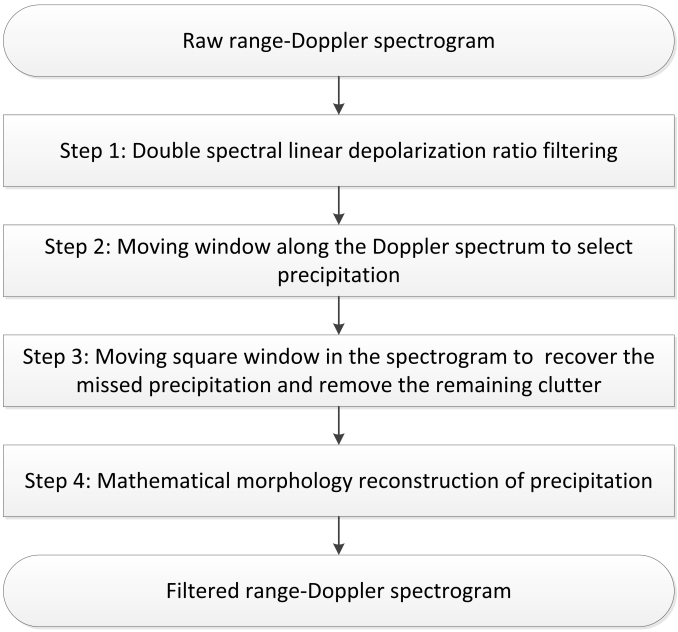

Figure 3.2: Flowchart of the moving double spectral linear depolarization ratio filter.

trated in Section 3.2. As for the ground clutter, their spectra become noncontinuous in the range-Doppler domain, which is favorable to Step 2. Additionally, some bins of the precipitation are eliminated, which is not desirable but can be compensated by the moving 2D window in Step 3 and the mathematical morphology method in Step 4.

2. Step 2, the moving window is applied along the Doppler domain to select precipitation. The $1 \times L$ Doppler moving window is set based on the analysis of the spectral width of the narrow-band clutter. Then the moving window is applied to the mask M^{DsLDR} obtained in Step 1. When the moving window traverses from the first bin to the last bin in one Doppler spectrum, the central bin as well as the $L/2$ bins before and after the chosen bin, altogether L bins, are considered as a whole. If there is 0 in any position of the moving window, the central bin is replaced with 0, otherwise maintained 1. With this process, a filtered mask $M^{filtered}$ is obtained. However, it will lead to the loss of some "1" areas when they locate in the boundary of the precipitation, which will be compensated in the next steps.

3. Step 3, the moving 2D window is applied in the spectrogram to recover the missed precipitation and further eliminate the clutter. With the process of Step 2, almost all the narrow-band clutter is removed, but unfortunately, some precipitation, especially those locating in the boundaries, is also discarded. To further eliminate the very few remaining environment clutter and recover the filtered precipitation, a moving 2D window sized $a \times b$ is applied to the filtered mask $M^{filtered}$. For each

bin in the mask $M^{filtered}$, we apply the center of the moving window aligning to the chosen bin, and then we have $a \cdot b$ chosen elements $\left[M_1^{filtered}, M_2^{filtered}, \cdots, M_{a \cdot b}^{filtered}\right]$. By summing them up and normalizing with the weight $1/a \cdot b$, we can get

$$K = \frac{1}{a \cdot b} \sum_{i=1}^{a \cdot b} M_i^{filtered} \tag{3.3}$$

With the weight, the calculated K is in the interval $[0, 1]$. The comparison between K and the set threshold T_2 is made to decide whether the chosen bin is 1 or 0.

$$M^{MDsLDR} = \begin{cases} 1, & if\ K > T_2 \\ 0, & otherwise \end{cases} \tag{3.4}$$

With this moving 2D window, it is possible to further remove the isolated bins in the filtered mask obtained in Step 2. Moreover, those points near the filtered "1" areas will be recovered. The selection of the length a and b of the moving window and the threshold T_2 will be discussed in the next section where the technique is applied to real radar data.

4. Step 4, the mathematical morphology method is adopted to further reconstruct the precipitation. After the previous three steps, some points inside the precipitation area as well as the points in the boundaries may be filtered out. Then the mathematical morphology which is particularly useful for the analysis of binary images can be used to recover them. The particular operator is the morphological closing whose function is removing small holes in the image processing. Closing is defined simply as a dilation followed by an erosion using the same structuring element for both operations. The details of the mathematical morphology method refer to Najman and Talbot (2013). The structuring element is set as the flat disk of radius r. The reason why the structuring element is set as the flat disk is that the precipitation areas are continuous in the range-Doppler spectrogram, and the flat disk is conducive to the smooth precipitation boundary recovery. The radius r should be properly set to recover sufficient precipitation bins.

3.4. APPLICATION TO RADAR DATA

3.4.1. PARAMETER SETTING

The parameters described in Section 3.3 are determined in this section for IDRA measurements. The threshold T_1 in Step 1 of the DsLDR filter applied to IDRA is -7 dB. The selection of T_1 is explained by Unal (2009). Specifically, T_1 is selected considering clutter and precipitation removal percentage versus different thresholds. The threshold T_1 may differ for another radar (e.g. $T_1 = -5$ dB for Transportable Atmospheric Radar (Unal, 2009)) because of different radar configuration and clutter. For example, a vertically profiling radar is less affected by ground clutter than a horizontally profiling one.

As for the length of the Doppler moving window L in Step 2, it depends on the spectral width of the narrow-band clutter, and L corresponds to the largest Doppler spectral

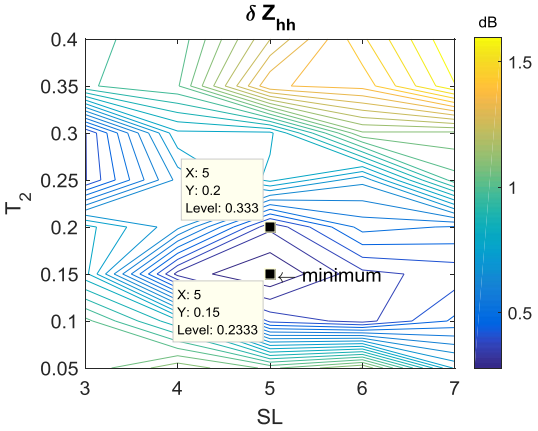

Figure 3.3: Average error reflectivity δZ_{hh} calculation based on different side length SL and threshold T_2.

width observed for this clutter. For IDRA in the operational mode with 512 sweeps for the Doppler processing, $L = 5$ (about $20\,\mathrm{cm\,s^{-1}}$).

In Step 3, with no loss of generality, the moving 2D window can be squared with size $a = b$. Then the choice of the side length SL of the moving square window as well as the threshold T_2 are important to recover the removed precipitation bins and eliminate the remaining clutter bins. On the one hand, the boundaries of precipitation in the range-Doppler domain will be removed in Step 2, so the threshold T_2 for the moving 2D square window should be small to recover more marginal precipitation. On the other hand, there is some isolated clutter remaining in the range-Doppler spectrogram, which should be further suppressed otherwise it will bring in more surrounding clutter with Step 4. In other words, the threshold T_2 should be large enough to further mitigate the isolated clutter. The later factor is dominant because the marginal precipitation affects less the final reflectivity calculation.

Next, the selection of side length SL and threshold T_2 will be explored in detail. The reflectivity derived from the range-Doppler spectrogram is proportional to the power sum along the Doppler bins. Supposing for a given spectrogram, we have R range bins with precipitation, and then a parameter named average error reflectivity δZ_{hh} is defined as

$$\delta Z_{hh} = \frac{1}{R} \sum_{r=1}^{R} \left| Z_{hh}^{true}(r) - Z_{hh}^{est}(r) \right| \tag{3.5}$$

where $Z_{hh}^{true}(r)$ is the true reflectivity value in the r^{th} range bin, and $Z_{hh}^{est}(r)$ is the filtered reflectivity value in the r^{th} range bin. Based on the δZ_{hh}, a method named the average error reflectivity minimization can be used to select the side length SL and threshold T_2.

Considering the spectrogram in Fig. 3.1(c) to calculate the $Z_{hh}(r)$ (r in the interval of 8.6 −9.1 km), the true $Z_{hh}^{true}(r)$ and the MDsLDR filtered $Z_{hh}^{est}(r)$ with $SL \in [3,7]$ with a step 1 and $T_2 \in [0.1, 0.4]$ with a step 0.05 are calculated. Furthermore, the δZ_{hh} is obtained and its contour map is depicted in Fig. 3.3. Note that the sweep number is 512 here.

From Fig. 3.3, it is concluded that similar average error reflectivity values may be obtained for different combinations of SL and T_2. Hence, one of these two parameters can be pre-set, and the other one can be selected based on the average error reflectivity minimization. L is used in Step 2 as the length of the moving window along the Doppler domain, while the selection of SL is the 2D window to further mitigate the isolated clutter and recover the marginal precipitation. The 2D window takes advantage of the continuity of precipitation in the range-Doppler domain. Thus, L and SL can be related to each other, and we set $L = SL$. From Fig. 3.3, with $SL = 5$ and $T_2 = 0.15$, we obtain the minimum $\delta Z_{hh} = 0.23$ dB, which is consistent with our analysis, namely pre-setting $SL = L$ and then exploring T_2 based on the average error reflectivity minimization. Note that such parameter selection may be optimal for the adopted spectrogram, and further validation should be implemented for other measurements. As discussed above, T_2 should be relatively large to mitigate more isolated background clutter. Hence, we set $SL = 5$ and $T_2 = 0.2$ whose corresponding $\delta Z_{hh} = 0.33$ dB is the final average reflectivity error for the spectrogram at high Doppler resolution. Furthermore, 10 cases (each case contains more than 140 rays) during the time from 2011 to 2016 are tested, and it verifies the effectiveness of the configuration of $SL = 5$ and $T_2 = 0.2$ for the operational mode. Some results are presented in Section 3.5.

Finally, in Step 4, the radius of the flat disk can be set as $r = L$. The reason is easy to understand. The radius of this structuring element used here is to recover the excessive removal of precipitation which is done in Step 2 with one moving window sized $1 \times L$. With $r = L$, it is expected the recovered precipitation can fully compensate the precipitation boundaries.

To reiterate, the parameter selection in the MDsLDR filter is based on radar configuration and the clutter property, e.g. spectral width. Apart from that, the parameters in Step 3 are also chosen based on the radar data. Normally, for the situations with different sweep numbers, the parameter selection procedure in Step 3 should be applied.

3.4.2. IMPLEMENTATION AND PERFORMANCE ANALYSIS

When the parameters are determined, the MDsLDR filter can be implemented according to the flowchart in Fig. 3.2. To better understand each step described in the block diagram, the corresponding spectrogram after each step is shown in Fig. 3.4. From Fig. 3.4(a), the spectrogram after the DsLDR filter is not desirable because there are radar artifacts as well as background noise and ground clutter remaining. In this case, the intensity of precipitation is so weak that it will be largely biased when Z_{hh} is calculated based on this result. Then with the moving window in the Doppler domain, Fig. 3.4(b) shows that all the artifacts, the majority of background noise and most of precipitation are mitigated. The precipitation removal is not favorable, which should be recovered later. In Fig. 3.4(c) , with the moving 2D window, the isolated noise is further reduced, and some precipitation is recovered. Finally, with the mathematical morphology reconstruction in Fig. 3.4(d), almost all the precipitation remains and all the artifacts, the noise, and the ground clutter are removed. From this spectrogram comparison, the newly proposed MDsLDR technique shows full artifacts, ground clutter and noise suppression.

To further make a comparison between the DsLDR filter and the MDsLDR filter, the Doppler spectra of Range bin 300 after the DsLDR and the MDsLDR filtering are pre-

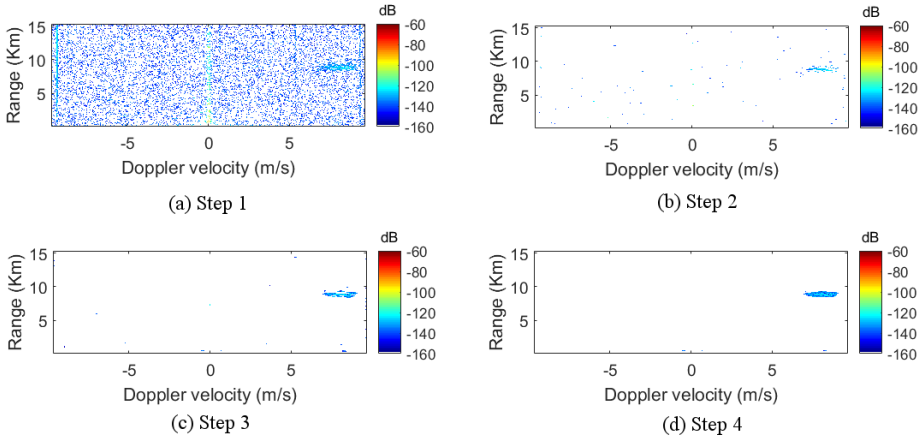

Figure 3.4: The output range-Doppler spectrogram after each step of the flowchart.

sented in Fig. 3.5(a). From Fig. 3.5(a), it is obvious that the MDsLDR filter has better clutter suppression performance than the DsLDR filter only. Additionally, the Doppler spectra of precipitation after the MDsLDR filter are continuous, and the DsLDR filtered ones have some missing data.

After having illustrated the effectiveness of the MDsLDR filter, it is necessary to quantitatively verify the performance of the technique. To quantify the results, the error reflectivity in the r^{th} range bin $\Delta Z_{hh}(r)$ is defined as

$$\Delta Z_{hh}(r) = Z_{hh}^{true}(r) - Z_{hh}^{est}(r) \tag{3.6}$$

The error reflectivity $\Delta Z_{hh}(r)$ and the average error reflectivity δZ_{hh} defined in Eq.(3.5) are used to characterize the filter performance. The morphological closing operator is an essential step in the MDsLDR filter, which will also be studied here. The true reflectivity, the DsLDR filtered reflectivity, and the MDsLDR filtered reflectivity with and without the mathematical morphology process, are displayed in Fig. 3.5(b). Note that the "MDsLDR no MM" in the legend means the MDsLDR filter without the mathematical morphology process.

From Fig. 3.5(b), the mathematical morphology process plays an indispensable role in the precipitation recovery, especially for the precipitation boundaries. The maximum error reflectivity $\Delta Z_{hh}(r)$ and the average error reflectivity δZ_{hh} of the MDsLDR filter is 1.09 dB and 0.33 dB. While these errors between the MDsLDR filter without the mathematical morphology process and true reflectivity are 3.66 dB and 1.03 dB. The maximum $\Delta Z_{hh}(r)$ difference with and without the mathematical morphology process is as high as 2.57 dB. As for the DsLDR filtered reflectivity, its average error reflectivity is 1.63 dB, which is the worst among the three filters. Additionally, its reflectivity is always larger than the true reflectivity. The reason is the residual ground clutter and artifacts remaining because of the incomplete filtering as indicated in Fig. 3.5(a). It can be concluded that the Z_{hh} obtained from the MDsLDR filter with the mathematical morphology process is the best fit to the true Z_{hh}. Note that the true reflectivity is around 0 dBZ, corre-

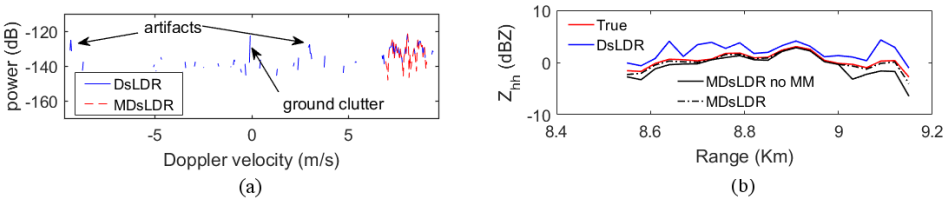

Figure 3.5: The performance comparison between the DsLDR filter and the MDsLDR filter. (a) the filtered Doppler spectrum of Range bin 300; (b) the Z_{hh} comparison.

sponding to very light precipitation.

The above analysis validates the good performance of the MDsLDR filter applied to the range-Doppler spectrogram. For the operational polarimetric radar, the filtered observables displaying in the PPI are required. Hence, by applying the MDsLDR filter to all the spectrograms in one PPI, we calculate the reflectivity Z_{hh}, differential reflectivity Z_{dr} and linear depolarization ratio (LDR) as shown in Fig. 3.6(b), 3.6(d) and 3.6(f), respectively. Making a comparison with the standard processing results based on the DsLDR filter as shown in Fig. 3.6(a), 3.6(c) and 3.6(e), almost all the precipitation remains while the artifacts are suppressed with the MDsLDR filter. Furthermore, the scatter plot of the MDsLDR filtered Z_{hh} and the Z_{hh} after the standard processing is shown in Fig. 3.6(g). It indicates that the artifacts have a larger impact on Z_{hh} smaller than 0 dBZ which usually corresponds to light precipitation or drizzle.

To further quantify the filtering performance of the MDsLDR filter in the PPI, the clutter suppression ratio Z_{hh}^{CSR} expressed in dB is defined as

$$Z_{hh}^{CSR} = Z_{hh}^{original} - Z_{hh}^{MDsLDR} \tag{3.7}$$

where $Z_{hh}^{original}$ is the original reflectivity without any filtering, and Z_{hh}^{MDsLDR} is the reflectivity after the MDsLDR filtering. The histogram of the clutter suppression ratio Z_{hh}^{CSR} is shown in 3.6(h). The maximum clutter suppression ratio is as high as 43.0 dB dB for this adopted case occurred at 02:00 UTC on 1st July 2011.

Note that the polarimetric features of artifacts can be low Z_{hh} (around 0 dBZ), large Z_{dr} (around 1 dB) and low LDR (around −15 dB), which are typical precipitation features. These comparisons verify the effectiveness of the proposed filter for artifact mitigation especially in the presence of light precipitation. It is foreseeable that the MDsLDR filter improves the data quality of polarimetric weather radar and makes the measured data available for further application. However, other precipitation cases have to be considered for an independent evaluation, which will be shown in Section 3.5.

3.4.3. IMPACT OF THE DOPPLER RESOLUTION

The current operational weather radars tend to scan faster to update the atmospheric changes in shorter time. This means a shorter dwell time for the Doppler processing. This section will further verify the effectiveness of the MDsLDR filter regarding different Doppler resolutions.

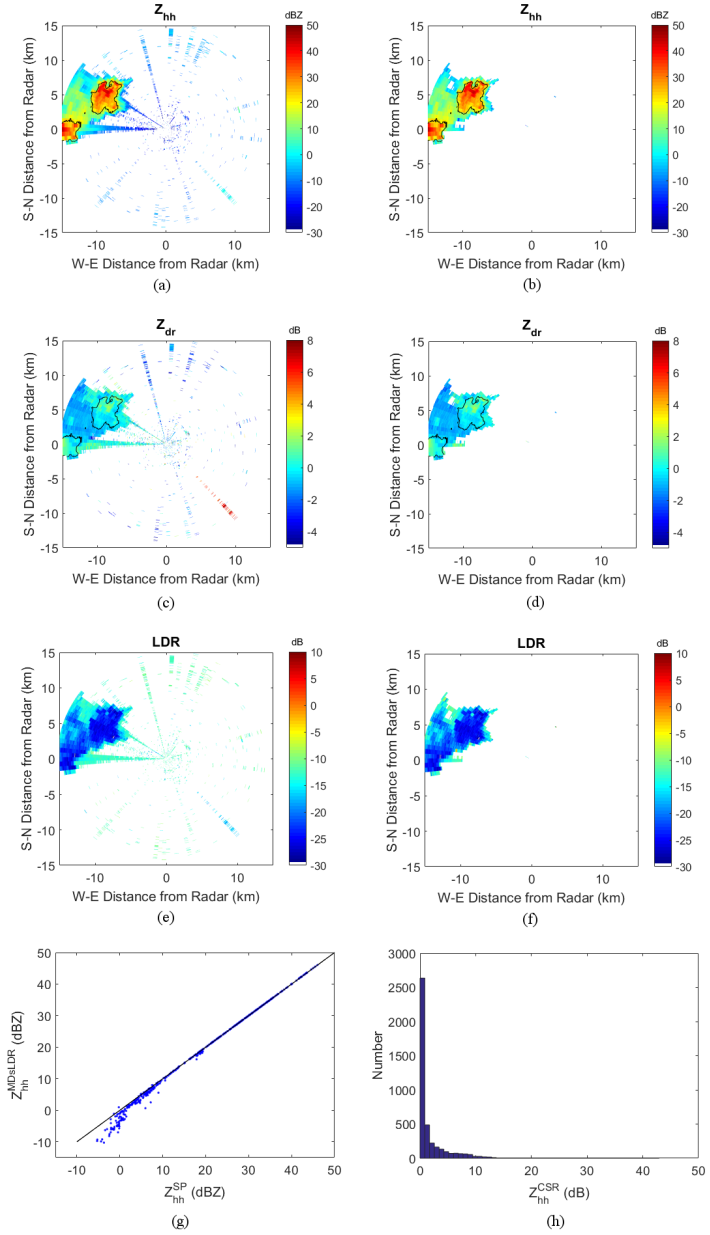

Figure 3.6: PPI comparison between the standard processing and the MDsLDR filter. Data measured at 02:00 UTC on 1st July 2011. (a) Z_{hh} after the standard processing; (b) Z_{hh} after the MDsLDR filter; (c) Z_{dr} after the standard processing; (d) Z_{dr} after the MDsLDR filter; (e) LDR after the standard processing; (f) LDR after the MDsLDR filter; (g) Z_{hh} comparison between the MDsLDR filter and the standard processing; (h) Clutter suppression ratio distribution.

Using the same data measured at 02:00 UTC on 1st July 2011, we set the sweep number to 512, 256, 128, and 64 to explore the performance of the MDsLDR filter. Since the total sweep number of one PPI is fixed, to get the same data for comparison, the increasing multiple of the ray number is the same with the decreasing multiple of sweep number in the data selection. As for the selection of L, it is obtained by the observation of spectral width of the narrow-band clutter in the range-Doppler spectrogram. Finally, as discussed in Section 3.4.1, by setting $SL = L$, the T_2 is determined based on the average error reflectivity minimization. The results of parameter selection are shown in Table 3.2.

Table 3.2: MDsLDR parameter selection for different Doppler resolutions.

Sweep number	Doppler velocity resolution (m/s)	Ray No	L	T_2	SL
512	3.8×10^{-2}	68	5	0.2	5
256	7.5×10^{-2}	135	4	0.2	4
128	1.5×10^{-1}	269	3	0.3	3
64	3.0×10^{-1}	537	3	0.35	3

With the parameter selection in Table 3.2, another measurement should be used to verify the filter effectiveness. Data measured at 12:00 UTC on 1st July 2011 are selected, and Ray 142, 284, 568, and 1136 are considered for different Doppler velocity resolutions. The results are shown in Fig 3.7. From Fig 3.7(a)-(d), we can observe that the MDsLDR filter can preserve almost the precipitation while removing all the clutter. These results further verify that MDsLDR filter can be adopted for different Doppler velocity resolutions. Note that, in this case, when the ground clutter overlaps with precipitation, MDsLDR cannot mitigate the ground clutter, and other technique should be used to resolve this situation.

3.5. OTHER CASES STUDY

3.5.1. APPLY TO SEVERE-STORM CASE

To assess the MDsLDR filter, a case of a severe storm is illustrated here. The data measurement occurred at 14:45 UTC in 3rd January 2012 when a cold-season organized storm crossed the Netherlands from the northwest to the southeast. The IDRA radar observed reflectivity signatures such as hook echo and weak echo region which are associated with supercell vortices. A successful clutter suppression method should retain this important reflectivity signature while mitigating the unwanted clutter.

Fig. 3.8(a) and Fig. 3.8(b) are the PPI after the standard processing and the MDsLDR filter, respectively. From the comparison of them, it seems that they are almost the same. In particular the important reflectivity signature — hook echo remains. This is consistent with above analysis — the artifacts affect less large reflectivity zone. The only difference is that some areas in the PPI are free of echoes with the MDsLDR filter. In this case, it is difficult to judge which filter results in better clutter suppression performance. Hence, an inspection of the spectrogram is necessary, and Ray 45 is used here.

Compared with the MDsLDR filtered spectrogram as shown in Fig. 3.8(d), the stan-

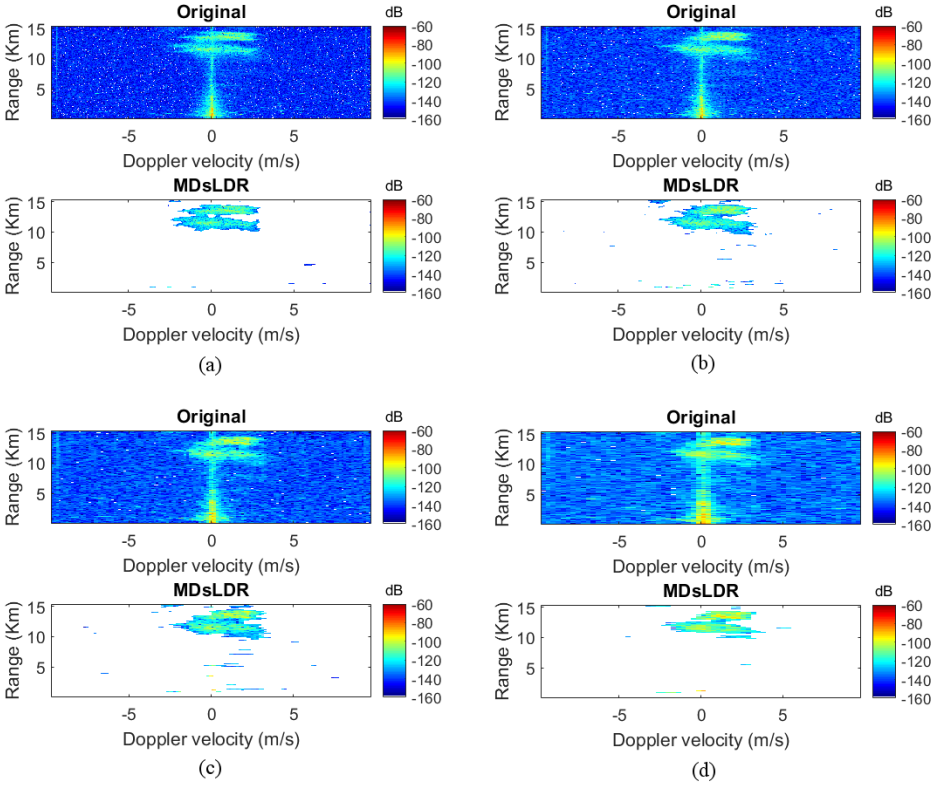

Figure 3.7: The MDsLDR filter applied to radar data with different Doppler resolutions. (a) Sweep number 512; (b) Sweep number 256; (c) Sweep number 128; (d) Sweep number 64.

dard processing filtered spectrogram in Fig. 3.8(c) has an inferior performance. Specifically, after the standard processing, some of the artifacts remain, and some light precipitation is also reduced by the fixed notch filter. While for the MDsLDR filter, all the artifacts and the ground clutter which is not overlapping with precipitation are discarded. Additionally, almost all the areas with precipitation in the range-Doppler domain are maintained.

Finally, the scatter plot of the MDsLDR filtered Z_{hh} and the Z_{hh} after the standard processing is shown in Fig. 3.8(e). Normally, the standard processing filtered Z_{hh} has a larger value than the MDsLDR filtered one because of the residual artifacts. However, in this case where ground clutter and precipitation overlap for some range bins, the Z_{hh} after the standard processing has a smaller value. This is because the notch filter adopted in the standard processing will remove all the ground clutter while the MDsLDR filter will retain the ground clutter overlapping with precipitation. This is illustrated in Fig. 3.8(d) and Fig. 3.8(c). Then it is concluded that the MDsLDR filter cannot resolve the situation of ground clutter overlapping with precipitation, which means another technique should be combined. The histogram of the clutter suppression ratio is shown in

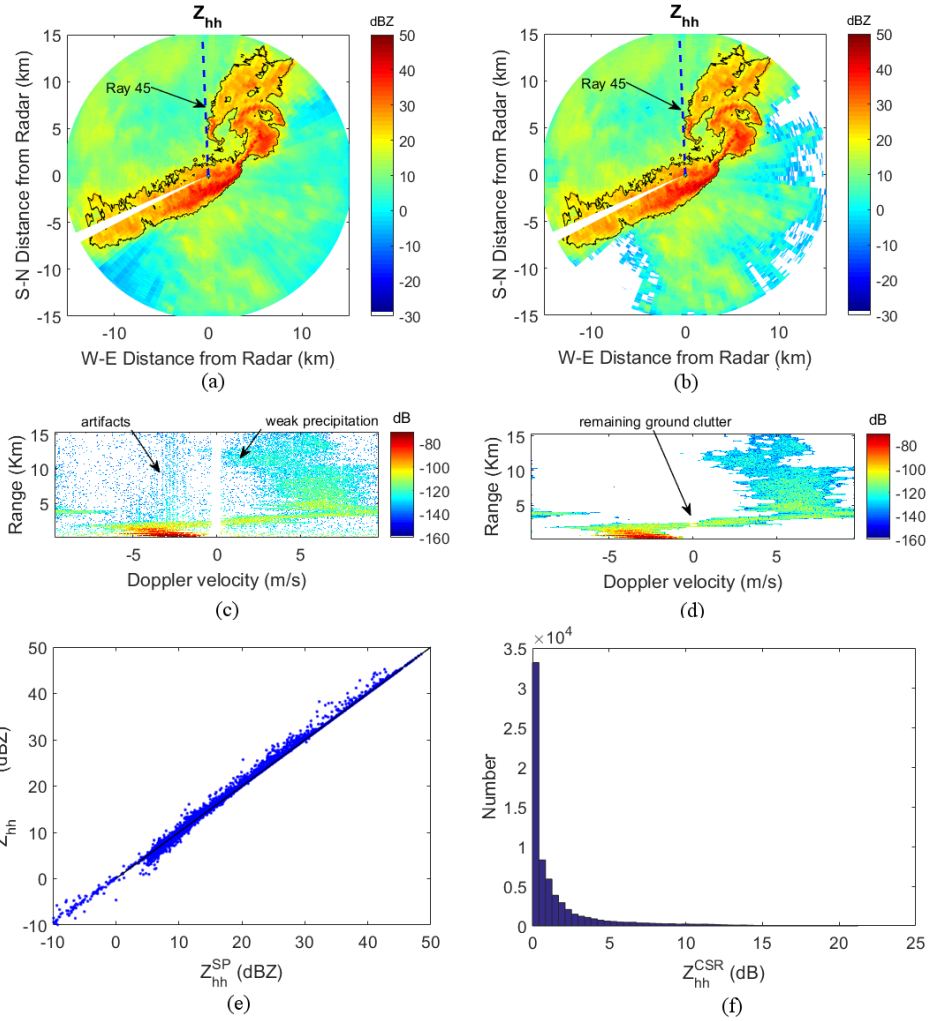

Figure 3.8: A severe-storm case. Data measured at 14:45 UTC on 3rd January 2012. (a) Z_{hh} after the standard processing; (b) Z_{hh} after the MDsLDR filter; (c) spectrogram of Ray 45 after the standard processing; (d) spectrogram of Ray 45 after the MDsLDR filter; (e) Z_{hh} comparison between the MDsLDR filter and the standard processing; (f) Clutter suppression ratio distribution.

Fig. 3.8(f). Note that the maximum clutter suppression ratio, in this case, is 21.2 dB.

3.5.2. APPLY TO SEVERE-ARTIFACTS CASE

To further verify the performance of the newly proposed method in narrow-band clutter removal, another case with severe artifacts is used here. The case occurred at 12:00 UTC on 15th January 2016. The results of Z_{hh} and Z_{dr} after the standard processing and the MDsLDR filter are shown in Fig. 3.9. Apart from these PPI displays, a further check of

Ray 69 and the scatter plot of Z_{hh} between the two techniques are also included.

From Fig. 3.9(a) and 3.9(c), we can see artifacts severely contaminate the reflectivity Z_{hh} and the differential reflectivity Z_{dr}. While after the MDsLDR filtering, a better artifact suppression can be achieved as shown in Fig. 3.9(b) and 3.9(d). However, for the differential reflectivity Z_{dr}, the azimuthal discontinuities are still present. They are not the result of artifacts. The reason behind this may be attributed to the security fence locating near the radar system. This speculation is based on the similar problem which is well documented for the Meteo-France C-band polarimetric radar (Gourley *et al.*, 2006). Further research should be conducted to improve the quality of the differential reflectivity.

The Ray 69 is extracted, and its corresponding range-Doppler spectrogram is further processed with the standard processing and the MDsLDR filter. The labeled artifacts in Fig. 3.9(e) indicate the insufficient artifact mitigation for the standard processing. In this case, the artifacts have larger intensity than the weak precipitation. Compared with the standard processing, Fig. 3.9(f) shows that the MDsLDR filter suppresses more artifacts, ground clutter, and noise at the price of partial removal of weak signal.

Finally, the scatter plot of the MDsLDR filtered Z_{hh} and the Z_{hh} after the standard processing is displayed in Fig. 3.9(g). It shows that the reflectivity whose intrinsic values are less than 0 dB is estimated smaller with the MDsLDR filter. This conclusion is consistent with the case in Fig. 3.6 and the reason behind this phenomenon is the good artifact mitigation performance of the newly proposed method. The histogram of the clutter suppression ratio is shown in Fig. 3.9(h). Note that the maximum clutter suppression ratio, in this case, is 49.5 dB.

3.6. CONCLUSION

This paper proposes a new clutter suppression method named moving double spectral linear depolarization ratio (MDsLDR) filter to remove the stationary and non-stationary narrow-band clutter in the spectral polarimetric radar. The MDsLDR filter relies on the Doppler spectral width and polarimetric properties of precipitation and clutter. This filter is mainly divided into four steps. Firstly, a mask indicating the precipitation is obtained from the double spectral linear depolarization ratio filter. Secondly, a moving Doppler window is applied to the mask to further select precipitation. Thirdly, a moving 2D window is implemented to recover the removed precipitation and eliminate the remaining clutter. Finally, the mathematical morphology method is adopted to further reconstruct the precipitation area. The performance of the newly proposed method is verified qualitatively and quantitatively with the IDRA radar data, namely cases of moderate/light precipitation, storm with hook-echo signature and light precipitation with severe artifact contamination. The MDsLDR filter has clutter suppression ratio as high as 49.5 dB. Moreover, its effectiveness is verified for different Doppler velocity resolutions. This filter can remove the artifacts, the noise and ground clutter which are not overlapping with precipitation. For the case of the ground clutter mixed with precipitation, it should combine with another technique, such as the Gaussian model adaptive processing (GMAP). The MDsLDR filter is also verified on cases in the period from 2011 to 2016, and it shows robustness in artifacts, noise and ground clutter suppression. Another advantage is that the MDsLDR filter is easy to implement, and it has relatively

low computation complexity. Therefore the technique can be applied in real time. It is foreseeable that this new filter can mitigate other moving narrow-band clutter such as airplanes, cars, and trains in spectral polarimetric weather radar. More research can be done in this direction in the future.

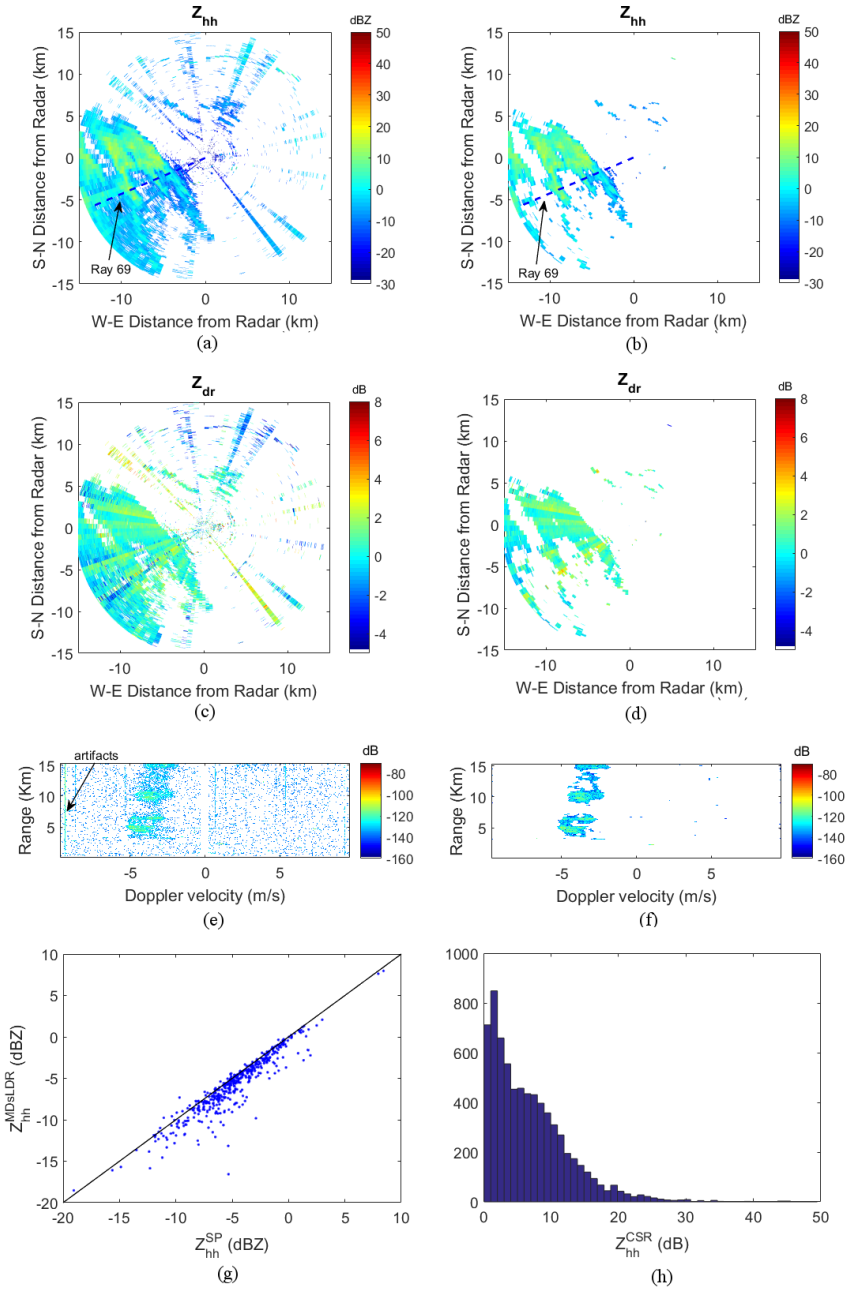

Figure 3.9: A severe-artifacts case. Data measured at 12:00 UTC on 15th January 2016. (a) Z_{hh} after the standard processing; (b) Z_{hh} after the MDsLDR filter; (c) Z_{dr} after the standard processing; (d) Z_{dr} after the MDsLDR filter; (e) spectrogram of Ray 69 after the standard processing; (f) spectrogram of Ray 69 after the MDsLDR filter; (g) Z_{hh} comparison between the MDsLDR filter and the standard processing; (h) Clutter suppression ratio distribution.

4

Object-orientated Filter Design in Spectral Domain for Polarimetric Weather Radar

---

This chapter has been published as:

Jiapeng Yin, Christine Unal, and Herman Russchenberg. "Object-orientated Filter Design in Spectral Domain for Polarimetric Weather Radar", *IEEE Trans. Geosci. Remote Sens.*, 57(5):2725-2740, 2019.

The technique described in Chapter 3 can only be used in polarimetric weather radar with cross-polar measurements, which limits its application to most dual-polarization radar systems. To alleviate this problem, this chapter introduces one filter named the object-orientated spectral polarimetric (OBSpol) filter to remove the same clutter mentioned in Chapter 3. Based on the spectral polarimetric features and spectral continuity of precipitation and clutter, the OBSpol filter generates a filtering mask implementing on the range-Doppler spectrogram to remove the clutter. Due to the more advanced signal processing method used in the OBSpol filter design, it can achieve good clutter mitigation performance and keep weaker precipitation.

Except the introduction is given in Section 4.1, the reminder of this chapter is organized as follows. In Section 4.2, the spectral polarimetric observables and the details of the proposed clutter suppression method are introduced. Then, using radar measurements, radar clutter analysis, filter parameter selection and filter implementation are discussed in Section 4.3. In Section 4.4, the OBSpol filter performance is compared with another technique (i.e., the MDsLDR filter introduced in Chapter 3) and evaluated in the spectrogram and PPI. In addition, the effectiveness of the OBSpol filter with different

Doppler velocity resolutions is explored. Finally, some conclusions are drawn in Section 4.5.

4.1. INTRODUCTION

Weather radar, sensing precipitation with high spatial and temporal resolution, is well recognized as an indispensable tool for atmospheric observation (Doviak and Zrnic, 2014). Upgrading to the polarimetric Doppler ability (Doviak *et al.*, 2000), weather radar can simultaneously record microphysical and dynamical features of precipitation, which largely improves its performance in quantitative precipitation estimation (QPE) (Chen and Chandrasekar, 2015; Chen *et al.*, 2017). Weather radar data have also been used to forecast severe storms such as tornadoes and hurricanes (Rezacova *et al.*, 2007). Additionally, the pluvial urban flood, which is caused by extreme rainfall and now a major societal hazard (Huong and Pathirana, 2013), can be predicted using radar measurements (Hamidi *et al.*, 2017). Not only is monitoring large-intensity precipitation important, but also the weak precipitation such as drizzle. Accurate measurements of drizzle rates will improve our understanding of cloud life time, which is critical to climate change studies (Stocker *et al.*, 2013).

Generally, the prerequisite of using radar data for the QPE application is the sufficient measurement accuracy which is always affected by unwanted echoes, namely radar clutter. However, compared with heavy precipitation, light precipitation may be easily removed by clutter mitigation methods. Hence, effective clutter suppression method should be developed to mitigate the clutter while keeping the precipitation regardless of its intensity.

Weather radar clutter mainly divides into two categories according to the Doppler velocity: stationary and non-stationary. One of the well-known stationary clutter (i.e., ground clutter) mitigation technique is named as the Gaussian model adaptive processing (GMAP) (Siggia and Passarelli Jr, 2004) which is introduced to resolve the problem when precipitation and ground clutter overlap. However, when GMAP is implemented on data without ground clutter contamination, it will result in some signal loss. Hence, ground clutter detection algorithms should be used before the application of GMAP. Integrating the clutter detection and filtering in one algorithm, the Clutter Environment Analysis using Adaptive Processing (CLEAN-AP) is put forward (Warde and Torres, 2014). Compared with GMAP, CLEAN-AP has a better clutter suppression performance, and the variance of estimates is diminished because of the usage of both magnitude and phase for proper notch width determination (Torres *et al.*, 2012). Nonetheless, GMAP and CLEAN-AP are not mitigation methods for moving clutter such as biomass and vehicles.

The non-stationary clutter for weather radar consists of flying biomass such as birds and insects, moving sea waves, variable radio frequency interference, and dynamic wind turbines. The feature studies of birds and insects are well documented by Stepanian and Horton (2015); Zrnic and Ryzhkov (1998); Melnikov *et al.* (2014, 2015). Additionally, combining image processing techniques and the fuzzy logic algorithm, the sea and chaff clutter mitigation technique is proposed by (Alku *et al.*, 2015). The weather radar performance is significantly deteriorated by wind turbines because of the large-intensity backscattering from the large tower and rotating blades (Yin *et al.*, 2017a; Isom *et al.*, 2009).

Techniques such as interpolation (Kong *et al.*, 2012; Nai *et al.*, 2013), signal decomposition (Uysal *et al.*, 2014, 2016) and machine learning (Nepal *et al.*, 2015), are developed to remove the wind turbine clutter. Last but not least, the radio frequency interference arising from the radio local area network is also an annoying interference that brings the disturbances such as dots, spokes and spikes in the radar plan position indicator (PPI) (Saltikoff *et al.*, 2016). Similarly, artifacts caused by radar system itself also affect the usage of radar data. Most of the time, the artifacts are speckles along many range bins in some azimuth directions in the PPI. Moreover, these speckles are non-stationary when observed in the Doppler domain, making it impossible to mitigate them with the conventional clutter suppression methods. These artifacts affect not only the reflectivity but also the Doppler and polarimetric measurements. For example, artifacts have influenced the polarimetric Doppler X-band radar IRCTR Drizzle Radar (IDRA) since its installation in 2007, which is well illustrated by Yin *et al.* (2017b, 2018). Also, the high-resolution polarimetric Doppler X-band radar MESEWI suffers from this problem (Krasnov and Yarovoy, 2016), and so do the Bonn X-band radar systems. This specific type of moving clutter is studied in this paper.

A novel clutter suppression method named the object-orientated spectral polarimetric (OBSpol) filter is proposed to remove both stationary and non-stationary clutter while retaining as much precipitation as possible regardless of its intensity. Based on the spectral polarimetric feature and the range-Doppler continuity of precipitation, the OBSpol filter is implemented in the range-Doppler spectrogram (i.e., one ray in the radar PPI) to mitigate the clutter and noise. Generally, precipitation is continuous in the range-Doppler domain, and the OBSpol filter groups the contiguous bins into different independent objects after the spectral polarimetric filtering and the mathematical morphology method. Then, an extra observable is chosen to mitigate the clutter based on the separated objects. Since the ray-by-ray clutter mitigation technique is computationally efficient, it can be implemented in real-time. In addition, the selected spectral polarimetric feature and extra observable can be a conventional variable of dual-polarization weather radar. Note that the term "conventional variable" refers to all variables available from a dual-polarization radar which does not have cross-polar measurements, including the standard moments (i.e., reflectivity, Doppler velocity and spectral width) and the polarimetric observables (i.e., differential reflectivity, differential phase and copolar correlation coefficient). Thus, the proposed clutter mitigation technique can be designed for dual-polarization operational weather radar.

Specifically, this paper will focus on the application of the OBSpol filter to IDRA narrow-band clutter (both moving and stationary) mitigation and weak precipitation preservation. In this case, the extra observable will be the spectral width. The IDRA clutter can be also mitigated by a method named the moving double spectral linear depolarization ratio (MDsLDR) filter (Yin *et al.*, 2017b). However, the MDsLDR filter requires measurements of a full-polarimetric weather radar. Hence, it is imperative to investigate one clutter mitigation method to remove the clutter and keep the weak precipitation for dual-polarization weather radar without cross-polar measurements. The OBSpol filter is put forward as an alternative for such purpose. Similar spectral processing method, however not polarimetric, in mitigating ground clutter and narrow-band interference for wind profiler radar is addressed by Morse *et al.* (2002).

4.2. OBJECT-ORIENTATED SPECTRAL POLARIMETRIC FILTER

4.2.1. SPECTRAL POLARIMETRIC OBSERVABLES

Based on the combined simultaneous Doppler and polarization information, spectral polarimetry exhibits the microphysical and dynamical properties of the target. This is favorable to retrieve atmospheric microphysical information and to mitigate non-atmospheric echoes. Following the backscatter alignment convention, the spectral reflectivity which relates to the range r and Doppler velocity v is expressed as

$$sZ_{xy}(r,v) = C \cdot sP_{xy}(r,v) \cdot r^2 = C \cdot \left|S_{xy}(r,v)\right|^2 \cdot r^2 \tag{4.1}$$

where $S_{xy}(r,v)$ represents the complex Doppler velocity spectrum in range bin r with a transmitted y polarization and a receiving x polarization, x and y being horizontal polarization (i.e., h) or vertical polarization (i.e., v). In addition, $sP_{xy}(r,v)$ is defined as spectral power, C is the calibration constant.

Accordingly, we can define the spectral differential reflectivity sZ_{dr}, the spectral linear depolarization ratio $sLDR^{hh}$ and $sLDR^{vv}$, and the spectral copolar correlation coefficient $s\rho_{co}$ as

$$sZ_{dr}(r,v) = 10log_{10}\left(\frac{sZ_{hh}(r,v)}{sZ_{vv}(r,v)}\right) \tag{4.2}$$

$$\begin{aligned} sLDR^{hh}(r,v) &= 10log_{10}\left(\frac{sZ_{vh}(r,v)}{sZ_{hh}(r,v)}\right) \\ sLDR^{vv}(r,v) &= 10log_{10}\left(\frac{sZ_{hv}(r,v)}{sZ_{vv}(r,v)}\right) \end{aligned} \tag{4.3}$$

$$s\rho_{co}(r,v) = \frac{\left|\left\langle S_{hh}(r,v)\, S^*_{vv}(r,v)\right\rangle\right|}{\sqrt{\left\langle |S_{hh}(r,v)|^2\right\rangle \left\langle |S_{vv}(r,v)|^2\right\rangle}} \tag{4.4}$$

where $\langle\rangle$ represents the averaging in range or Doppler, and the latter is chosen in this paper. Note that there is no averaging for other observables except $s\rho_{co}$. The averaging makes the spectral polarimetric observables with lower variability, leading to thresholding technique working better in precipitation and clutter separation. However, the averaging will also broaden the clutter to its neighboring bins in the range-Doppler domain, resulting in incomplete clutter removal.

sZ_{dr} is a good indicator of the shape of hydrometeors, and it should be larger than 0 dB for oblate particles such as raindrops. It has also been investigated for clutter suppression by Bachmann and Zrnić (2007) to separate bird and insect echoes for wind retrievals. As for $sLDR^{hh}$ and $sLDR^{vv}$, they are prone to contamination from clutter and noise, resulting in the increase of their values. Hence, $sLDR$ can be used to distinguish the precipitation from clutter and noise. They have been used to mitigate clutter for an S-band atmospheric radar slantwise or vertically profiling the troposphere (Unal, 2009). The $sLDR$ thresholding technique is enhanced for an X-band horizontally scanning radar (Yin *et al.*, 2017b). However, most dual-polarization operational weather radar systems (e.g., WSR-88D (Crum and Alberty, 1993)) cannot measure the cross-polar backscattering. $s\rho_{co}$, which also proved to be an efficient classification observable (Moisseev and Chandrasekar, 2009), is available for most polarimetric radar sys-

tems. The spectral copolar correlation coefficient $s\rho_{co}$ is very close to 1 for most hydrometeors and significantly lower than 1 for non-meteorological scatterers measured by the sidelobes of the antenna. However, for ground clutter, values of $s\rho_{co}$ are similar to that of precipitation while values of $sLDR$ differ. This means that as a single spectral polarimetric parameter, $sLDR$ is the most efficient in reducing different types of clutter (Unal, 2009). To explore an effective clutter mitigation method for dual-polarization weather radar without cross-polar measurements, $s\rho_{co}$ is considered. However, to use $s\rho_{co}$ for both stationary and moving clutter mitigation, other techniques should be combined, which will be described in detail next.

After the spectral polarimetric filtering which is going to be proposed and discussed in this paper, only the bins representing atmospheric signal are kept. Then, the standard moments and polarimetric observables can be calculated. The reflectivity in range bin r is expressed as

$$Z_{hh}(r) = C \cdot \sum_{v \in atm} (sP_{hh}(r,v) - sN) \cdot r^2 \tag{4.5}$$

where $v \in atm$ signifies that only those Doppler bins that contain atmospheric signal are used. sN is the spectral noise for the chosen spectrogram. By grouping all the power bins of sP_{xy} in a histogram, the power bin related to the largest number frequency will be regarded as the estimated spectral noise. The spectrogram-by-spectrogram noise estimation is inspired by (Ivić *et al.*, 2013), which is proposed to accurately produce estimates of the system noise power. In addition, the radial velocity $\bar{v}$ and spectral width σ_v can be expressed as

$$\bar{v}(r) = \frac{1}{Z_{hh}(r)} \sum_{v \in atm} v \cdot sZ_{hh}(r,v) \tag{4.6}$$

$$\sigma_v(r) = \sqrt{\frac{1}{Z_{hh}(r)} \sum_{v \in atm} (v - \bar{v}(r))^2 \cdot sZ_{hh}(r,v)} \tag{4.7}$$

Finally, the copolar correlation coefficient is defined as

$$\rho_{co}(r) = \frac{\left|\sum_{v \in atm} \left\langle S_{hh}(r,v)\, S^*_{vv}(r,v) \right\rangle\right|}{\sqrt{\sum_{v \in atm} \left\langle |S_{hh}(r,v)|^2 \right\rangle \sum_{v \in atm} \left\langle |S_{vv}(r,v)|^2 \right\rangle}} \tag{4.8}$$

These four radar observables will be evaluated after the application of the proposed filter in Section 4.4.

4.2.2. FILTER DESCRIPTION

Taking advantage of the spectral-polarimetric feature and the range-Doppler continuity of precipitation, the OBSpol filter is implemented in the range-Doppler spectrogram. This clutter mitigation technique contains 4 steps, and its flowchart is given in Fig. 4.1. The input of the OBSpol filter is the raw range-Doppler spectrogram while the output will be the filtered one. The raw range-Doppler spectrogram is obtained by applying the Fourier transform along the sample time with a Hamming window.

(a) Step 1, one precipitation mask is obtained by the spectral polarimetric filtering.

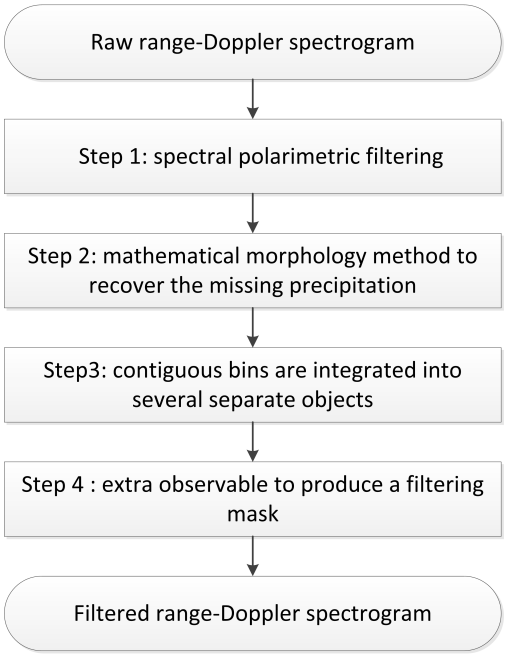

Figure 4.1: Flowchart of the objected-orientated spectral polarimetric filter.

sLDR IS NOT AVAILABLE

For dual-polarization radar systems without cross-polar measurements, the spectral copolar correlation coefficient $s\rho_{co}$ is always available. Filtered by the $s\rho_{co}$, the binary mask $M^{s\rho_{co}} \in \{0,1\}$ indicating precipitation is expressed as

$$M^{s\rho_{co}} = \begin{cases} 1, & if\ s\rho_{co} > T_1 \\ 0, & \text{otherwise} \end{cases} \tag{4.9}$$

where the threshold T_1 can be set based on the clutter and precipitation removal percentage. Since ground clutter and precipitation have a similar $s\rho_{co}$ value distribution, $M^{s\rho_{co}}$ will keep ground clutter, which means that another ground clutter mitigation method should be added. The narrow notch filter around $0\,\mathrm{m\,s^{-1}}$ or even more advanced techniques such as GMAP and CLEAN-AP can be used to remove the ground clutter. With such implementation, a ground clutter mitigation mask $M^{GCM} \in \{0,1\}$ where "0" indicates ground clutter will be developed. Note that the spectral copolar correlation coefficient filtering is implemented on the whole spectrogram while the ground clutter mitigation is only concentrated around $0\,\mathrm{m\,s^{-1}}$, and the remaining bins will be set to "1" in M^{GCM}. Then, after the completion of Step 1, one binary mask $M^{step1} \in \{0,1\}$ can be obtained, expressed as

$$M^{step1} = M^{s\rho_{co}} \times M^{GCM} \tag{4.10}$$

sLDR IS AVAILABLE

For radar systems with full-polarimetric measurement capability, the spectral linear depolarization ratio $sLDR$ can be used to mitigate the clutter, moving and stationary. Then, the binary filtering mask in Step 1 can be directly obtained and expressed as

$$M^{step1} = \begin{cases} 1, & if\ sLDR^{hh} < T_2,\ sLDR^{vv} < T_2 \\ 0, & \text{otherwise} \end{cases} \tag{4.11}$$

where the threshold T_2 is set based on clutter and precipitation removal percentage.

The precipitation mask M^{step1} is obtained based on the spectral polarimetric features of precipitation and clutter, which may cause some precipitation loss due to the low signal to noise ratio (SNR). When the SNR is low, the spectral polarimetric values of precipitation and clutter tend to overlap. Using a fixed thresholding method in Step 1, it may remove weak precipitation. The relation between spectral polarimetric observable value distributions and SNR will be given later combined with radar measurements. Additionally, some noise will be kept, which will be removed in the following steps.

(b) Step 2, the mathematical morphology method is used to recover the missing precipitation.

The mathematical morphology which is widely used in the binary image analysis can be used to recover the missing precipitation. The basic morphological operators contain erosion, dilation, opening and closing (Soille, 2013), and specifically closing is selected here. Closing is defined as the combination of dilation followed by erosion. Dilation operator with proper structuring element fills the holes inside M^{step1}, but extends the perimeter of the range-Doppler areas with value "1", which can be restored by performing the erosion operator with the same structuring element. A structuring element is a shape, used to probe or interact with a given image, with the purpose of drawing conclusions on how this shape fits or misses the shapes in the image. In this paper, the structuring element is selected as a flat disk of radius r, because precipitation is continuous in the range-Doppler spectrogram and flat disk is better in smoothing the precipitation boundaries. The selection of radius r will be discussed in a systematic way in the following section. After the completion of Step 2, one binary mask $M^{step2} \in \{0,1\}$ is obtained.

(c) Step 3, the contiguous bins having value "1" are integrated into several separate objects.

Taking advantage of the range-Doppler continuity of precipitation, the contiguous bins of the same values "1" are grouped in areas in the range-Doppler domain which are termed as objects. These bins are termed as connected bins. The basic steps in finding the connected bins are shown in Table 4.1 (Fisher *et al.*, 2018).

Note that the unlabeled bin is a bin not yet attributed to one object. The flood-fill algorithm is universally used in the field of image processing to determine the

Table 4.1: The connected range-Doppler bins labeling algorithm.

i) Search for the next unlabeled bin p having value "1"
ii) Use a flood-fill algorithm to label bin p
iii) Repeat steps i) and ii) until all the bins are labeled.

areas connected to a given bin (i.e., a pixel). In the situation of the binary mask generation, the neighboring bins indicating "1" of a unlabeled bin "1" will be integrated together into one object. Depending on whether we consider contiguous bins touching at the corners connected or not, two options — eight-neighbors and four-neighbors can be considered. Since precipitation is continuous in the range-Doppler domain, eight-neighbors option is selected here. After objects are separated, they are sorted in area descending order going from the largest area to the smallest one, as $\mathbf{O} = [O_1, O_2, \cdots, O_N]$. Normally, precipitation is continuous in the range-Doppler spectrogram, and it has two properties: 1) large area sizes; 2) limited numbers of objects. Hence, only a limited number of separated objects that exhibit the largest areas in $\mathbf{O}$ will be chosen for processing in Step 4.

(d) Step 4, extra observable is used to produce the filtering mask.

The sorted objects in $\mathbf{O}$ will be taken one by one and further classified as precipitation or not. Inspired by the better performance of the object-orientated technique in remote sensing data analysis than the pixel-based technique (Benz *et al.*, 2004), we propose similar object-orientated precipitation and clutter separation technique. In addition to spectral polarimetric observable values, other information, such as shape, can be also used in the new filter design. Therefore, it can take full advantage of the range-Doppler continuity property of precipitation in the filter design. If the selected objects in $\mathbf{O}$ contain both precipitation and clutter, it means that they have similar spectral polarimetric observable values and area sizes. Thus, separation should be performed with extra observables to further remove the clutter. Which observables should be combined to complete the precipitation and clutter separation depends on the type of clutter and its property. For a given $O_i \in \mathbf{O}$, the filtered mask is expressed as M_{O_i}. After the extra observable filtering, the filtered separate objects are integrated as one mask expressed as

$$M^{step4} = \sum_{i=1}^{N} M_{O_i} \tag{4.12}$$

$M^{step4} \in \{0, 1\}$ is the final mask applied to the raw range-Doppler spectrogram to remove the clutter and noise, and preserve the precipitation. One scenario will be studied in detail using radar data in Section 4.3.

Table 4.2: IDRA Specifications (Figueras i Ventura, 2009). The boldface indicates parameters used for the operational mode.

Radar type	Linear FMCW
Polarization	Full polarimetric
Center frequency (GHz)	9.475
Transmitted power (W)	1, 2, 5, 10, **20**
Range resolution (m)	3, 6, 15, **30**
Sweep time (μs)	204.8, **409.6**, 8192.2, 1638.4, 3276.8
Frequency sweep (MHz)	**5**, 10, 20, 50
Antenna beamwidth (∘)	1.8
Elevation angle (∘)	0.5

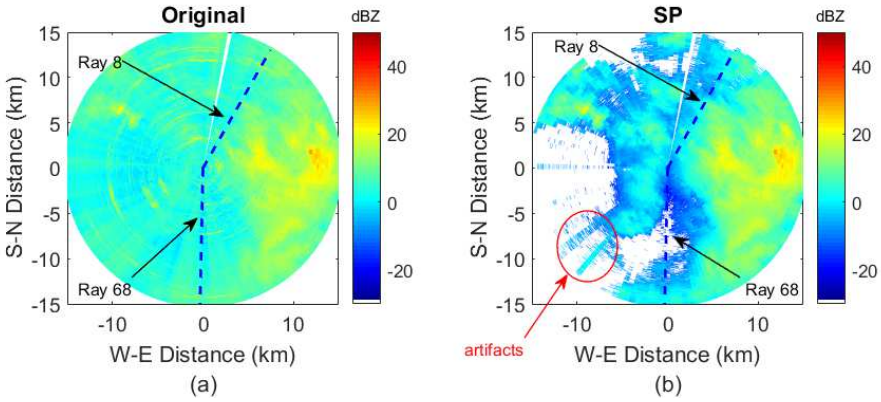

Figure 4.2: Reflectivity PPI of IDRA. Data measured at 13:00 UTC on 22nd August 2014. (a) raw Z_{hh}; (b) Z_{hh} after standard processing.

4.3. APPLICATION TO RADAR DATA

4.3.1. RADAR CLUTTER ANALYSIS

The X-band polarimetric Doppler IRCTR Drizzle Radar (IDRA) observes continuously the atmosphere (Figueras i Ventura, 2009), and it updates its measurements shown in near-real time online with a rotation rate 1 rpm. All the data collected by this horizontally scanning radar from April 2009 up to now can be accessed on the website named 4TU.centre for Research Data. However, IDRA has been affected by narrow-band moving clutter (also termed as artifacts) since its installation in 2007, which is well documented by Yin *et al.* (2017b, 2018). The specifications of the linear frequency-modulated continuous waveform (FMCW) radar are shown in Table 4.2. Note that the number of sweeps which is the terminology for FMCW radar, is equivalent to the number of pulses for pulse radar.

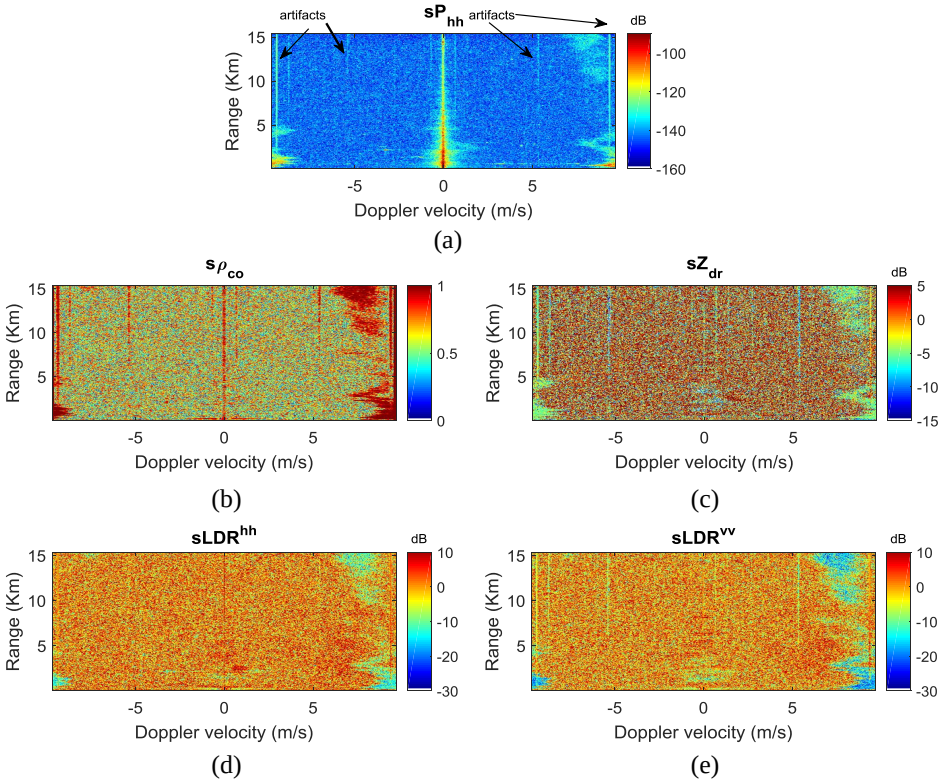

Figure 4.3: Spectral polarimetric observables of IDRA. Data are related to Ray 68 of the measurements at 13:00 UTC on 22nd August 2014. (a) spectral power sP_{hh}; (b) spectral copolar correlation coefficient $s\rho_{co}$; (c) spectral differential reflectivity sZ_{dr}; (d) spectral linear depolarization ratio $sLDR^{hh}$; (e) spectral linear depolarization ratio $sLDR^{vv}$.

The raw PPI of one radar measurement at 13:00 UTC on 22nd August 2014 is shown in Fig. 4.2(a). In addition, the PPI after the standard clutter suppression processing is shown in Fig. 4.2(b) for a comparison. The standard processing is carried out in the range-Doppler domain. It consists of a narrow notch filter centered around $0\,\mathrm{m\,s^{-1}}$ and the double spectral linear depolarization ratio filter (Unal, 2009). Further, a noise clipping technique is implemented. It keeps the Doppler bins related to a spectral reflectivity at least 3 dB above the noise level. Finally, Doppler spectra containing less than 2% of valid Doppler bins are discarded. From Fig. 4.2(b), the remaining artifacts are indicated in some azimuths. It means that the standard processing is ineffective at artifact removal. Actually, the azimuths displaying artifacts are not fixed among different PPIs from the long-term observation.

To take a close look at the raw range-Doppler spectrogram (i.e., one ray in radar PPI), Ray 68 is extracted and the spectral polarimetric observables are shown in Fig. 4.3. Averaging is not carried out to obtain sP_{hh}, sZ_{dr}, $sLDR^{hh}$ and $sLDR^{vv}$. Concerning $s\rho_{co}$,

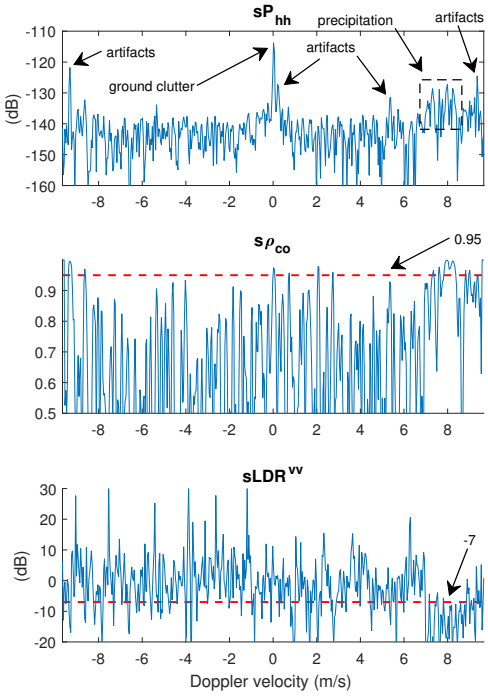

Figure 4.4: Observable spectra of Range bin 468 (e.g., 14 km) . (a) spectral power sP_{hh}; (b) spectral copolar correlation coefficient $s\rho_{co}$; (c) spectral linear depolarization ratio $sLDR^{vv}$.

there is running averaging on 7 consecutive Doppler bins. The properties of artifacts can be observed as follows: 1) non-stationary in the Doppler domain; 2) randomly appearing in some range bins; 3) parts of its intensity larger than that of weak precipitation; 4) similar spectral polarimetric features with precipitation. These features make it difficult to suppress this specific clutter for weather radar. Furthermore, Range bin 468 (e.g., 14 km) is taken and its power spectrum, $s\rho_{co}$ spectrum and $sLDR^{vv}$ spectrum are plotted as shown in Fig. 4.4. As is observed, the power intensity of ground clutter and some artifacts is higher than that of precipitation. After integrating the whole Doppler bins resulting in one reflectivity value, the true reflectivity of precipitation will be biased by the artifacts and ground clutter. Fortunately, the spectral width of artifacts and ground clutter is much narrower compared with that of precipitation, which can be used as the extra observable in Step 4 for the OBSpol filter design. Moreover, $s\rho_{co}$ values of precipitation and clutter are inseparable, which is different from that of noise. When $s\rho_{co}$ is chosen, another technique should be combined to mitigate the ground clutter. While precipitation have different $sLDR^{vv}$ values from that of clutter and noise, indicating $sLDR$ as a powerful clutter and precipitation separation observable.

As is mentioned in the introduction, the MDsLDR filter is put forward to remove the narrow-band clutter (i.e., radar artifacts and ground clutter) for full-polarimetric weather radar. Based on the difference of the spectral polarimetric feature and the spectral continuity between precipitation and clutter, the method is proved to be effective

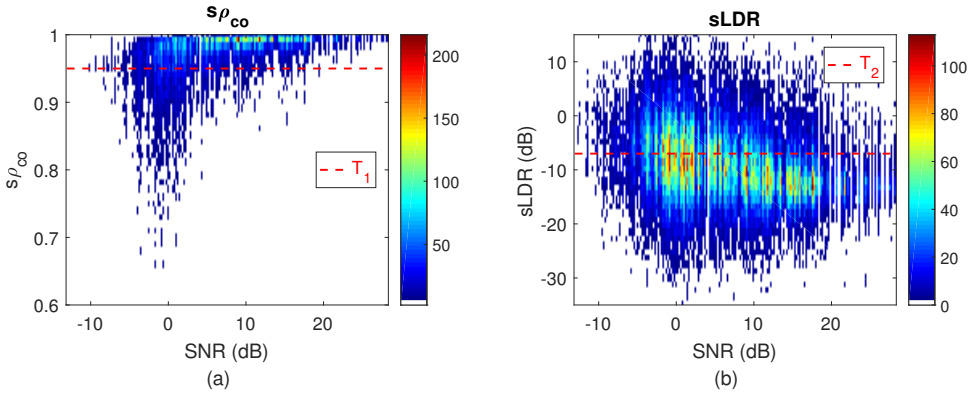

Figure 4.5: Spectral polarimetric observable distributions of precipitation versus SNR. (a) $s\rho_{co}$; (b) $sLDR^{hh}$ and $sLDR^{vv}$.

and its performance is verified by data collected in different scenarios. However, the limitation of applying the MDsLDR filter in dual-polarization weather radar which does not measure cross-polar backscattering is the spectral linear depolarization ratio ($sLDR$) measurements. The OBSpol filter proposed in this paper is used to fill the gap and the performance of the two filters will be compared and discussed in detail next.

4.3.2. PARAMETER SELECTION

Retaining the precipitation and removing the clutter is always a trade-off. In Step 1 of the OBSpol filter, for dual-polarization weather radar without cross-polar measurements, the spectral copolar correlation coefficient $s\rho_{co}$ is used as the spectral polarimetric observable for non-meteorological scatterer mitigation. Further, the notch filter around $0\,\mathrm{m\,s^{-1}}$ is used to generate the ground clutter mitigation mask M^{GCM}. Note that Doppler velocities between $-0.23\,\mathrm{m\,s^{-1}}$ and $0.23\,\mathrm{m\,s^{-1}}$ (i.e., 13 Doppler bins for IDRA operational mode with 512 sweeps for Doppler processing) are used to generate the M^{GCM}, which is based on the statistical analysis of spectral width of ground clutter. The selection of the thresholds T_1 and T_2 is based on the precipitation and clutter removal percentage (Yin *et al.*, 2017b; Unal, 2009), specifically $T_1 = 0.95$ and $T_2 = -7\,\mathrm{dB}$.

Considering Ray 8 and Ray 68 of raw PPI in Fig. 4.2(a), the true precipitation areas are manually selected, and the $s\rho_{co}$ and $sLDR$ (i.e., $sLDR^{hh}$ and $sLDR^{vv}$) value distributions versus SNR are calculated, as shown in Fig. 4.5. For each range bin, we can calculate one SNR and it corresponds to several spectral polarimetric observable values. The estimation of noise is based on the noise measurements by the radar system. From Fig. 4.5(a) and 4.5(b), it is concluded that both $s\rho_{co}$ and $sLDR$ have larger distributions with the decrease of SNR. This means that using $s\rho_{co}$ and $sLDR$ as the spectral polarimetric filtering observables in weather radar may cause some weak precipitation loss. Hence, other techniques should be included to preserve weak precipitation. In this paper, we aim to propose one technique for dual-polarization weather radar which does not measure cross-polar backscattering, so the focus is on the combination of the $s\rho_{co}$ filtering and notch filter around $0\,\mathrm{m\,s^{-1}}$.

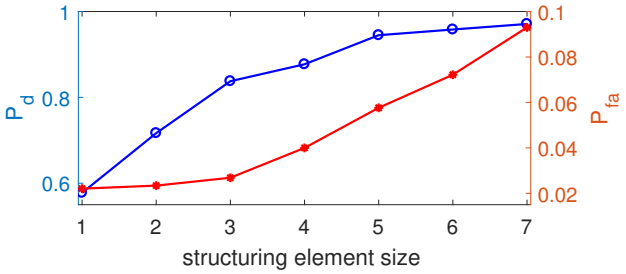

Figure 4.6: Structuring element size versus P_d and P_{fa}.

For the parameter selection next, Ray 68 of raw PPI in Fig. 4.3(a) is chosen as the study case. In Step 2, the structuring element is chosen as the flat disk of radius r which will be discussed here. Firstly, we define P_d as the detection probability of precipitation which is the ratio between the precipitation areas after Step 2 and the true precipitation areas.

$$P_d = \frac{N_s}{N_s + N_f} \tag{4.13}$$

where N_s is the number of precipitation bins successfully identified and N_f is the number of precipitation bins classified as clutter and noise. The false alarm rate (detecting the clutter and noise) P_{fa} is defined as the clutter and noise areas after Step 2 divided by the true non-precipitation ones.

$$P_{fa} = \frac{N_i}{N_T - N_s - N_f} \tag{4.14}$$

where N_T is the total bin number of the chosen spectrogram, and N_i is the number of clutter and noise bins classified as precipitation. The relations between the calculated P_d and P_{fa} and different structuring element size r are shown in Fig. 4.6. Normally, with the increase of radius r, both P_d and P_{fa} will increase, which is consistent in this figure. On one hand, when the radius r is in the interval of [1, 3], P_d increases rapidly while P_{fa} increases slowly. On the other hand, when r is in the interval of [3, 7], the situation is opposite. Thus, $r = 3$ is the turning point where the detection probability of precipitation is sufficient while keeping low false alarm rate. Based on this analysis, the structuring element size r is chosen to be 3.

Finally, in Step 4, the extra observable selected for IDRA precipitation and artifact separation is the spectral width. In general, precipitation is the distributed target with large spectral width. On the contrary, artifacts are narrow-band moving clutter with limited spectral width, specifically the largest Doppler spectral width L observed equals to 5 Doppler bins (about 20 $\mathrm{cm\,s^{-1}}$) for IDRA in the operational mode. Considering the mathematical morphology adopted in Step 2, the threshold T_3 for the spectral width selection will be

$$T_3 = L + 2 \times r \tag{4.15}$$

where r is the structuring element size determined in Step 2. Hence, we have $T_3 = 11$ (about 42 $\mathrm{cm\,s^{-1}}$). It means that for the separated objects obtained in Step 3, those

range bins related to one object whose spectral width is less than T_3 will be discarded. Therefore, dealiasing of the Doppler spectra should be carried out before this filtering technique to avoid the presence of narrow-band precipitation Doppler spectra due to Doppler aliasing. Note that the calculation of the filtered spectral width in each range bin is by summing up the binary separated objects along the Doppler domain.

The above analysis provides the parameter selection for the OBSpol filter applying to the IDRA data in the case of narrow-band clutter (both moving and stationary).

4.3.3. IMPLEMENTATION

With the set of the selected parameters, the implementation of the OBSpol filter will be given step by step according to the flowchart in Fig. 4.1. The results are the binary spectrograms, as shown in Fig. 4.7 where white color represents precipitation and the red contour represents the true precipitation obtained by manual selection. Firstly, in Step 1, the $s\rho_{co}$ filtering and the notch filter around $0\,\mathrm{m\,s^{-1}}$ are combined to generate the binary filtering mask. From Fig. 4.7(a), the range-Doppler mask after the spectral polarimetric filtering is not sufficient because of the remaining artifacts and noise. Additionally, there are some missing points inside the precipitation areas. Secondly, with the mathematical morphology in Step 2, Fig. 4.7(b) shows the recovery of the missing precipitation, but also an increase in artifacts and noise. Thirdly, the connected range-Doppler bins are integrated into several separate objects as shown in Fig. 4.7(c) - (g), where their subtitles represent the descending orders in areas, namely from the largest area to the smallest one. As is mentioned in Section 4.2, a limited number of separated objects that exhibit the largest areas will be chosen for the next process, and here only the top 5 are shown because the 5^{th} one (i.e., Fig. 4.7(g)) only contains some isolated noise. The number of separate objects chosen for next step should not be too small, otherwise it will cause precipitation loss. Neither should it be too large, otherwise it will keep extra artifacts or noise, which is not a problem because they can be removed by the extra observable filtering in Step 4 (i.e., the spectral width). For the empirical setting, we select the top 8 objects for next step processing. Note that Fig. 4.7(c) and (e) show the situations where precipitation and artifacts overlap. Finally, with the spectral width filtering, and integrating all the filtered areas in one mask as indicated by Eq. (4.12), we obtain Fig. 4.7(h) as the filtering mask on the raw range-Doppler spectrogram. There is some signal loss around 4 km, and this originates from the Doppler aliasing which separates one precipitation area into two parts. It is expected that the signal loss problem can be avoided with proper dealiasing technique (Unal and Moisseev, 2004) which will integrate the separated precipitation as a whole, and increase the spectral width. Note that the OBSpol filter cannot resolve the situation when precipitation and clutter overlap.

4.4. FILTER PERFORMANCE EVALUATION

4.4.1. SPECTROGRAM ANALYSIS

In this section, the performance of the OBSpol filter applied to IDRA measurements will be further discussed qualitatively and quantitatively comparing with one existing filter named the MDsLDR filter. The results of the MDsLDR filter and the OBSpol filter implemented on the raw range-Doppler spectrogram in Fig. 4.3(a) are shown in Fig. 4.8. From

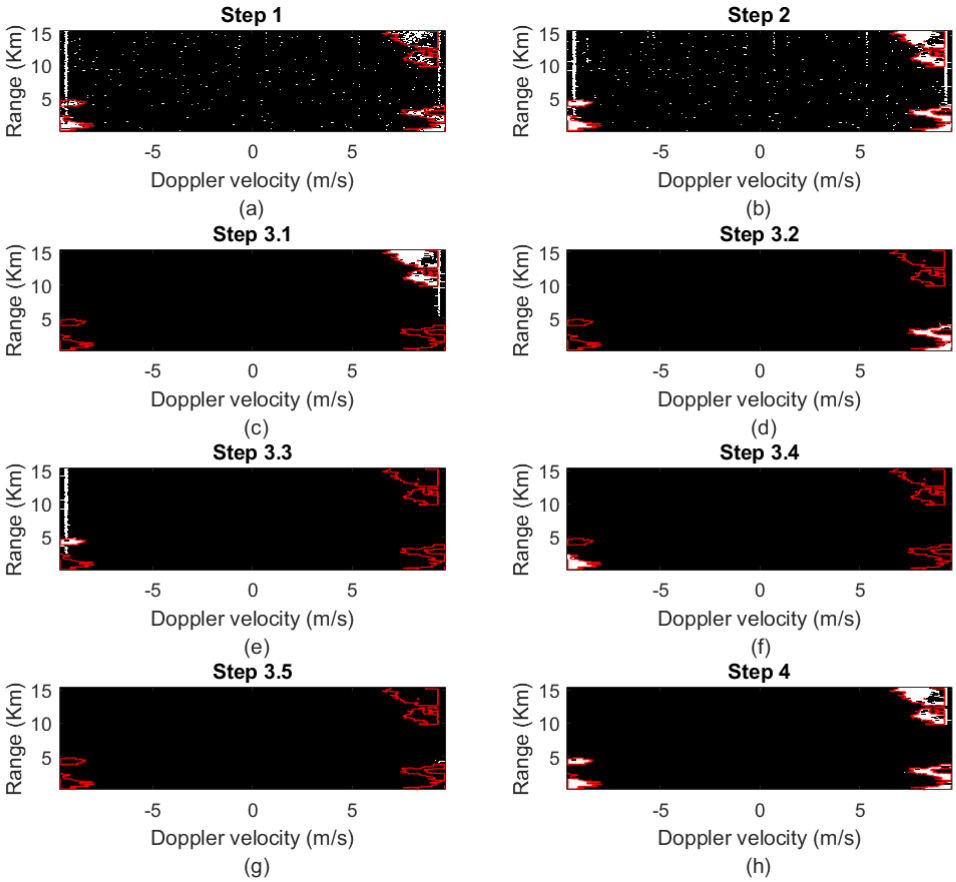

Figure 4.7: The output range-Doppler masks after each step of the flowchart. (a) Step 1; (b) Step 2; (c) - (g) Step 3; (h) Step 4.

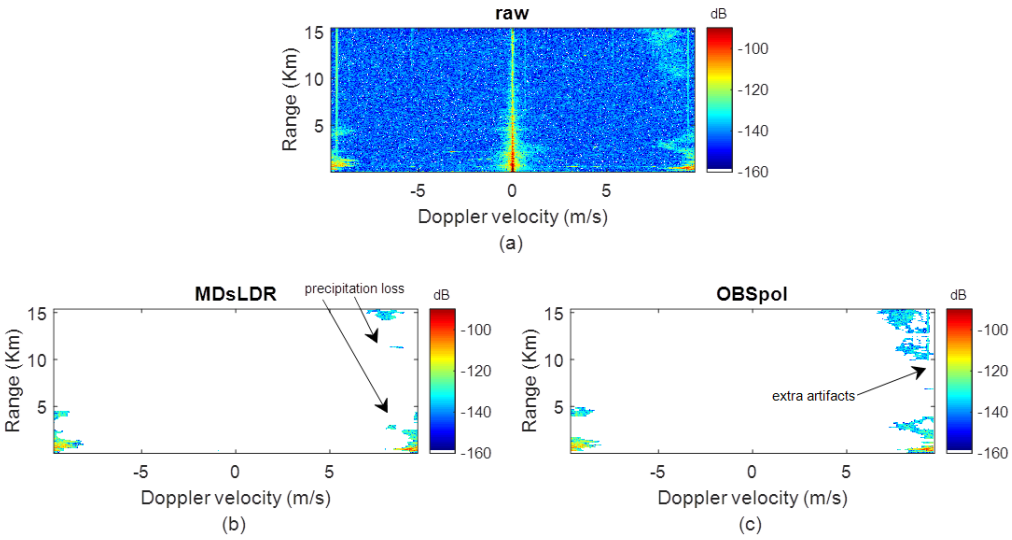

Figure 4.8: Qualitative performance comparison between the MDsLDR filter and the OBSpol filter. (a) raw spectrogram; (b) MDsLDR filtered spectrogram; (c) OBSpol filtered spectrogram.

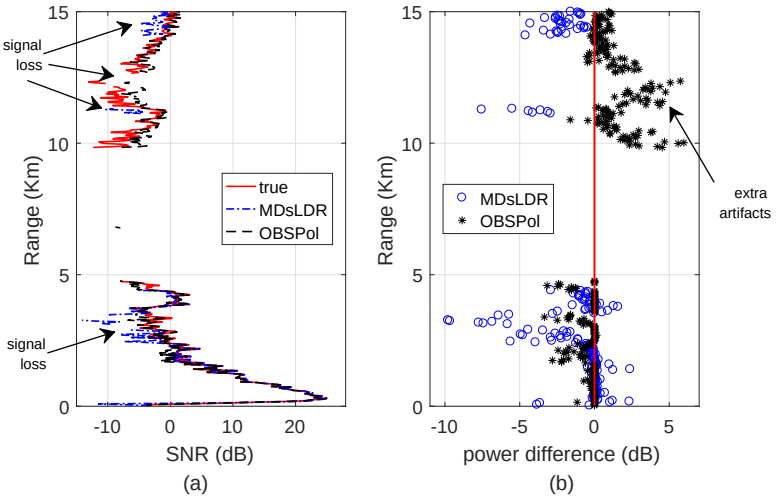

Figure 4.9: Quantitative performance comparison between the MDsLDR filter and the OBSpol filter. (a) SNR calculation in different range bins; (b) power difference after the MDsLDR filter and the OBSpol filter.

Fig. 4.8(b) and (c), it is clear that both filters can remove the artifacts, ground clutter and noise, while the OBSpol filter outperforms in keeping more weak signal. However it retains some artifacts that overlap with precipitation.

To quantify the filter performance, the SNR is calculated and shown in Fig. 4.9(a). It can be concluded that both MDsLDR filter and OBSpol filter can retain the precipitation when the SNR is larger than 2 dB. When the SNR is smaller than 2 dB, sometimes, there is some signal missing in the MDsLDR filter and there is no such problem with the OBSpol filter (see the black arrows "signal loss" in Fig. 4.9(a)). Further, the power difference between the filtered one and the true one is obtained in Fig. 4.9(b). Note that the true power is obtained by the manual selection of precipitation in the raw range-Doppler spectrogram. The maximum power difference for the OBSpol filter is around 5 dB while that of the MDsLDR filter is 10 dB. Note that such conclusion is given based on the premise that the true SNR is smaller than 0 dB which usually corresponds to light precipitation or drizzle.

Finally, the root mean square error (RMSE) is used to quantify the filtering performance. Supposing a given spectrogram, where we have R range bins with precipitation, the RMSE of a specific observable X can be expressed as

$$\delta X = \sqrt{\frac{1}{R}\sum_{r=1}^{R}\left(X^{tru}(r) - X^{est}(r)\right)^2} \tag{4.16}$$

where $X^{tru}(r)$ is the true observable value in the r^{th} range bin, which is manually selected, and $X^{est}(r)$ is the filtered observable value in the r^{th} range bin. Note that the observable X can be reflectivity Z_{hh}, radial velocity $\bar{v}$, spectral width σ_v and copolar correlation coefficient ρ_{co}. The δZ_{hh} and $\delta\rho_{co}$ of the MDsLDR filter are 2.58 dBZ and 0.063 while that of the OBSpol filter are 2.06 dBZ and 0.100 for this spectrogram (i.e., Ray 68). The RMSE difference is due to the precipitation loss in the MDsLDR filter and the artifacts preservation in the OBSpol filter, both of which are labeled in Fig. 4.8. The RMSE of the $\bar{v}$ and σ_v are not provided because the chosen spectrogram is Doppler aliased which will bring in bias. Note that the SNR interval of the chosen spectrogram is [−15 dB, 23 dB] which includes weak and moderate precipitation. To quantify further these observables, we use another data (measured at 02:00 UTC on 1st July 2011) which do not have the problem of Doppler aliasing. Continuous rays from Ray 45 to Ray 54 are considered, and the true values are manually selected. These rays are selected because clutter and precipitation do not overlap in order to estimate properly the true values of precipitation. The results are shown in Table 4.3. In addition, the SNR histogram of the chosen data is displayed in Fig. 4.10. Distributed in the interval of [−15 dB, 43 dB], the selected data contain weak, moderate and strong precipitation. In general, both the OBSpol filter and the MDsLDR filter have good performance, specifically the average δZ_{hh} is within 1.00 dBZ, the average $\delta\bar{v}$ within 0.15 m/s, the average $\delta\sigma_v$ within 0.50 m/s and the average $\delta\rho_{co}$ within 0.020. The OBSpol filter outperforms the MDsLDR filter in all the observables when clutter and precipitation do not overlap and Doppler dealiasing had been performed. It means that the OBSpol filter has better performance in weak precipitation preservation.

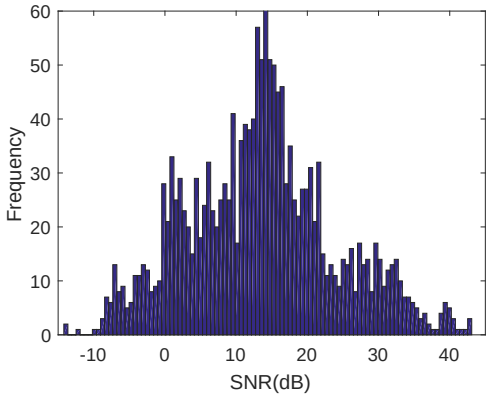

Figure 4.10: SNR histogram of the chosen data for RMSE evaluation.

Table 4.3: RMSE of radar observables.

Ray No.	MDsLDR				OBSpol			
	δZ_{hh}	$\delta \bar{v}$	$\delta \sigma_v$	$\delta \rho_{co}$	δZ_{hh}	$\delta \bar{v}$	$\delta \sigma_v$	$\delta \rho_{co}$
45	1.60	0.05	0.07	0.017	0.49	0.06	0.05	0.013
46	1.05	0.75	0.82	0.037	0.43	0.55	0.74	0.023
47	0.83	0.05	0.09	0.003	0.19	0.01	0.08	0.002
48	1.43	0.13	0.20	0.012	0.05	0.02	0.03	0.003
49	1.57	0.15	0.16	0.018	0.08	0.02	0.02	0.005
50	0.17	0.04	0.14	0.002	0.03	0.06	0.21	0.002
51	1.30	0.05	0.07	0.061	0.59	0.02	0.03	0.015
52	0.29	0.04	0.04	0.005	0.24	0.02	0.02	0.011
53	0.63	0.07	0.04	0.005	0.05	0.02	0.02	0.004
54	0.93	0.15	0.49	0.010	0.57	0.11	0.42	0.019
average	1.00	0.15	0.45	0.017	0.27	0.09	0.16	0.010

4.4.2. PPI ANALYSIS

For operational weather radar systems, the filtered observables are required to display in real-time in the radar PPI. To test the real-time capability of the proposed technique, both the MDsLDR filter and the OBSpol filter are applied to the data collected at 13:00 UTC on 22nd August 2014, and their results are given in Fig. 4.11. Compared with the PPI after the standard processing shown in Fig. 4.2(b), both the MDsLDR filter (i.e., Fig. 4.11(a)) and the OBSpol filter (i.e., Fig. 4.11(b)) have better performance in artifact removal, while the OBSpol filtered PPI performs better in weak precipitation preservation. One example is the Ray 68 (i.e., Fig. 4.8) which corresponds to the spectrogram analyzed above. It is not easy to obtain the true precipitation for the selected data, and the ray-by-ray output check is done to further verify the better performance of the OBSpol filter in keeping weak precipitation signal. All the following cases are met: precipitation with narrow-band clutter and precipitation with ground clutter. Note that the implementation of the MDsLDR filter and the OBSpol filter takes 18.2 s and 28.1 s for the whole PPI

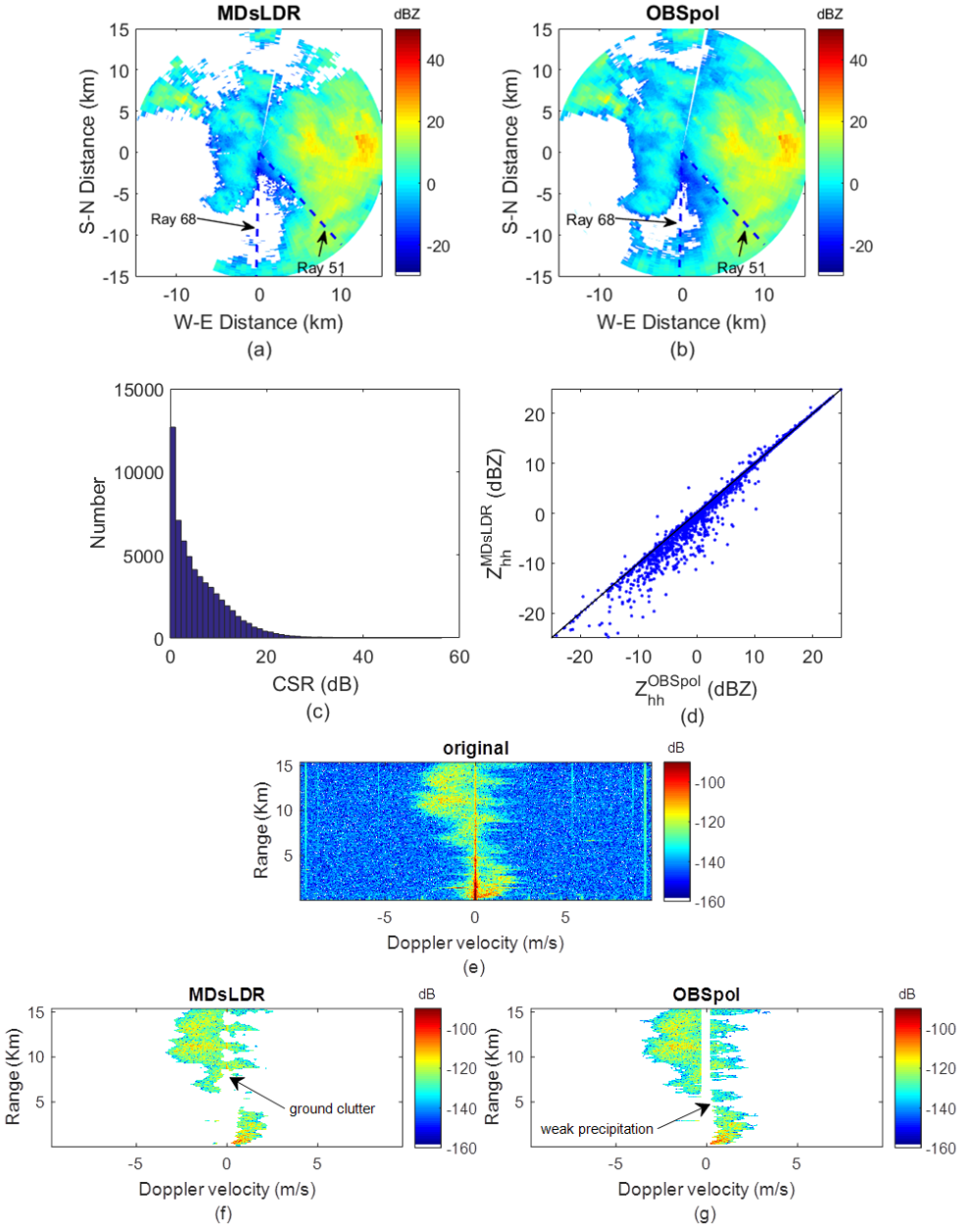

Figure 4.11: Performance comparison between the MDsLDR filter and the OBSpol filter. Data measured at 13:00 UTC on 22nd August 2014. (a) Z_{hh} after the MDsLDR filter; (b) Z_{hh} after the OBSpol filter; (c) clutter suppression ratio distribution of the OBSpol filter; (d) scatter plot of the MDsLDR filtered Z_{hh} and the OBSpol filtered Z_{hh}; (e) raw spectrogram of Ray 51; (f) MDsLDR filtered spectrogram; (g) OBSpol filtered spectrogram.

using Matlab 2016b in a Window 7 desktop PC with a 3.6 GHz Intel Xeon E5-1620 CPU and 16 GB RAM in this case. Hence, both algorithms can be implemented in real-time.

To further quantify the filtering performance of the OBSpol filter in the PPI, the clutter suppression ratio (CSR) is calculated and plotted in Fig. 4.11(c). In principle, CSR is the filtered reflectivity subtracted from the raw one. The maximum clutter suppression ratio is 54.7 dB for the case occurred at 13:00 UTC on 22nd August 2014. Furthermore, the scatter plot of the MDsLDR filtered reflectivity Z_{hh}^{MDsLDR} and the OBSpol filtered reflectivity Z_{hh}^{OBSpol} is shown in Fig. 4.11(d). Most of the time, when the reflectivity is less than 10 dBZ, Z_{hh}^{OBSpol} is larger than Z_{hh}^{MDsLDR}. This is because the OBSpol filter has better ability in retaining weak precipitation. As for the unexpected cases where Z_{hh}^{OBSpol} is smaller than Z_{hh}^{MDsLDR}, the main reason is the presence of residual ground clutter after the MDsLDR filtering, which is illustrated by Ray 51 in Fig. 4.11(e)-(g), respectively. Note that both techniques cannot resolve the problem when precipitation and clutter overlap. In that case when precipitation data are discarded by filtering like at $0\,\mathrm{m\,s^{-1}}$ for Ray 51, the radar observables are presently estimated without interpolation procedure in the spectrogram.

4.4.3. OTHER CASE STUDY

To further assess the performance of the OBSpol filter, a case with severe artifacts is considered. The case occurred at 12:00 UTC on 15th January 2016. The raw PPI and the one after the standard processing are shown in Fig. 4.12(a)-(b). It can be observed that the influence of artifacts on radar PPI are severe and artifacts cannot be removed by the standard processing. The PPI of Z_{hh} after the MDsLDR filter and the OBSpol filter are shown in Fig. 4.12(c)-(d). From these figures, it can be concluded that both the OBSpol filter and the MDsLDR filter can mitigate artifacts while the OBSpol filter can preserve more weak precipitation. Just based on the PPI of Z_{hh}, it is difficult to determine whether the added signal is precipitation or not. Hence, the ray-by-ray inspection has been implemented. Here Ray 70 is used as an example, and its raw, MDsLDR filtered and OBSpol filtered spectrograms are presented in Fig. 4.12(e)-(g) respectively.

From Fig. 4.12(e), it is obvious that the measurement is severely contaminated by narrow-band moving artifacts. Both the MDsLDR filter and the OBSpol filter can remove the non-stationary artifacts, the noise and the ground clutter, and they can keep the precipitation having moderate SNR. However, less weak precipitation is preserved after the MDsLDR filtering, while the OBSpol filter can keep the weak precipitation locating on the edge of the precipitation area. This is confirmed by the scatter plot of the MDsLDR filtered Z_{hh} and the OBSpol filtered Z_{hh} in Fig. 4.12(h). Finally, the histogram of the CSR of the OBSpol filter is shown in Fig. 4.12(i). Note that the maximum clutter suppression ratio, in this case, is 58.3 dB.

4.4.4. IMPACT OF DOPPLER VELOCITY RESOLUTION

The operational weather radars tend to have shorter dwell time due to the requirement of faster updating atmospheric changes. This tendency means that the proposed clutter mitigation technique should also work with smaller pulse numbers. This section will further verify the effectiveness of the OBSpol filter regarding different Doppler velocity

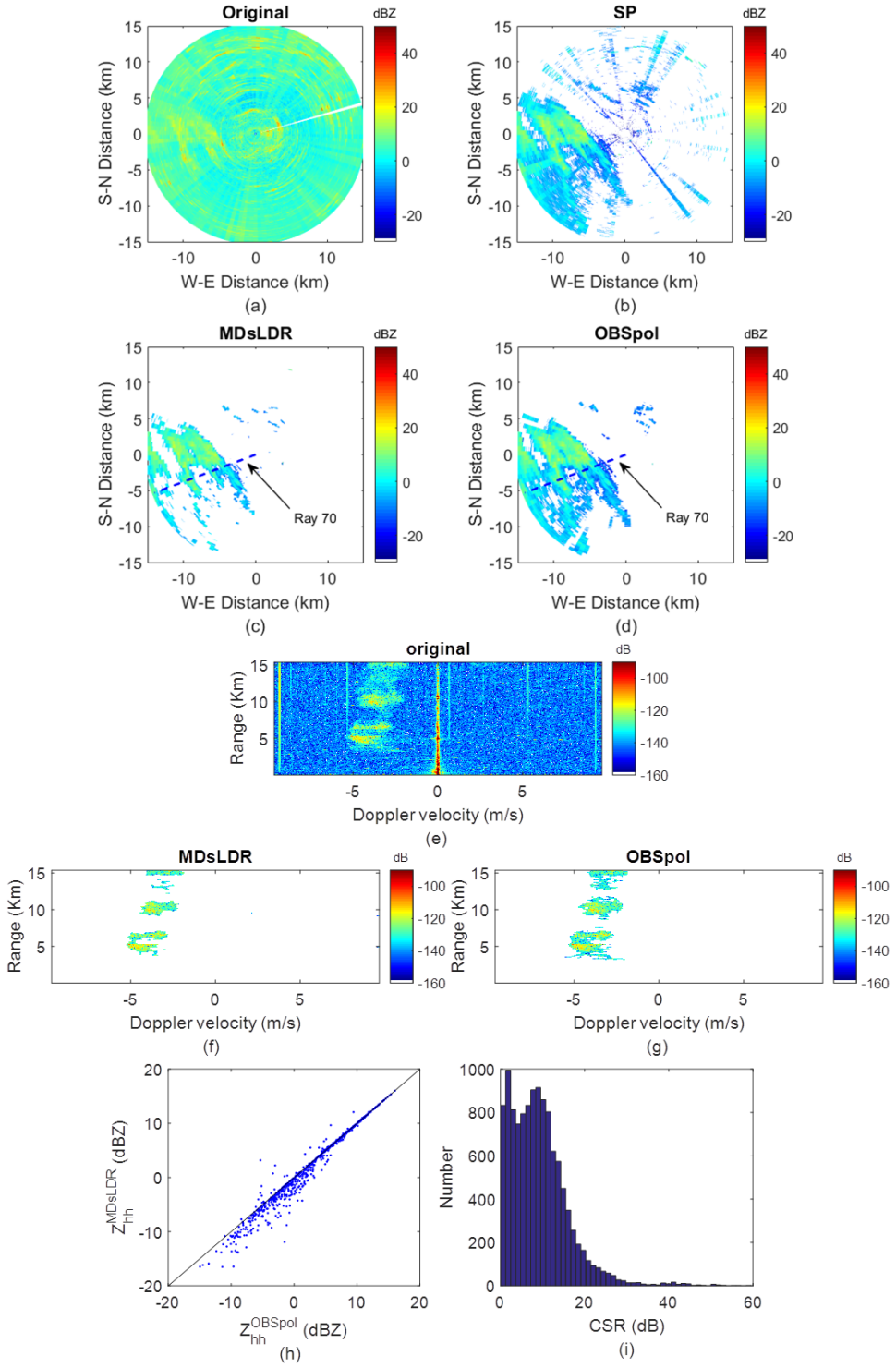

Figure 4.12: Performance comparison between the MDsLDR filter and the OBSpol filter. Data measured at 12:00 UTC on 15th January 2016. (a) raw Z_{hh}; (b) Z_{hh} after standard processing; (c) Z_{hh} after MDsLDR filter; (d) Z_{hh} after OBSpol filter; (e) raw spectrogram of Ray 70; (f) MDsLDR filtered spectrogram; (g) OBSpol filtered spectrogram; (h) scatter plot of MDsLDR filtered Z_{hh} and OBSpol filtered Z_{hh}; (i) clutter suppression ratio distribution of the OBSpol filter.

resolutions.

Since the total sweep number of one IDRA PPI N_{PPI} is fixed, and it meets

$$N_{PPI} = N_{Ray} \times N_{Doppler} \tag{4.17}$$

where N_{Ray} is total ray number in the PPI and $N_{Doppler}$ is the sweep number chosen for Doppler processing. To get the same data for comparison, the increasing multiple of the ray number is the same as the decreasing multiple of sweep number for Doppler processing in the data selection.

Using the same data measured at 13:00 UTC on 22nd August 2014 which is obtained in the operational mode (i.e., pulse repetition frequency (PRF) around 2.4 kHz), we set the sweep number $N_{Doppler}$ to 512, 256, 128 and 64 for the Doppler processing to explore the OBSpol filter performance. Ray 68, Ray 136, Ray 272 and Ray 544 are considered for the parameter selection which obeys the same principle of Section 4.3.2, as shown in Table 4.4. Note that the selection of L is obtained by the observation of the spectral width of the narrow-band moving clutter. While the decrease of T_1 is due to the smaller sweep number selected for Doppler processing which means the spectral SNR is decreasing, leading to the decrease of the spectral copolar correlation coefficient.

Table 4.4: Parameter selection for different Doppler velocity resolutions.

Sweep number	Velocity resolution	averaging size	Ray No	L	T_1	r	T_3
512	3.8×10^{-2} (m/s)	7	68	5	0.95	3	11
256	7.5×10^{-2} (m/s)	5	136	4	0.94	3	10
128	1.5×10^{-1} (m/s)	5	272	3	0.91	2	7
64	3.0×10^{-1} (m/s)	5	544	1	0.90	2	5

With the parameter selection in Table 4.4, another ray than the study case Ray 68 is evaluated and the spectrogram results of Ray 62, Ray 124, Ray 248, and Ray 496 related to different Doppler velocity resolutions are shown in Fig. 4.13(a) - (d), respectively. In addition, the filtered PPIs with sweep number 128 and 64 are shown in Fig. 4.13(e) and (f). From these results, we can conclude that with the decrease of Doppler velocity resolution, the performance of keeping weak precipitation also degrades. The reason is that the OBSpol filter, taking advantage of range-Doppler continuity of precipitation, will perform better with more data in the range-Doppler spectrogram. However, qualitatively acceptable results in preserving the precipitation and removing narrow-band clutter (both moving and stationary) and noise can still be obtained in all the situations. This shows the potential that the OBSpol filter can be used for different Doppler velocity resolutions.

4.5. CONCLUSION

Aiming at removing both stationary and moving clutter and retaining precipitation for dual-polarization weather radar which does not measure cross-polar backscattering, this paper puts forward a new clutter suppression method named the object-orientated spectral polarimetric (OBSpol) filter. Taking advantage of the spectral polarimetric feature and the range-Doppler continuity of precipitation, the OBSpol filter is implemented

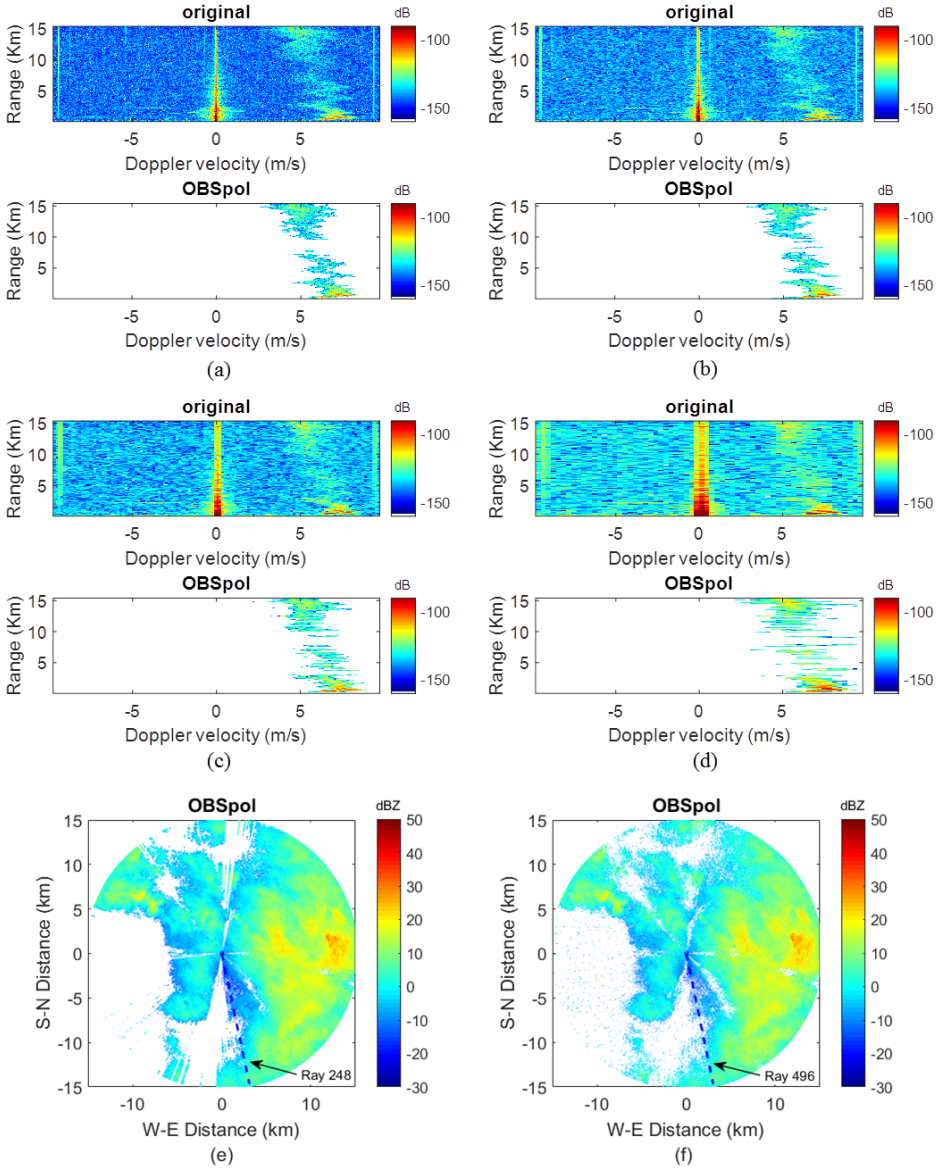

Figure 4.13: OBSpol filter applied to radar data with different Doppler velocity resolutions. Data measured at 13:00 UTC on 22nd August 2016. (a) Spectrogram with sweep number 512; (b) Spectrogram with sweep number 256; (c) Spectrogram with sweep number 128; (d) Spectrogram with sweep number 64; (e) PPI with sweep number 128; (f) PPI with sweep number 64.

in the range-Doppler spectrogram to mitigate the clutter and noise. The filter is divided into 4 steps. Firstly, the spectral polarimetric observables are utilized to generate one binary mask where "1" indicates the precipitation. In Step 2, the mathematical morphology method is used to recover the missing precipitation areas of the obtained mask. Based on the reconstructed mask in Step 2, the contiguous bins having values "1" are selected and integrated into several separate objects in Step 3. Next in Step 4, whether the produced objects are precipitation or not will be further decided based on appropriate observable. Thus, a filtering mask can be obtained by summing up the filtered separated objects, which is implemented on the raw range-Doppler spectrogram to keep the precipitation and remove the clutter and noise.

The OBSpol filter can be very general due to different spectral polarimetric filtering strategies in Step 1 and different observable selection in Step 4, which depend on the type of clutter encountered and based on the clutter feature study. The OBSpol filter is a spectrogram-by-spectrogram clutter mitigation technique which integrates clutter detection and filtering together. In this paper, the OBSpol filter is specifically designed for narrow-band clutter (both stationary and moving) mitigation in the polarimetric Doppler radar IDRA. In the situation of IDRA which simulates dual-polarization radar without cross-polar measurements, the spectral copolar correlation coefficient filtering and the notch filter around $0\,\mathrm{m\,s^{-1}}$ are combined in Step 1, and the extra observable in Step 4 is the spectral width. The OBSpol filter can remove the ground clutter, the noise and the moving artifacts, which are not overlapping with precipitation. In the cases where clutter mixes with precipitation, other techniques should be combined. Compared with one existing method namely the moving double spectral linear depolarization ratio (MDsLDR) filter, both filters can remove narrow-band clutter (i.e., ground clutter and moving artifacts) and noise, and they tend to have the same performance in keeping precipitation with a reflectivity larger than 10 dBZ, while OBSpol filter is better in weak precipitation preservation due to the more advanced signal processing technique adopted in the filter design. Two precipitation cases — 1) moderate precipitation with large scale and 2) light precipitation with severe artifact contamination — are used to assess the performance and make the comparison.

There are several advantages of the OBSpol filter. Apart from the good performance in clutter mitigation and precipitation preservation, this technique is easy to implement, and it has relatively low computation complexity. In addition, the spectral polarimetric features can be the observables of dual-polarization weather radar without cross-polar measurements. Last but not least, the OBSpol filter can be used with different Doppler velocity resolutions. Hence, the OBSpol filter can be applied in real-time for dual-polarization operational weather radar. It is foreseeable that the OBSpol filter can be extended to remove different types of weather radar clutter with proper observable selection. However, the OBSpol filter cannot resolve the problem when precipitation is mixed with clutter. It is expected that in absence of moving clutter when precipitation overlaps with ground clutter, the GMAP or CLEAN-AP will perform better than the OBSpol filter. More research can be done in these directions in the future.

5

RADIO FREQUENCY INTERFERENCE CHARACTERIZATION AND MITIGATION FOR POLARIMETRIC WEATHER RADAR

This chapter has been submitted as:

Jiapeng Yin, Peter Hoogeboom, Christine Unal, Herman Russchenberg. "Radio Frequency Interference Characterization and Mitigation for Polarimetric Weather Radar.", *IEEE Trans. Geosci. Remote Sens.*, Under review.

Chapter 3 and Chapter 4 describe the real-time clutter mitigation techniques which are specifically designed for narrow-band clutter removal for polarimetric weather radar. This chapter extends the application of the mentioned clutter mitigation techniques to the radio frequency interference (RFI) mitigation. Observed in the spectral domain, RFI are broad-band clutter, acting as additional noise over the whole spectra. In this chapter, RFI mitigation techniques for polarimetric weather radar with and without cross-polar measurements are presented.

Except the introduction is given in Section 5.1, the reminder of this chapter is organized as follows. In Section 5.2, RFI characterization is given, consisting of RFI-contaminated weather radar, RFI characterization in single polarization radar and RFI characterization in polarimetric radar. The RFI simulation in radar is introduced in Section 5.3. Section 5.4 introduces the spectral polarimetric filters. The filter applications in RFI mitigation in both radar with simultaneous transmission of horizontally and vertically polarized

waves (SHV radar) and radar with alternate transmission of horizontally and vertically polarized waves (AHV radar) are provided in Section 5.5. Finally, Section 5.6 draws conclusions and discusses guidelines for using these filters.

5.1. INTRODUCTION

Polarimetric Doppler weather radar is well recognized as an effective sensor for obtaining the microphysical and dynamical properties of precipitation at high spatial and temporal resolution (Bringi and Chandrasekar, 2001). The prerequisite of using weather radar data is sufficient measurement accuracy and precision. The primary error sources are different types of unwanted echoes termed as clutter. The presence of various clutter may prevent detection of weather signal or introduce bias on radar observables. Hence, it is important to design a multi-functional filter to mitigate all the clutter.

Nowadays, heavy demands for bandwidth in the radio frequency (RF) spectrum force its shared use. There is a growing concern on the effects of unwanted RF signals in weather radars (Cho, 2017). For example, band 5470 - 5720 MHz was assigned to the mobile service for the operation of wireless access systems, including radio local area networks (RLAN) at the World Radio-communication Conference 2003 (ITU-R Resolution 229, 2003). The allocated bands partially overlap with the bands used by existing C-band radars, which may introduce some radio frequency interference (RFI).

The co-existence of weather radar with RLAN requires the Dynamic Frequency Selection (DFS) equipment in RLAN systems to detect radar signals. Before using a channel, a check for the presence of radar signals for a time period initially set to 60 s is carried out by the DFS, and the decision should be made in RLAN to avoid the frequencies in use by radars. However, some DFS only consider "simple" radar characteristics, such as pulse widths over 1 μs and a fixed pulse repetition interval (Tristant, 2009). This makes DFS incapable of avoiding RFI in radar systems.

In the past 15 years, the reported RFI contamination issues on C-band weather radars have been increasing. Typical examples are the Terminal Doppler Weather Radar (TDWR) (Carroll *et al.*, 2010) and the European National Meteorological Services Network (EUMETNET) (Saltikoff *et al.*, 2016). Moreover, there is an increasing number of cases from S-band radars (e.g., the National Weather Service Weather Radar termed as NEXRAD), which are caused by adjacent band interference from wireless networks and in-band interference from other government radars (Saltikoff *et al.*, 2016).

Hence, the detection and mitigation of RFI at the radar signal processing level is in high demand. The signatures of RFI on radar plan position indicator (PPI) are dots, spokes, or stripes (Saltikoff *et al.*, 2016), which contaminate large portions of a weather radar scanning volume. By comparing the amplitude of each pulse to that of its immediate neighbors or the median over the dwell time, the 1D median RFI filter (Lake *et al.*, 2014) and Vaisala-3 RFI filter (Vaisala, 2016) were proposed. However, the RFI cannot be completely removed by these two filters. Based on the amplitude-anomaly property of RFI in the range-time domain, a 2D RFI filter was designed (Cho, 2017), which shows better performance in RFI removal compared with the aforementioned methods.

However, these time domain methods are especially suitable for low to medium duty cycle interference (less than 10% (Cho, 2017)). When the duty cycle of the interferer surpasses 50%, which means that in the time domain not enough clean data are left for

data processing, Doppler spectral filtering is recommended (Cho, 2017). In addition, due to its pulsed nature in the time domain, RFI could perhaps be largely removed in the time domain for a pulse radar. However, this is not the case for a frequency-modulated continuous wave (FMCW) radar, which is attractive for its cost efficiency, low power for transmission and higher range resolution(Richards *et al.*, 2010). In FMCW radar, the time domain echoes from all ranges are received simultaneously and are superimposed, making the RFI unidentifiable. The raw time domain FMCW data are Fourier transformed to the range domain, after which the RFI appears as white noise. Moreover, the removal in the time domain has, for a case of weak signals and strong interference, the risk of removing or reducing the atmospheric signal.

To cope with these problems of the time domain method, filters in the Doppler domain can be considered. In the Doppler domain, RF interference in weather radars presents as raised white noise (Joe *et al.*, 2005). If the weather signal is not completely covered by the raised noise floor, the weather observables can be recovered. A spectral polarimetric filter based on a fuzzy-logic classification algorithm was proposed (Rojas *et al.*, 2012), but its performance in RFI mitigation was not fully discussed.

To mitigate the radio frequency signatures and alleviate the problem of high duty cycle RFI in both pulse and FMCW polarimetric weather radar, spectral polarimetric filters (SPFs) are investigated in this paper. These SPFs, consisting of the moving double spectral depolarization ratio (MDsLDR) filter (Yin *et al.*, 2017b) and the object-orientated spectral polarimetric (OBSpol) filter (Yin *et al.*, 2019), are multi-functional filters which can simultaneously remove various types of clutter. Specifically, they were initially put forward to mitigate narrow-band clutter (i.e., moving clutter and ground clutter) and now are analyzed for removing the RFI. Taking advantage of the spectral polarimetric features and range-Doppler continuity of precipitation, the filters are implemented in the range-Doppler spectrogram (i.e., one ray in radar PPI) to mitigate the clutter. The filters will generate a filtering mask that is applied to the raw range-Doppler spectrogram to retain the precipitation and remove the clutter. The filters can be used in polarimetric weather radar with and without cross-polar backscattering measurements.

Currently, data from the following radar systems are available to us: 1) a C-band pulse Doppler radar contaminated by RFI without cross-polar measurements; 2) an X-band FMCW radar with cross-polar measurement capability, but not influenced by RFI. Based on the limited data, we first characterize the features of the RFI in the spectral domain using the real radar measurements, and then use the obtained spectral features to simulate the situation where the full-polarimetric radar is contaminated by RFI to further compare different types of spectral polarimetric filters.

5.2. RFI CHARACTERIZATION

5.2.1. RFI-CONTAMINATED WEATHER RADAR

Characterization of RFI is required to optimize the mitigating filtering procedures. In this paper RFI simulation is used, based on the properties of real RFI signals. The latter are taken from the weather radar systems of the Royal Netherlands Meteorological Institute (referred to as KNMI, taken from the Dutch abbreviation). From May 12th 2017, KNMI operates new weather radar systems, upgrading from single-polarization (i.e., Se-

lex Meteor 360) to dual-polarization (i.e., Selex Meteor 735CDP10 (KNM, 2018a)). The two new radars located at Herwijnen and Den Helder can cover the whole Netherlands. The radars are also part of the EUMETNET (Huuskonen *et al.*, 2014). The KNMI radars have 16 scanning modes with different configurations in 5 minutes observation interval. A precipitation map is compiled for the public and for weather forecast (Pre, 2018). In addition, all the processed radar data are freely accessible online (KNM, 2018b). The specifications of the KNMI radars are shown in Table 5.1.

Table 5.1: KNMI radar Specifications (KNM, 2018a).

Radar type	Pulsed Doppler
Transmitter type	Magnetron
Polarization	Dual-polarization
Center frequency (GHz)	5.633(Herwijnen), 5.625(Den Helder)
Transmitted power (kW)	500
Pulse width (μs)	0.5 - 3.5
Pulse repetition frequency (Hz)	175 - 2400
Antenna beamwidth	$\leq 1°$
Operational angles	Elevation $-2°$ - $90°$, Azimuth $0°$ - $360°$
Scanning strategy	16 modes in 5 minutes

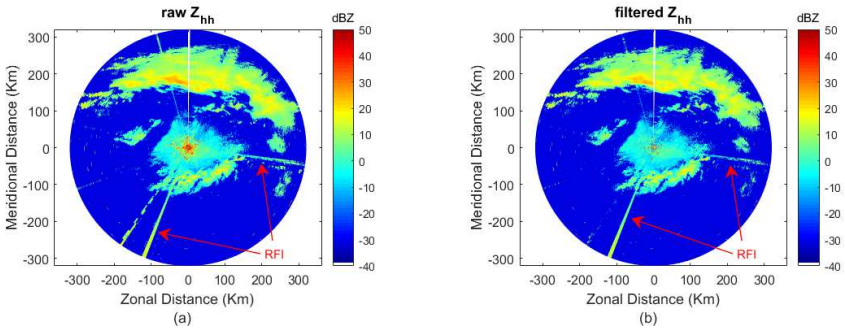

Figure 5.1: Processed data of KNMI Herwijnen radar. (a) raw reflectivity Z_{hh} PPI; (b) filtered reflectivity Z_{hh} PPI.

RFI contamination is present in processed data of the KNMI radar collected at 17:15 UTC on October 26th 2017. We display the raw reflectivity PPI and the one after the standard processing in Fig. 5.1. The PPIs in Fig. 5.1, shows that RFI are spikes along the whole range in some azimuth directions. The standard processing of KNMI radar consists of an IIR, DFT linear or Gaussian iterative interpolation (Sel, 2018), which are incapable of RFI signature mitigation. Hence, it is imperative to find a solution which can be implemented in real-time to mitigate the RFI.

First it will be shown that the RFI in Doppler spectra of this radar strongly resembles

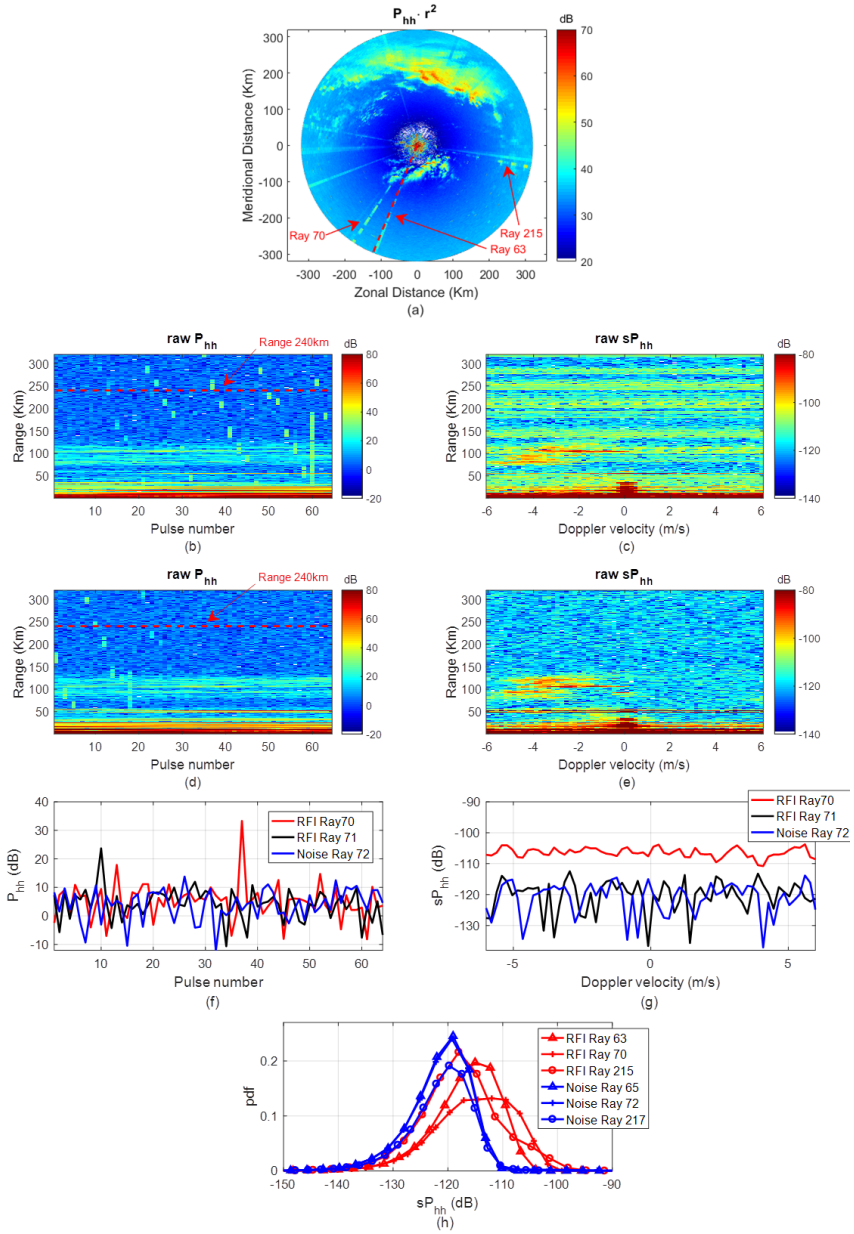

Figure 5.2: KNMI Herwijnen radar measurements. (a) raw uncalibrated PPI of $P_{hh} \cdot r^2$; (b) range-time image of Ray 70; (c) range-Doppler spectrogram of Ray 70; (d) range-time image of Ray 71; (e) range-Doppler spectrogram of Ray 71; (f) backscattered power versus pulse number of RFI and noise at Range 240 km; (g) power spectra versus Doppler velocity of RFI and noise at Range 240 km; (h) observed probability density function of spectral power of RFI and noise.

white noise as it was also concluded in e.g. Joe *et al.* (2005). Next, in the analysis of RFI filters for various types of polarization radars, similar white noise signals will be injected to study the filtering merits in a controlled fashion.

5.2.2. RFI CHARACTERIZATION IN SINGLE POLARIZATION RADAR

To further analyze the features of the RFI, some I/Q data were recorded. Data collected at 17:17 UTC on October 26th 2017 are shown in Fig. 5.2. The data were measured in the same configuration as the PPI in Fig. 5.1, namely the antenna speed is 2 rpm, the elevation angle is 0.3°, the pulse repetition frequency is 449 Hz, and the range resolution is 0.4 km. As observed in Fig. 5.2(a), there is more RFI appearing in the radar PPI and some of it overlaps with the precipitation. The RFI pulses are not synchronised with the radar timing, therefore they occur randomly with approximately equal signal strength at all radar ranges, whereas the strength of atmospheric signals is range dependent.

For the Doppler processing, the number of pulses in the Fourier transform window is set to be 64, which corresponds to a Doppler velocity resolution of 18.8 cm s^{-1}, and an azimuth resolution of 1.6°. A Hamming window is applied to suppress spectral leakage. Ray 70 is considered as an example of the RFI contamination. Fig. 5.2(b) shows the backscattered power versus range and pulse number (i.e., time). Irregularly positioned short spikes can be observed. A range-Doppler spectrogram is obtained (Fig. 5.2(c)) when the Fourier transform is applied on the received signal along the time domain (i.e., the pulses) for each range. We can see that the precipitation is heavily masked by the interference. A single RFI spike in the time domain introduces a wide noise-like response in the Doppler domain, just as may be expected in theory from the Fourier transform of a Dirac pulse. In addition, Ray 71 is inspected, and its range-time image and range-Doppler spectrogram are shown in Fig. 5.2(d) and (e). The first 20 pulses of the range-time image of Ray 71 have spikes similar to that of Ray 70, while the rest has no spikes, and is therefore free of RFI contamination.

Fig. 5.2(f) and Fig. 5.2(g) show the time domain and the Doppler spectrum for a single range bin at 240 km. Rays 70, 71and 72 are displayed. The strong spike in the time domain of Ray 70 leads to a high level of interference in the spectral domain, thereby masking the thermal noise, whereas Ray 72, which contains no RFI shows the thermal noise only. Clearly in the spectral domain the RFI signal is noise-like, albeit that the variance is much smaller than the one for noise. Still, the bandwidth of RFI signals is much wider than the bandwidth of weather radars, and thereby it contributes to the noisy character of RFI as experienced in weather radar Doppler spectra.

Next, the distribution of the (non-precipitating) background signal level is estimated in Fig. 5.2(h) for a variety of rays. All the spectral bins in the range interval between 140 km and 320 km are taken to generate the probability density function (pdf) of spectral power. The chosen bins cover RFI with a wide range of interference to noise ratio (INR), including noise only bins. Ray 65, 72 and 217 are completely free of RFI contamination. All of these pdfs have a near-Gaussian shape, which supports the assumption of the noisy character of RFI, even though the power distribution for a single event as indicated in Fig. 5.2(g), does not fully comply with a white noise distribution.

The INR parameter is introduced here to enable realistic and comparable interference levels in simulations with various radar systems later on in this paper. This allows

for a better comparison of the RFI filter performance for these systems. Ray 70 has the largest INR, followed by Ray 63, then Ray 215, which is consistent with the PPI in Fig. 5.2(a). A maximum INR of about 16 dB is observed.

In conclusion, the above observations support the validity of RFI simulation with white noise in the spectral domain, as was also concluded in Cho (2017).

5.2.3. RFI CHARACTERIZATION IN POLARIMETRIC RADAR

POLARIMETRIC RADAR TYPES AND RFI

Most polarimetric radars have separate receive channels for horizontal and vertical polarization. The RFI analysis for a single channel in the previous section is equally valid for these polarimetric radars. An RFI signal, that is transmitted with an arbitrary linear polarization (not strictly H or V), will be decomposed by the receive channels into a horizontal and a vertical component. In general, these components will have different amplitudes (except for a 45° polarization transmitted RFI pulse), but show a strong correlation. The received signals in the polarimetric radar are linked to the polarization of the transmitted pulse, resulting in a 2×2 complex scattering matrix S

$$S = \begin{bmatrix} S_{hh} & S_{hv} \\ S_{vh} & S_{vv} \end{bmatrix} \tag{5.1}$$

where S_{xy} is a complex scattering matrix component with a transmitted y polarization and a received x polarization, x and y being horizontal polarization (i.e., h) or vertical polarization (i.e., v). In the case of backscattering in a reciprocal medium (e.g., precipitation), $S_{hv} = S_{vh}$.

A distinction has to be made, based on the transmit pulse sequences. Polarimetric radars can be divided into two types: 1) simultaneous transmission of horizontally and vertically polarized waves (SHV mode) and 2) alternate transmission of horizontally and vertically polarized waves (AHV mode). The schematic diagram is displayed in Fig. 5.3 (Melnikov and Zrnić, 2015).

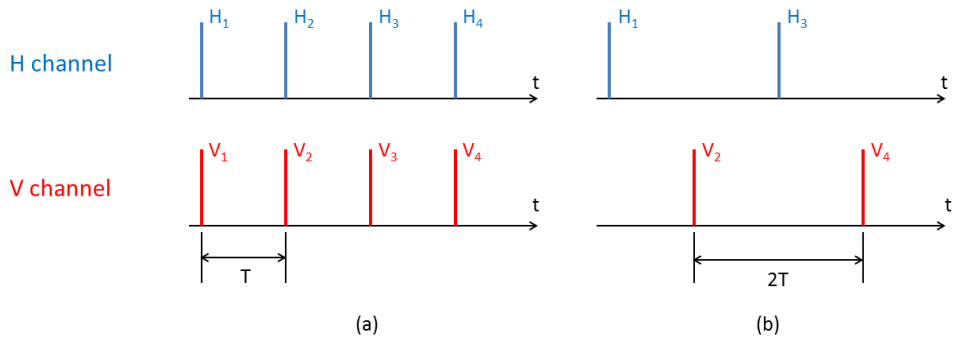

Figure 5.3: Schematic diagram of pulse sequences (Melnikov and Zrnić, 2015). (a) SHV mode; (b) AHV mode.

Most operational polarimetric weather radars operate in the SHV mode, and do not produce cross-polar measurements. RFI signals in the HH and VV channels will show correlation in this case, unless it is horizontally or vertically polarized. However in AHV

mode, the HH component is measured at a different time than the VV component, and therefore the RFI measured components will be uncorrelated.

Compared with the SHV mode, AHV mode has the advantage of straight-forward measurement of the cross-polar backscattering. In this case RFI simultaneously received in the copolar and cross-polar channels will have its components correlated. A drawback of AHV mode is the reduction of the maximum unambiguous Doppler velocity. This can be compensated for by advanced techniques (Unal and Moisseev, 2004). Polarimetric radar in AHV mode is also referred to as full-polarimetric weather radar. The dependency of RFI on the radar receiver has also been discussed in Meyer *et al.* (2013).

The RFI mitigation for polarimetric radar in both SHV and AHV mode will be discussed in this paper. The KNMI C-band radars operate in SHV mode and lack cross-polar measurements. The full-polarimetric radar data are from the X-band radar named the IRCTR drizzle radar (IDRA) (Figueras i Ventura, 2009). The simulated RFI will be added to IDRA data to quantify the performance of the filters proposed for polarimetric radar in AHV mode. Furthermore, to verify the effectiveness of the filters for SHV radar, the simulated RFI will also be added to KNMI radar data.

POLARIMETRIC OBSERVABLES

Before analyzing RFI effects, some polarimetric observables that will be used in the filters are introduced. First, following the backscatter alignment convention, the reflectivity which relates to range r is defined as

$$Z_{xy}(r) = C \cdot P_{xy}(r) \cdot r^2 = C \cdot \left|S_{xy}(r)\right|^2 \cdot r^2 \tag{5.2}$$

where $P_{xy}(r)$ is the backscattered power in one range bin with a transmitted y polarization and a received x polarization, and C is the calibration constant. Correspondingly, the well-known polarimetric observables, such as the differential reflectivity and the copolar correlation coefficient can be defined as

$$Z_{dr}(r) = \frac{Z_{hh}(r)}{Z_{vv}(r)} \tag{5.3}$$

$$\rho_{co}(r) = \frac{\left|\left\langle S_{hh}(r)\, S^*_{vv}(r)\right\rangle\right|}{\sqrt{\left\langle |S_{hh}(r)|^2\right\rangle \left\langle |S_{vv}(r)|^2\right\rangle}} \tag{5.4}$$

where $\langle\rangle$ in ρ_{co} represents the averaging, and $*$ is the complex conjugate.

Based on the combined simultaneous Doppler and polarization information, spectral polarimetry exhibits the microphysical and dynamical properties of weather radar targets. This is favorable for retrieval of atmospheric microphysical information and mitigation of non-atmospheric echoes at the same time. The spectral reflectivity which relates to range r and Doppler velocity v is expressed as

$$sZ_{xy}(r, v) = C \cdot sP_{xy}(r, v) \cdot r^2 = C \cdot \left|sS_{xy}(r, v)\right|^2 \cdot r^2 \tag{5.5}$$

where $sS_{xy}(r, v)$ represents the complex Doppler velocity spectrum, and $sP_{xy}(r, v)$ is defined as spectral power. Correspondingly, we can define the spectral differential reflectivity sZ_{dr}, the spectral linear depolarization ratios $sLDR^{hh}$ and $sLDR^{vv}$, and the

spectral copolar correlation coefficient $s\rho_{co}$ as

$$sZ_{dr}(r,v) = \frac{sZ_{hh}(r,v)}{sZ_{vv}(r,v)} \tag{5.6}$$

$$\begin{aligned} sLDR^{hh}(r,v) &= \frac{sZ_{vh}(r,v)}{sZ_{hh}(r,v)} \\ sLDR^{vv}(r,v) &= \frac{sZ_{hv}(r,v)}{sZ_{vv}(r,v)} \end{aligned} \tag{5.7}$$

$$s\rho_{co}(r,v) = \frac{\left|\left\langle S_{hh}(r,v)\, S^{*}_{vv}(r,v)\right\rangle\right|}{\sqrt{\left\langle |S_{hh}(r,v)|^2\right\rangle \left\langle |S_{vv}(r,v)|^2\right\rangle}} \tag{5.8}$$

where $\langle\rangle$ in $s\rho_{co}$ represents the averaging either in range or Doppler, with the latter being chosen in this paper. We will term the averaged observables as smoothed observables (e.g., smoothed $sLDR$). The averaging results in spectral polarimetric observables with lower variability, leading to thresholding techniques that better separate precipitation from clutter. However, the averaging also broadens the clutter to its neighboring bins in the range-Doppler domain, leading to incomplete clutter removal. This problem can be solved by advanced signal processing techniques proposed in the spectral polarimetric filter design (see Section 5.4).

After spectral polarimetric filtering, only the bins representing atmospheric signals are retained in the Doppler domain. Then, better noise-free standard observables can be estimated. E.g. the reflectivity in range bin r is expressed as

$$Z_{hh}(r) = C \cdot \sum_{v \in atm} (sP_{hh}(r,v) - sN) \cdot r^2 \tag{5.9}$$

where $v \in atm$ signifies that only those Doppler bins that contain atmospheric signals are used, and sN is the spectral noise for the chosen spectrogram. The spectral noise is estimated from a histogram of sP_{hh}. The most occurring bin value is regarded as the estimated spectral noise. The spectrogram-by-spectrogram noise estimation is inspired by Ivić *et al.* (2013), which is proposed to accurately produce estimates of the system noise power.

POLARIMETRIC SIGNATURE OF RFI AND PRECIPITATION

The measured polarimetric signature of RFI depends on the polarization of the RFI transmission. Also, the weather radar mode, SHV or AHV, leads to a different signature. Furthermore, in spectral polarimetric observables the RFI will be more or less uniformly distributed over all spectral bins, due to its noise like properties, as discussed in Section 5.2.2. Since atmospheric signals will always be contained in a part of the spectral bins, the filtering based on spectral polarimetric observables will lead to substantial improvement for RFI suppression, in a similar fashion as thermal noise and clutter can be suppressed in these observables. The polarimetric signature of RFI is expressed in Table 5.2.

The dB values of Z_{dr} will change from positive to negative when RF polarization gradually varies from horizontal to vertical. Z_{dr} values of precipitation concentrate around

Table 5.2: Polarimetric features of RFI versus the different RF polarization used.

variable \ RF pol	H pol	45° pol	V pol
$Z_{dr}(dB)$	inf	0	-inf
$LDR^{hh}(dB)$	-inf	0	inf
$LDR^{vv}(dB)$	inf	0	-inf
ρ_{co} in SHV mode	small	large	small
ρ_{co} in AHV mode	small		

0 dB (light rain) or are positive. This means that it is difficult to distinguish RFI from precipitation by using only Z_{dr} thresholding.

LDR^{vv} presents the same pattern for RFI as Z_{dr}, while LDR^{hh} has the opposite trend. The use of double LDR thresholding (Unal, 2009) provides a promising way to mitigate RFI from precipitation because both LDR^{hh} and LDR^{vv} of precipitation are of the same order and negative. This method requires cross-polar measurements and is therefore not suited for SHV type radars.

In contrast to the above mentioned polarimetric observables, ρ_{co} is phase sensitive, consequently the expression of RFI differs according to the polarimetric radar mode. For SHV mode, RFI will go into horizontal and vertical channels simultaneously, thus the strong correlation of RFI in the two channels will result in large ρ_{co} values, unless RFI is horizontally or vertically polarized. On the other hand, ρ_{co} values of RFI are small in the AHV mode. Due to the time delay between horizontal and vertical channels different RFI pulses are received in the two channels. For precipitation the coherence time is long enough to maintain large ρ_{co} values for both SHV and AHV mode. This provides a powerful way to mitigate RFI, suitable for both AHV and SHV mode radars, as will be shown later on.

In summary, RFI has a noise like signature in the spectral domain. However, its polarimetric signature differs from the noise one, which makes RFI a pseudo noise. Having built the polarimetric model of RFI, we analyze next the measured polarimetric signature of RFI based on the KNMI radar data.

PRACTICAL ANALYSIS OF SPECTRAL POLARIMETRIC FEATURES IN SHV RADAR

Spectral polarimetric observables are analysed in this section because of their better capabilities in RFI filtering, as discussed in the previous section. Data from the KNMI Herwijnen SHV radar are displayed in Fig. 5.2(a). Specifically, Ray 63, Ray 70 and Ray 215 are chosen as data with RFI contamination. All the spectral bins of the rays with RFI in the range interval between 140 km and 320 km km are taken. The chosen areas cover RFI with different INR values, including noise only bins. Experimental pdfs of spectral polarimetric observables of noise only and precipitation are given for comparison. They are displayed in Fig. 5.4(a) and (b). Since these KNMI radars do not measure the cross-polar backscattering, only sZ_{dr} and $s\rho_{co}$ will be considered.

The spectral differential reflectivity sZ_{dr} is a shape indicator of hydrometeors, and it has been investigated for clutter suppression to separate bird and insect echoes for wind retrievals (Bachmann and Zrnić, 2007). As shown in Fig. 5.4(a), the sZ_{dr} value

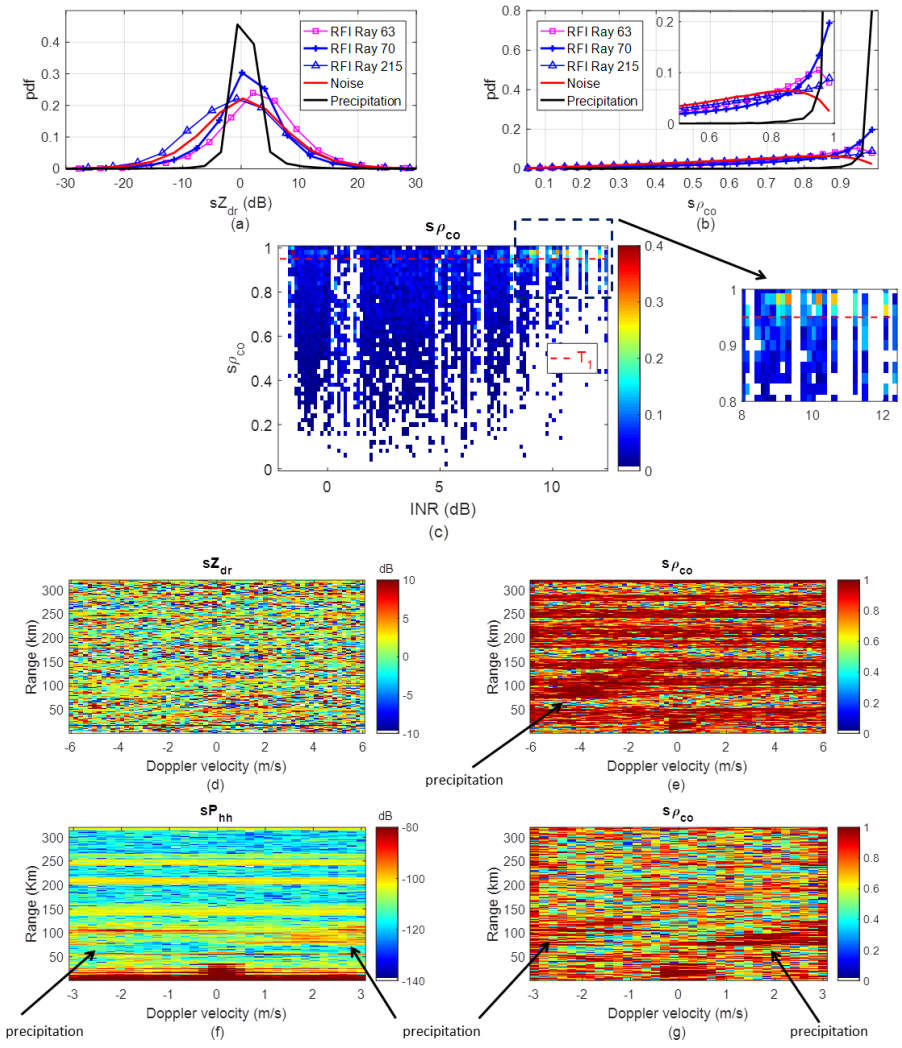

Figure 5.4: The spectral polarimetric variables of RFI in KNMI Herwijnen radar data. (a) experimental pdfs of sZ_{dr}; (b) experimental pdfs of $s\rho_{co}$; (c) $s\rho_{co}$ distribution versus INR; (d) sZ_{dr} spectrogram in SHV mode; (e) $s\rho_{co}$ spectrogram in SHV mode; (f) sP_{hh} spectrogram in AHV mode; (g) $s\rho_{co}$ spectrogram in AHV mode.

distribution of RFI varies from ray to ray, having positive, negative or zero mean value. Pure noise has a near-zero mean sZ_{dr} value. The sZ_{dr} values of both RFI and noise are broadly distributed in the interval of [−20 dB, 20 dB], while that of precipitation concentrates on [−3 dB, 4 dB]. In this case, all the sZ_{dr} values of RFI have a near-zero mean, indicating the RFI has a polarization of approximately 45°. One example of sZ_{dr} from Ray 70 is shown in Fig. 5.4(d). The overlapping values make it difficult, if not impossible to distinguish precipitation buried in noise and/or RFI using thresholding techniques.

The spectral copolar correlation coefficient $s\rho_{co}$, which is available for most polarimetric radar systems, has been used as an efficient classification observable (Moisseev and Chandrasekar, 2009). One key feature of $s\rho_{co}$ is that its value is very close to 1 for most hydrometeors and significantly lower than 1 for non-meteorological scatterers measured in the sidelobes of the antenna pattern. The $s\rho_{co}$ values of the KNMI Herwijnen radar are calculated using a running average on 3 consecutive Doppler bins. As discussed in the previous section, for RFI with arbitrary polarization (not strictly H or V) high values near 1 are expected in SHV mode. Indeed in Fig. 5.4(b) high values of $s\rho_{co}$ are found for RFI bins. The pdf indicates that 8% to 20% of the RFI data have high $s\rho_{co}$ values larger than 0.95. The bins with lower values contain also noise, as is indicated by the INR. When INR is low, the spectral polarimetric features of RFI and noise tend to be the same. As is mentioned in Section 5.2.2, Ray 70 has the largest INR, followed by Ray 63, then Ray 215. This is consistent with the pdf of the $s\rho_{co}$ values close to 1 (see the zoom-in part in Fig. 5.4(b)).

To further explore the influence of INR on $s\rho_{co}$ values, we display the same $s\rho_{co}$ data versus INR and normalize the frequency of $s\rho_{co}$ values in each INR bin, as shown in Fig. 5.4(c). We observe that when the INR is less than 5 dB, $s\rho_{co}$ values are broadly distributed in the interval of [0, 1]. As INR increases, the $s\rho_{co}$ values tend to concentrate to 1, with most values greater than 0.95. In addition, one example of $s\rho_{co}$ from Ray 70 (the ray with the largest INR) is shown in Fig. 5.4(e). The precipitation, which is almost masked by RFI, is located in the range of 100 km - 150 km at the negative Doppler velocity side.

RFI suppression in SHV radar can be achieved, if correlated channels are removed for the $s\rho_{co}$ estimation. Thus, from each set of simultaneously measured H and V polarization, either the H or V channel is discarded, in an alternating scheme. Specifically, data of H_{2m-1} and V_{2m} (or H_{2m} and V_{2m-1}) in Fig. 5.3(a) are used, where $m = 1, 2, ..., M/2$ and M is the total number of samples in the dwell time. The resulting datastream resembles an AHV radar one. Taking the H_{2m-1} samples, the spectral power sP_{hh} is generated as displayed in Fig. 5.4(f). Combined with V_{2m} samples, we have the $s\rho_{co}$ spectrogram as shown in Fig. 5.4(g), in which the polarimetric correlation of RFI has significantly decreased but that of precipitation stands out. Implementing the spectral polarimetric filters based on Fig. 5.4(g) preserves the precipitation and removes the RFI, providing a way to mitigate the RFI in SHV radar.

A disadvantage of this method is the decrease in maximum unambiguous Doppler velocity by a factor of 2 because the time between two consecutive samples is doubled, resulting in Doppler aliasing. The precipitation is now mainly located in the area of positive Doppler velocities. However, this problem is well-known from AHV mode radars and correction methods have been published (Unal and Moisseev, 2004).

To conclude, on one hand, RFI in polarimetric radar can be regarded as white noise in the spectral domain for each channel (also applied to single polarization radar). On the other hand, considering the correlation between two channels, different polarimetric radar types have different impacts. For SHV radar, the RFI sensed by the horizontal and vertical channels will be the same and correlated. While for AHV radar, RFI detected by the two consecutive channels will be independent. The RFI simulation in the Section 5.3 where the RFI is 45° polarized follows these assumptions.

5.3. RFI SIMULATION IN RADAR

5.3.1. SIMULATED RFI IN SINGLE POLARIZATION RADAR

For simulation of RFI, it is important to know the approximate RFI signal level that may be expected. For various reasons, it may be different from radar to another. However, if the RFI level is expressed in forms of the radar's thermal noise, it can be transferred to other radars and lead to comparative results in RFI mitigation because the SPFs operate on the noise in radar data. Thus, for a given radar, the mitigation that can be expected follows from a measurement of the INR, and from comparison with the result, in this paper.

The weather radar equation in the presence of noise and RFI is first derived. Rewriting Eq. (5.2) to express the reflectivity, we have

$$Z_{hh} = C \cdot P_{hh} \cdot r^2 \tag{5.10}$$

In the presence of RFI, P_{hh} will contain thermal noise and RFI. As mentioned in Section 5.2.2, RFI can be simulated by noise in the spectral domain. The received power, P_{hh}, results from the integration of the spectral power. Thus, we define the total noise N_{tot} in P_{hh} as

$$N_{tot} = N_{th} + N_{RFI} = N_{th}(1 + INR) \tag{5.11}$$

where N_{th} is the estimated thermal noise, N_{RFI} is the RFI power, and the INR is defined as

$$INR = \frac{N_{RFI}}{N_{th}} \tag{5.12}$$

The noise equivalent reflectivity Z_{noise} is the value where P_{hh} equals N_{th}. This is the smallest reflectivity value that can be measured by a radar, and it is range dependent as shown in Fig. 5.2(a). In the case of RFI, Z_{noise} is increased because of the additional noise power N_{RFI}.

Now the INR of the KNMI Herwijnen data can be measured. The INR, which is range independent, can be obtained by comparing the RFI-contaminated reflectivity Z_{RFI} and noise equivalent reflectivity Z_{noise} in the reflectivity PPI

$$INR(r) = \frac{Z_{RFI}(r) - Z_{noise}(r)}{Z_{noise}(r)} \tag{5.13}$$

Considering the KNMI Herwijnen data in Fig. 5.2(a), the calculated maximum INR is 16.5 dB. This makes the INR range of 10 dB to 20 dB of particular interest to study the performance of RFI filters.

5.3.2. SIMULATED RFI IN AHV RADAR

The RFI simulation uses the IDRA radar data. IDRA is a high-resolution X-band full-polarimetric Doppler weather radar designed specifically for atmospheric research. The scanning radar operates at a speed of 1 rpm, and its measurements are shown in near real-time. All the radar data recorded from April 2009 onward are freely accessible to the public via the 4TU.centre for Research Data. These data provide long-term observations of trends in precipitation change. The specifications of the FMCW radar are shown in

Table 5.3: IDRA Specifications (Figueras i Ventura, 2009). The boldface indicates parameters used for the operational mode.

Radar type	Linear FMCW
Transmitter type	Solid state
Polarization	Full-polarimetric
Center frequency (GHz)	9.475
Transmitted power (W)	1, 2, 5, 10, **20**
Range resolution (m)	3, 6, 15, **30**
Sweep time (μs)	204.8, **409.6**, 8192.2, 1638.4, 3276.8
Frequency excursion (MHz)	**5**, 10, 20, 50
Antenna beamwidth	1.8°
Operational angles	Elevation 0.5°, Azimuth 0° - 360°

Table 5.3. Note that sweep time, which is the terminology for FMCW radar, is equivalent to the pulse repetition time for pulse radar. For the Doppler processing, the number of sweeps in the Fourier transform window is set to be 512 (standard processing), which corresponds to a Doppler resolution of 3.8 cm s^{-1}. The related azimuth angle resolution is 2.5°.

To simulate the situation where AHV radar is contaminated by RFI, white noise with different INR can be added to the IDRA data. One IDRA measurement at 00:00 UTC on April 26th 2017 (the raw reflectivity PPI is shown in Fig. 5.5(a)) is considered. Adding the RFI with an INR of 13 dB to the range-Doppler spectrograms related to Rays 83 - 85 and Rays 120 - 122, yields the simulated RFI-contaminated PPI of IDRA (Fig. 5.5(b)). The RFI is clearly visible along the whole range in the two azimuth directions. The raw range-Doppler spectrogram of the power is displayed in Fig. 5.5(c) and the RFI-contaminated one in Fig. 5.5(d).

In the spectrograms, the ground truth areas of precipitation are manually selected, and depicted with a black contour. The manual selection yields a binary mask where "1" represents precipitation. The selection is based on three criteria: 1) the range-Doppler continuity of precipitation; 2) spectral signal to noise ratio thresholding; 3) spectral polarimetric values ($sLDR$ and $s\rho_{co}$) thresholding. Specifically, any bin in the range-Doppler spectrogram with a spectral power less than the estimated noise will be removed; any bin with a $sLDR$ value larger than the set threshold and a $s\rho_{co}$ value smaller than the set threshold will be mitigated. These thresholds are obtained from the clutter and precipitation spectral polarimetric value distributions. In addition, the precipitation should be continuous in the range-Doppler spectrogram. By using image processing techniques (i.e., the mathematical morphology), some of the zeros inside the precipitation mask are filled.

The noise level of the RFI-contaminated spectrogram is increased by about 13 dB, masking weak precipitation (e.g., the boundary precipitation) or other weak clutter (e.g., the artifacts indicated by a red arrow in Fig. 5.5(c)). Note that the artifacts show up in a similar way as RFI in the radar PPI (e.g., Fig. 5.5(a)). However, unlike RFI, they are

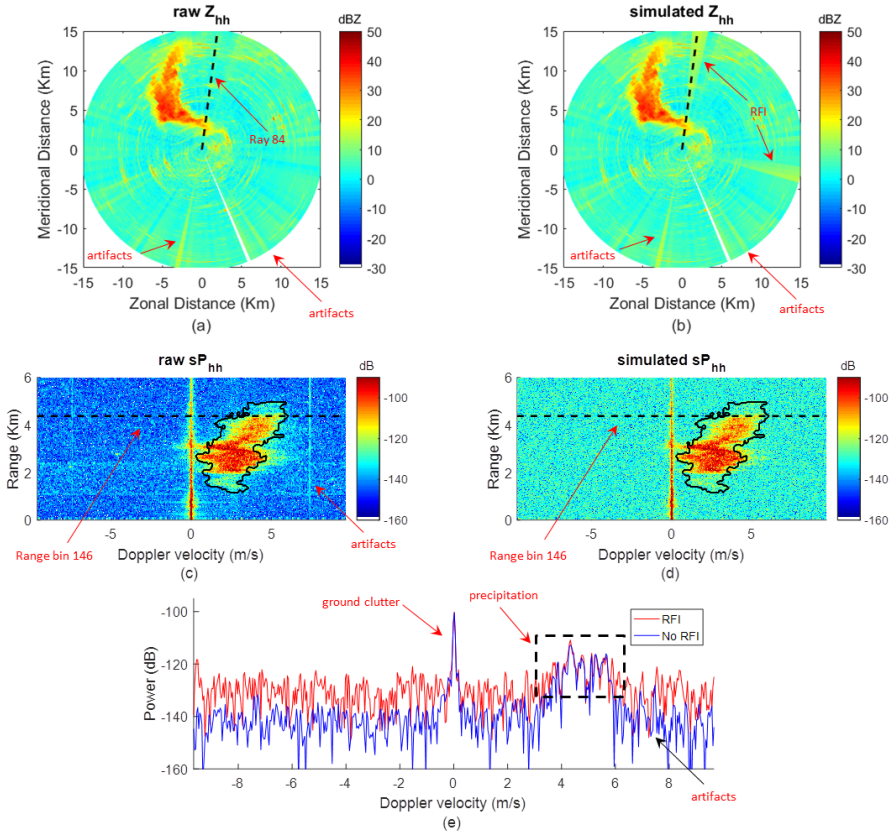

Figure 5.5: IDRA radar measurements. (a) raw reflectivity PPI; (b) raw reflectivity PPI with simulated RFI; (c) range-Doppler spectrogram of Ray 84; (d) range-Doppler spectrogram of Ray 84 with RFI (INR 13 dB); (e) Doppler spectra of range bin 146 (i.e., 4.38 km) with and without simulated RFI.

narrow-band in the Doppler domain (e.g., Fig. 5.5(c)). The exact phenomena responsible for producing the artifacts in the radar data remain unknown at this point, but the artifact features have been exhaustively studied in Yin *et al.* (2017b, 2018, 2019), and artifacts can be referred to as narrow-band moving clutter.

Finally, the Doppler spectra of range bin 146 (i.e., 4.38 km) with and without the additional RFI are displayed in Fig. 5.5(e). We can see that the whole noise floor is increased, which is consistent with Joe *et al.* (2005). However, those Doppler bins with large backscattered power remain the same, namely the precipitation centered around $5\,\mathrm{m\,s^{-1}}$ and the ground clutter centered around $0\,\mathrm{m\,s^{-1}}$. The increased noise (i.e., RFI) should be mitigated, otherwise it will bias the radar observable estimation.

5.3.3. Practical analysis of spectral polarimetric features in AHV radar

The spectral polarimetric parameters measured by AHV radar are going to be discussed using IDRA data. Taking the data collected at 00:00 UTC on April 26th 2017 whose spectral power sP_{hh} (no RFI is added) is shown in Fig. 5.5(c), the spectral polarimetric variables of Ray 84 are displayed in Fig. 5.6.

The sZ_{dr} values measured by the AHV radar (Fig. 5.6(a)) tend to have similar features as those discussed for SHV radar (Fig. 5.4(a)). Thus, sZ_{dr} may not be a desirable variable to distinguish precipitation from clutter.

The $s\rho_{co}$ values of RFI tend to be small because the two signals, HH and VV, used to calculate the polarimetric correlation are modeled independently. In this case, the $s\rho_{co}$ of noise can represent that of RFI. Fig. 5.6(d) shows that $s\rho_{co}$ values of thermal noise from the radar are randomly distributed between 0 and 1 in the range-Doppler spectrogram and are not continuous. The distribution will not change if we increase the noise level, e.g., by adding RFI. This feature is favorable for RFI and noise mitigation. However, ground clutter and narrow-band moving clutter (i.e., artifacts), indicated by red arrows, have the same $s\rho_{co}$ values as precipitation, which means that other techniques should be combined to keep only precipitation. Note that the $s\rho_{co}$ values of IDRA data are calculated using a running average on 7 consecutive Doppler bins.

As for the spectral linear depolarization ratio $sLDR$ (i.e., $sLDR^{hh}$ and $sLDR^{vv}$), its values for precipitation are relatively small and will increase due to contamination from noise and clutter. It can be estimated that $sLDR^{hh}$ and $sLDR^{vv}$ values of RFI are not simultaneously small because it largely depends on the polarization of the RF device. In the case of 45° polarization RFI, we have $sLDR^{hh} \approx sLDR^{vv} \approx 0$ dB which is a noise signature. Based on the similar sZ_{dr} and $s\rho_{co}$ value distributions of RFI and noise for AHV radar, we assume that the $sLDR$ values of RFI are also close to that of noise. As shown in Fig. 5.6(b) and (c), precipitation has the smallest $sLDR$ values compared with noise. It is verified that the larger the signal to noise ratio (SNR), the smaller the $sLDR$ of precipitation (Unal, 2009; Yin *et al.*, 2019). The signature of $sLDR$ of weak precipitation is similar to that of noise; nonetheless, the range-Doppler continuity of precipitation can be used to design the filter to retain the weak precipitation.

In addition, since the influence of RFI on precipitation in the spectral domain is actually the increased noise in all the observables, it will lead to the values of spectral polarimetric observables of precipitation approaching those of noise. One example of the $sLDR^{hh}$ and $s\rho_{co}$ versus different INR is shown in Fig. 5.7. Specifically, RFI with an INR 10 dB is shown in Fig. 5.7(a) and (b), while an INR 20 dB RFI is added in Fig. 5.7(c) and (d). As INR increases, precipitation with smaller SNR tends to be masked by RFI, thus more precipitation signal will be lost, a feature which is more obvious in Fig. 5.7(c) and (d) than in Fig. 5.7 (a) and (b). Additionally, the $sLDR$ values of precipitation increase due to the influence of RFI, which is indicated by the large-intensity precipitation changing from dark blue in Fig. 5.6(b) to light blue in Fig.5.7 (c). Similarly, the $s\rho_{co}$ values of precipitation decrease from Fig. 5.6(d) (without RFI) to Fig. 5.7(b) (INR is 10 dB) and further with Fig. 5.7(d) (INR is 20 dB).

In summary, the spectral polarimetric variables of precipitation are biased by the presence of large power RFI. For AHV radar, $sLDR$ and $s\rho_{co}$ can be desirable spectral

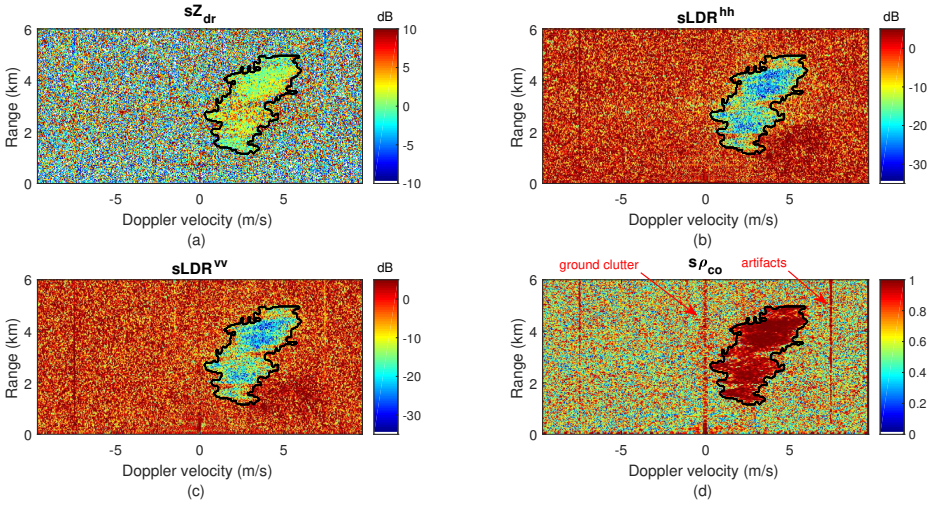

Figure 5.6: Spectral polarimetric observables of IDRA (without RFI). Data are related to Ray 84 measured at 00:00 UTC on April 26th 2017. (a) spectral differential reflectivity sZ_{dr}; (b) spectral linear depolarization ratio $sLDR^{hh}$; (c) spectral linear depolarization ratio $sLDR^{vv}$; (d) spectral copolar correlation coefficient $s\rho_{co}$.

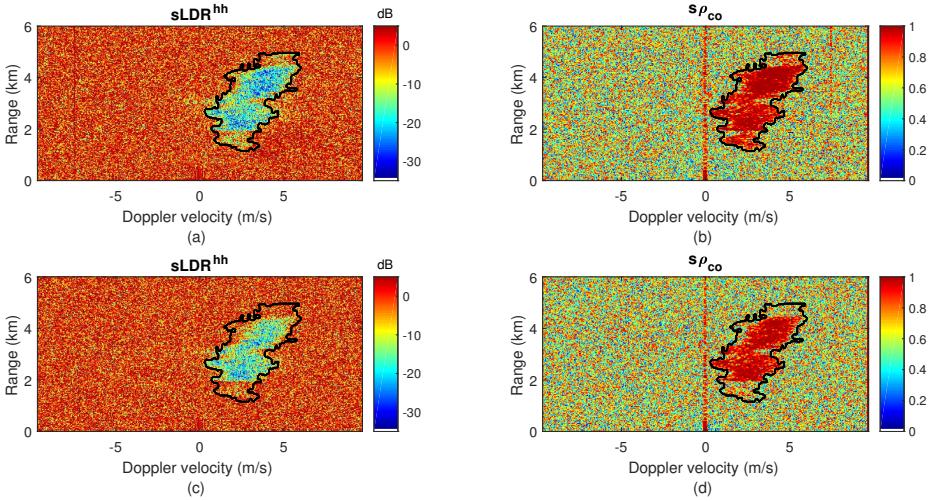

Figure 5.7: Spectral polarimetric observables with different INR. (a) $sLDR^{hh}$ with INR 10 dB; (b) $s\rho_{co}$ with INR 10 dB; (c) $sLDR^{hh}$ with INR 20 dB; (d) $s\rho_{co}$ with INR 20 dB.

polarimetric observables for RFI mitigation.

5.3.4. SIMULATED RFI IN SHV RADAR

Analogously, an INR of 10 dB is added to Rays 83 - 84, Rays 120 - 121 and Rays 160 - 161 of the KNMI Herwijnen data shown in Fig. 5.2. The simulated result is displayed in Fig. 5.8, and RFI rays similar to the IDRA case are observed. Note that Rays 160 - 161 cross the

precipitation, which provides a good evaluation case for the filters, which are described in Section 5.4.

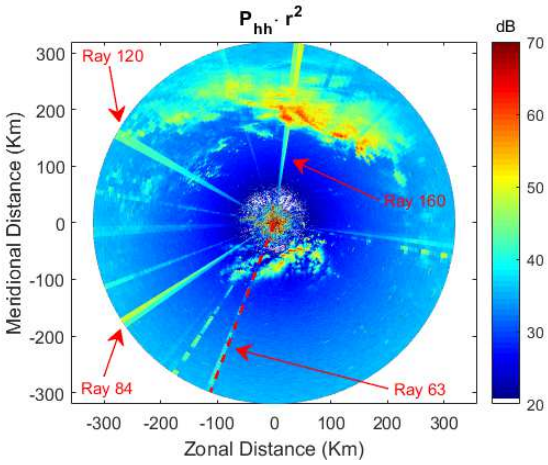

Figure 5.8: Simulated RFI with INR 10 dB added to the KNMI Herwijnen radar data.

5.4. SPECTRAL POLARIMETRIC FILTERS

Recently, two SPFs (i.e. the MDsLDR filter (Yin *et al.*, 2017b) and the OBSpol filter (Yin *et al.*, 2019)) were designed by the authors for narrow-band clutter (i.e. ground clutter and moving artifacts) and noise mitigation. Based on the difference of spectral polarimetric features and range-Doppler continuity of precipitation and clutter, these filters have been proved effective and their performance has been validated by several case studies. The SPFs can be very general, and in this paper, they are analyzed for the RFI mitigation. In this section, the MDsLDR filter and the OBSpol filter will be described briefly, and their applications to radar measurements are discussed.

The flowcharts of the MDsLDR filter and the OBSpol filter are shown in Fig. 5.9. Both filters are implemented in the range-Doppler domain, such that the input is a raw spectrogram and the output is the filtered one. The two filters generate a binary filtering mask indicating precipitation, which contributes to keep the complete information of precipitation. Moreover, both techniques can be applied in real-time due to their low computational complexity. It has been proved that the OBSpol filter and the MDsLDR filter remove narrow-band clutter and noise similarly well. However, the OBSpol filter better preserves weak precipitation (Yin *et al.*, 2019). Both filters cannot retrieve the precipitation accurately in the range-Doppler spectrogram when clutter and precipitation overlap.

5.4.1. MDSLDR FILTER

The MDsLDR filter is divided into 4 main steps. First, after the double $sLDR$ (i.e., $sLDR^{hh}$ and $sLDR^{vv}$) filtering (thresholding technique), a mask indicating precipitation is ob-

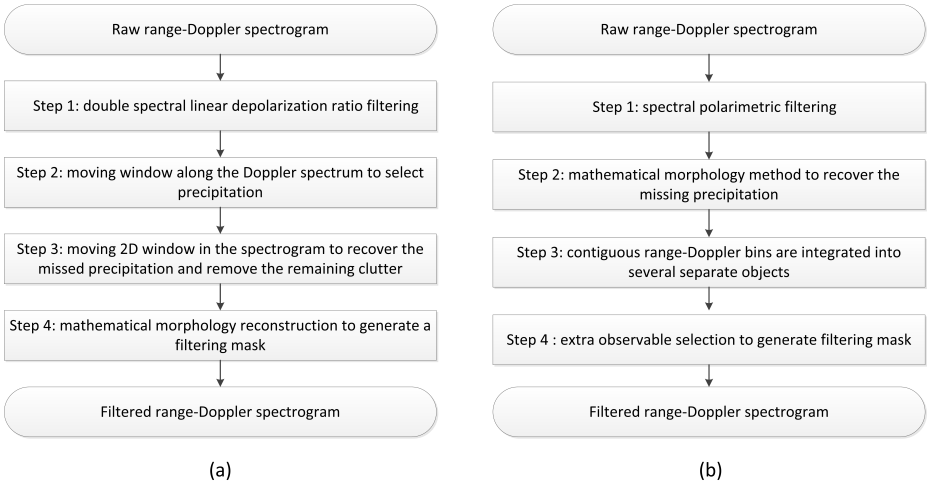

Figure 5.9: Flowchart of the spectral polarimetric filters applied to RFI mitigation. (a) the MDsLDR filter; (b) the OBSpol filter.

tained. Second, a moving window along the Doppler domain is applied to the mask to mitigate narrow-band clutter. Third, a moving 2D window is implemented to reconstruct the removed precipitation and eliminate the remaining clutter. Fourth, the mathematical morphology method (closing operator) is used to further recover the precipitation. A binary filtering mask $M \in \{0, 1\}$ is generated after the above 4 steps and is applied to the raw range-Doppler spectrogram. The filtered spectrogram should then keep only the precipitation and discard the clutter and noise.

The limitation of the MDsLDR filter is that *sLDR* measurements are not available for most polarimetric radars. Note that *sLDR* used here is not averaged. While averaging preserves more boundary precipitation it also retains more clutter (e.g. narrow-band moving artifacts). We try to design a multi-functional filter for different types of clutter. The performance of the MDsLDR filter in the RFI mitigation will be given later using radar measurements.

5.4.2. OBSPOL FILTER

Similar to the MDsLDR filter, the OBSpol filter also contains 4 steps. First, the spectral polarimetric observables are utilized to generate a binary mask where "1" indicates the precipitation (thresholding technique). In Step 2, the same mathematical morphology method as for the MDsLDR filter is used to recover the missing precipitation areas of the obtained mask. Based on the reconstructed mask in Step 2, the contiguous bins having values "1" are selected and integrated into several separate areas in the range-Doppler spectrogram termed as "objects" in Step 3. Next in Step 4, whether the produced objects are precipitation or not is further decided based on the appropriate observable. Thus, a filtering mask can be obtained by summing up the filtered separated objects.

It is recommended that a proper Doppler dealiasing technique is used before the implementation of the OBSpol filter. After the dealiasing technique, precipitation is in-

tegrated into a small amount of objects. Note that the spectral polarimetric variables in Step 1 can be $sLDR$ (double $sLDR$, namely $sLDR^{hh}$ and $sLDR^{vv}$) or $s\rho_{co}$, leading to two versions of the OBSpol filters, which are applicable to polarimetric radar with (i.e., AHV mode) and without cross-polar measurements (i.e., SHV mode). As visualized in Fig. 5.4(e) and (g), the $s\rho_{co}$ differences between precipitation and RFI become larger in the AHV mode.

Therefore, the pulse sequences of SHV radar can be divided into two sub-sequences (i.e., H_{2m-1} and V_{2m} and H_{2m} and V_{2m-1} from Fig. 5.3(a)). Such division helps to decorrelate the RFI between two consecutive channels. Hereafter, for SHV radar, we refer to the conventional $s\rho_{co}$ as SHV $s\rho_{co}$, and the one derived from sub-sequences as AHV $s\rho_{co}$. After filtering by the OBSpol filter with AHV $s\rho_{co}$, the subsequent results can be merged. In this paper, the merging method is performed by the simple summation of two sub-spectrograms; a proper Doppler dealiasing method (e.g., Unal and Moisseev (2004)) remains for future work. The power-related variables, such as reflectivity and differential reflectivity, can be obtained after the filtering. Note that a ground clutter suppression technique should be included in Step 1 due to the inability of the filter using only $s\rho_{co}$ to remove ground clutter.

Additionally, as mentioned in Section 5.2.3, the smoothed $sLDR$ is used instead of the raw one because the smoothed $sLDR$ has lower variability. For the problem of clutter broadening, advanced signal processing methods, such as clutter filtering based on individual objects in the range-Doppler domain, can be used. For the application of the OBSpol filter in the RFI suppression, we define two filters: 1) the OBSpol filter with $sLDR$ (smoothed) and 2) the OBSpol filter with $s\rho_{co}$ (the notch filter around 0 m/s is included in Step 1). Note that the smoothed $sLDR$ values of IDRA data are calculated also by a running average on 7 consecutive Doppler bins.

5.4.3. STANDARD PROCESSING

To make a comparison of the above three filters in AHV radar, we will also present the RFI mitigation results with the standard processing (SP) of IDRA. Currently, the standard clutter suppression processing is implemented in real-time in the IDRA system to generate the radar PPI online. Long-term observations show that the IDRA has suffered from moving artifacts of increasing severity each year since its installation. The SP is also carried out in the range-Doppler domain. It consists of a narrow notch filter centered around $0\,\mathrm{m\,s^{-1}}$ and the double spectral linear depolarization ratio (DsLDR) filter (Unal, 2009). Furthermore, a noise clipping technique is implemented. It keeps the Doppler bins related to a spectral power of at least 3 dB above the noise level in the Doppler domain. Finally, isolated Doppler bins and Doppler spectra containing less than 2% of Doppler bins are discarded. The DsLDR filter is based on the different $sLDR$ distributions of precipitation and clutter. Specifically, bins in the range-Doppler spectrogram will be removed if the corresponding $sLDR$ is larger than the set threshold which is given based on clutter and precipitation removal percentage.

5.5. FILTER APPLICATION TO RADAR MEASUREMENTS

After the introduction of all the filters, this section will show the RFI filtering results. Also the performance comparison using simulated RFI data (i.e., IDRA and KNMI Herwijnen radar) and real RFI data (i.e., KNMI Herwijnen radar) will be made. The results will be displayed using spectrograms and PPI images.

The parameter selections in the SPFs were well documented in Yin *et al.* (2017b) and Yin *et al.* (2019). The application there was narrow-band clutter and noise mitigation. Specifically, Step 2 of the MDsLDR filter and Step 4 of the OBSpol filter were designed to achieve this type of clutter mitigation. Since the proposed SPFs can be very general due to different combinations of spectral polarimetric observables, they are multi-functional and are analyzed here for the application of RFI mitigation. Based on the facts that 1) RFI acts as noise with larger power in the range-Doppler spectrogram, and 2) the proposed SPFs can remove the noise, it is expected that good RFI mitigation performance can be achieved by keeping the same steps in the original SPFs. In addition, the narrow-band clutter is removed. Hence, we keep the same parameter selection in the SPFs design for the RFI removal as in (Yin *et al.*, 2017b, 2019).

5.5.1. APPLICATION TO AHV RADAR DATA

To quantify the spectral polarimetric filters in RFI mitigation for AHV radar, one study case of IDRA measurements, Ray 84 of Fig. 5.5(d) is used. As discussed, the data contain narrow-band moving artifacts, and they are masked with RFI having an INR of 13 dB. After the SP as shown in Fig. 5.10(a), some precipitation signal is lost and some RFI signature is retained. While the spectral polarimetric filters can completely remove the RFI, this is at the expense of some precipitation loss. In this case, in terms of retaining "precipitation areas" (the precipitation may be contaminated by RFI), the best performance seems to be obtained with the OBSpol with $sLDR$ in Fig. 5.10(d), while the MDsLDR is second best, followed by the OBSpol with $s\rho_{co}$. Quantitative analysis of estimated radar variables are provided next.

To quantify the impact of different INR on the precipitation preservation, following the theory of confusion matrix (Fawcett, 2006), we define the detection probability (i.e., sensitivity) of precipitation P_d as

$$P_d = \frac{\mathrm{TP}}{\mathrm{TP}+\mathrm{FN}} \tag{5.14}$$

where TP is the number of precipitation bins successfully identified and FN is the number of precipitation bins classified as clutter and noise. The false alarm rate (i.e., fall-out) P_{fa} is defined as the clutter and noise areas divided by the true non-precipitation ones.

$$P_{fa} = \frac{\mathrm{FP}}{\mathrm{FP}+\mathrm{TN}} \tag{5.15}$$

where FP is the number of clutter and noise bins classified as precipitation, and TN is the number of clutter and noise bins successfully identified.

In addition, the root mean square error (RMSE) is used to quantify the filtering performance. Supposing a given spectrogram, where we have R range bins with precipita-

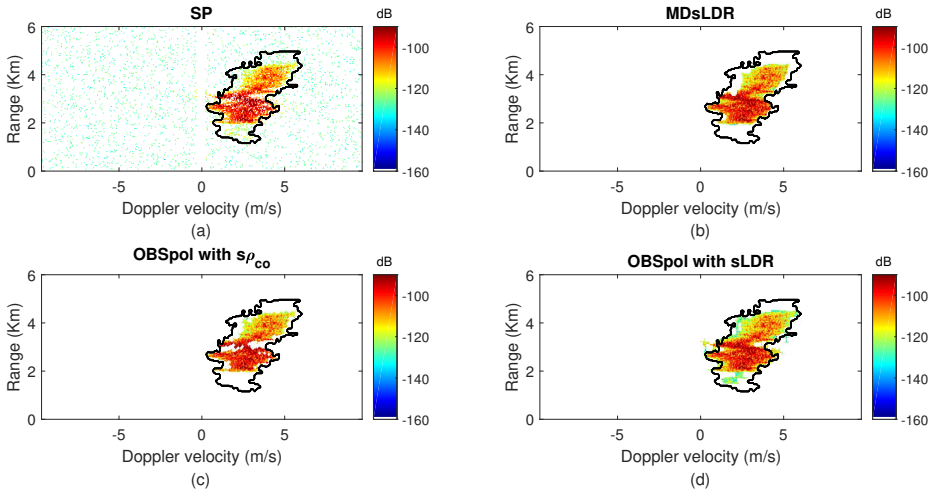

Figure 5.10: Different filtering techniques applied to range-Doppler spectrograms with simulated RFI (INR 13 dB). (a) the standard processing; (b) the MDsLDR filter; (c) the OBSpol filter with $s\rho_{co}$; (d) the OBSpol filter with $sLDR$.

tion, the RMSE of a specific observable X can be expressed as

$$\delta X = \sqrt{\frac{1}{R}\sum_{r=1}^{R}\left(X^{tru}(r) - X^{est}(r)\right)^2} \tag{5.16}$$

where $X^{tru}(r)$ is the true observable value in the r^{th} range bin, which is manually selected, and $X^{est}(r)$ is the filtered observable value in the r^{th} range bin. Note that the observable X can be reflectivity Z_{hh}, differential reflectivity Z_{dr} or copolar correlation coefficient ρ_{co}. Due to the azimuthal discontinuity problem of Z_{dr} in IDRA (Yin *et al.*, 2017b), only Z_{hh} and ρ_{co} will be considered in the research.

The P_d and P_{fa} versus different INR are shown in Fig. 5.11(a) and (b). The INR interval of the additional RFI is [−10 dB, 20 dB]. P_d decreases with the increase of INR, which is due to weaker precipitation being masked ($sLDR$ values of precipitation increase and $s\rho_{co}$ values of precipitation decrease). All the P_{fa} values obtained from different filters are relatively small, and those of SPFs are negligible. The δZ_{hh} of SPFs are not as sensitive to large INR, as shown in Fig. 5.11(c). While the δZ_{hh} of SP increases with the INR. The reason is that when INR is large, SPFs will only retain precipitation with large intensity, and SP will also keep some precipitation which has been contaminated by RFI. In this specific case, when INR is smaller than 10 dB, the δZ_{hh} after the OBSpol filter with $s\rho_{co}$ has the largest value because of the removal of some high-intensity precipitation at Range 3 km. One example is displayed in Fig. 5.10(c). In addition, indicated by Fig. 5.11(d), the $\delta\rho_{co}$ has similar tendency with the δZ_{hh}.

To further quantify the polarimetric variable quality, three other precipitation cases are chosen, as shown in Table 5.4. Five consecutive rays of each case in which clutter and precipitation do not overlap and are free of Doppler aliasing are selected. For these

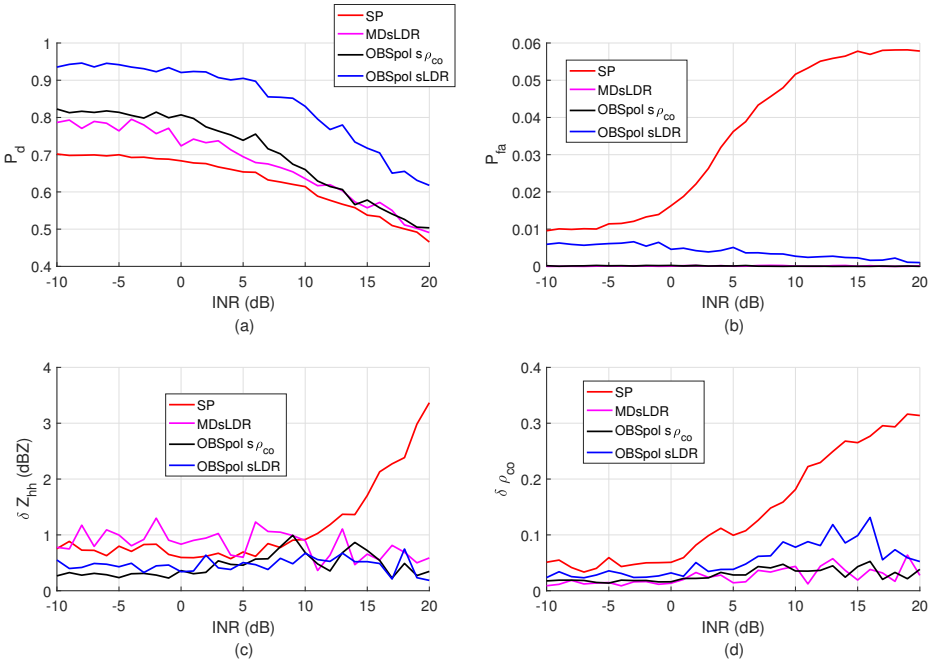

Figure 5.11: (a) P_d, (b) P_{fa}, (c) δZ_{hh} and (d) $\delta \rho_{co}$ of different filtering techniques versus different INR.

data, the true precipitation is manually selected in the range-Doppler spectrogram, and we add an INR of 10 dB. The RMSE results are shown in Table 5.5. Note that "RFI biased" means that the variables are calculated by using data located in the true precipitation areas but contaminated by addition of RFI.

As shown in Table 5.5, when the precipitation is contaminated by RFI, both δZ_{hh} and $\delta \rho_{co}$ of the "RFI biased" are the largest, the average δZ_{hh} being 3.81 dBZ and average $\delta \rho_{co}$ being 0.132. The δZ_{hh} and $\delta \rho_{co}$ values of the SP and the OBSpol filter with $sLDR$ are comparable. The reasons are that the SP keeps more RFI due to the incomplete clutter removal and the OBSpol filter with $sLDR$ retains more boundary precipitation (these precipitation has been contaminated by RFI). This is illustrated in Fig. 5.10(a) and (d). With the average δZ_{hh} being 0.88 dBZ and average $\delta \rho_{co}$ being 0.052, the MDsLDR filter has better performance in RFI mitigation. While the OBSpol filter with $s\rho_{co}$ is the best among all the techniques. Based on this study, the OBSpol filter with $sLDR$ may retain more precipitation data at the cost of their quality. If this is the case, the $sLDR$ thresholding can be set more strict (e.g., change of threshold) in precipitation preservation.

To better visualize the performances of different filtering techniques, the scatter plots between the true reflectivity and the reflectivity obtained by different filtering techniques are provided in Fig. 5.12. Note that when the range bins with precipitation are mitigated by filters, their reflectivity will be labeled as −30 dBZ. The chosen data are Ray 54 of Case 1, and the RFI with INR 10 dB (indicated by red points) and INR 20 dB (indicated by blue points) are added to the raw data, respectively. When the INR is set to be 10 dB, the

Table 5.4: Precipitation cases used to quantify the filter performance.

Case No.	Date & Time	Rain Type
1	2011-07-01 02:00	moderate
2	2014-08-22 13:00	moderate
3	2017-06-06 08:00	moderate

Table 5.5: RMSE of radar observables.

Case No.	Ray No.	RFI biased		SP		MDsLDR		OBSpol $s\rho_{co}$		OBSpol $sLDR$	
		δZ_{hh}	$\delta\rho_{co}$	δZ_{hh}	$\delta\rho_{co}$	δZ_{hh}	$\delta\rho_{co}$	δZ_{hh}	$\delta\rho_{co}$	δZ_{hh}	$\delta\rho_{co}$
1	53	1.74	0.141	1.30	0.213	0.65	0.033	0.69	0.040	1.66	0.203
	54	2.42	0.145	1.71	0.203	1.01	0.058	0.95	0.044	2.68	0.229
	55	1.19	0.112	1.10	0.190	0.67	0.063	0.73	0.047	1.24	0.245
	56	2.28	0.101	1.07	0.162	0.52	0.029	0.65	0.029	1.17	0.206
	57	3.59	0.173	2.91	0.253	0.92	0.073	1.07	0.058	3.28	0.281
2	18	4.74	0.078	0.32	0.146	0.81	0.056	0.71	0.040	1.21	0.185
	19	5.10	0.098	0.87	0.157	0.80	0.073	0.54	0.033	1.03	0.188
	20	4.02	0.065	0.35	0.124	0.39	0.048	0.64	0.029	1.14	0.168
	21	4.26	0.099	0.69	0.168	1.29	0.096	0.61	0.034	0.96	0.200
	22	3.95	0.069	0.41	0.158	0.40	0.071	0.53	0.036	1.80	0.202
3	10	5.87	0.160	1.51	0.180	0.75	0.039	0.64	0.026	1.18	0.058
	11	4.47	0.143	1.11	0.159	0.70	0.025	0.43	0.022	1.17	0.082
	12	4.86	0.163	1.81	0.181	1.00	0.027	0.93	0.034	0.96	0.067
	13	4.55	0.220	1.95	0.235	1.22	0.029	0.95	0.034	0.99	0.102
	14	4.21	0.217	2.44	0.228	1.67	0.051	0.71	0.039	0.80	0.073
average		3.81	0.132	1.33	0.183	0.88	0.052	0.72	0.037	1.45	0.167

precipitation with reflectivity values less than 15 dBZ is contaminated. After the SP and the OBSpol filter with $sLDR$, some RFI contaminated precipitation is preserved, whose Z_{hh} is less than −5 dBZ. While MDsLDR filter and the OBSpol filter with $s\rho_{co}$ can completely remove the RFI contaminated precipitation, and retain precipitation with Z_{hh} larger than 0 dBZ. The residual RFI contaminated precipitation results in the increase of the δZ_{hh}. In addition, with the increase of INR, more contaminated precipitation is kept after the SP and the OBSpol filter with $sLDR$. Whereas the MDsLDR filter and the OBSpol filter with $s\rho_{co}$ tend to retain the precipitation that are not contaminated by RFI.

The above spectrogram analysis allows us to compare and assess the spectral polarimetric filters for RFI mitigation. In addition, PPI examination is necessary as depicted in Fig. 5.13 to examine a large number of rays. The SP filtered PPI retains the most precipitation but also clutter (e.g., narrow-band artifacts and RFI) and noise. As for the proposed SPFs, they have better clutter and noise suppression capability. The OBSpol filters as shown in Fig. 5.13(c) and (d) outperform the MDsLDR filter as demonstrated in Fig. 5.13(b) by keeping more weak precipitation, making the PPI display continuous and smooth. In this case, which is contaminated by many artifacts, the OBSpol filter

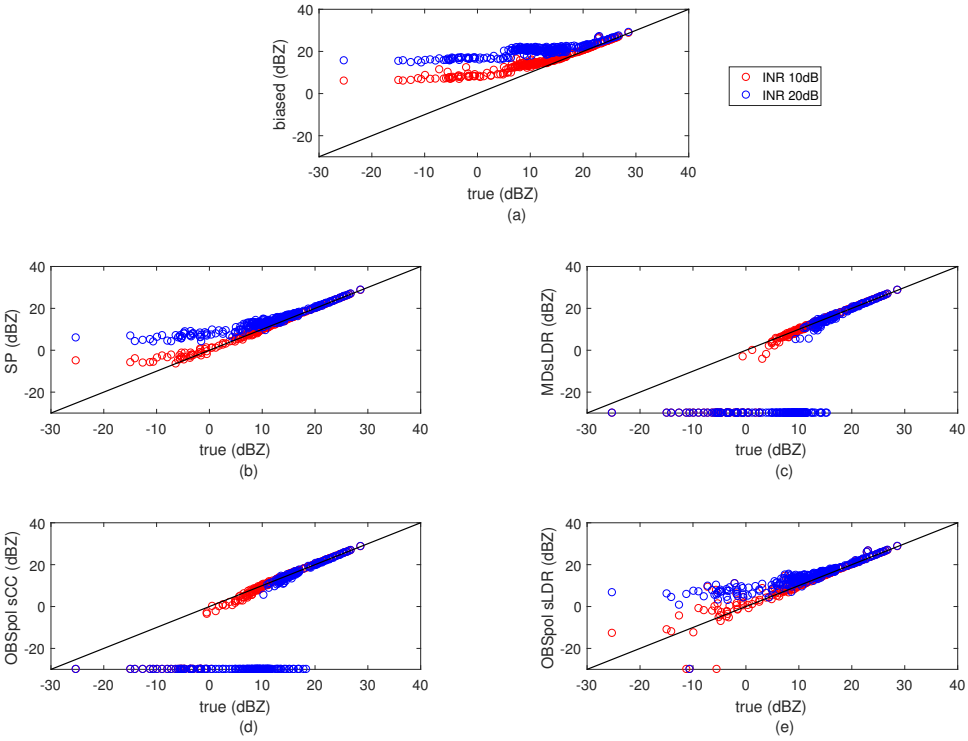

Figure 5.12: The scatter plots between the true reflectivity and the reflectivity obtained by different filtering techniques. Blue and red points are related to INR 10 dB and INR 20 dB, respectively. (a) RFI contaminaed; (b) the SP; (c) the MDsLDR filter; (d) the OBSpol filter with $s\rho_{co}$; (e) the OBSpol filter with $sLDR$.

with $s\rho_{co}$ and the MDsLDR filter cannot completely remove the artifacts. It takes 22.7 s to obtain the MDsLDR filtered PPI using Matlab 2016b in a windows 7 desktop PC with a 3.6 GHz Intel Xeon E5-1620 CPU and 16 GB RAM. The time elapsed for the OBSpol filter with $s\rho_{co}$ and with $sLDR$ is 36.4 s and 39.4 s, respectively. This time information indicates that the MDsLDR filter has slightly less computational complexity than the OBSpol filters. Nonetheless, all the SPFs have the potential to be operated in real-time with dedicated software.

In summary, with the spectrogram and PPI examination, the SPFs in AHV radar have good ability to remove RFI as well as narrow-band clutter (artifacts and ground clutter) and noise. For the inter-comparison, the OBSpol filters have better performance in weak precipitation preservation than the MDsLDR filter. Such capability, however, could be a shortcoming in the situation of high-intensity RFI contamination considering the quality of the polarimetric variables. Solving this problem for a specific application may lead to threshold changes for the spectral polarimetric variables. The advantage of using $sLDR$ measurements is that no notch filter is required for ground clutter mitigation.

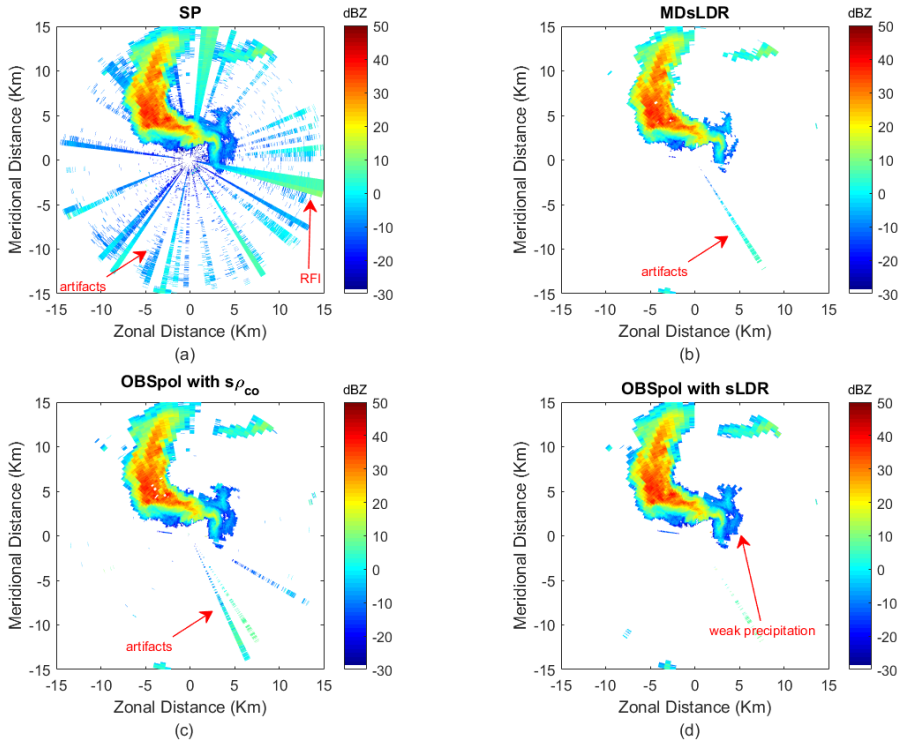

Figure 5.13: Reflectivity PPIs of IDRA with different filtering techniques. (a) the standard processing; (b) the MDsLDR filter; (c) the OBSpol filter with $s\rho_{co}$; (d) the OBSpol filter with $sLDR$.

5.5.2. APPLICATION TO SHV RADAR DATA

The IDRA data with simulated RFI show good performance of cross-polar measurements in clutter suppression. However, the cross-polar backscattering is not always available for most polarimetric weather radars. This part shows the RFI filtering results of the SHV radar, i.e., KNMI Herwijnen radar, which does not have $sLDR$ measurements. The filter applied is the OBSpol filter with $s\rho_{co}$. Specifically, $s\rho_{co}$ will be the SHV $s\rho_{co}$ and the AHV $s\rho_{co}$. The data considered are the same as in Fig. 5.8. The radar configuration for acquiring the data has been described in Section 5.2.1, and 64 samples of pulses are taken to generate the range-Doppler spectrogram.

First, the filter applied to the spectrograms is checked. Ray 70 is taken, and the original sP_{hh} spectrogram is displayed in Fig. 5.2(c) (in SHV mode) and Fig. 5.4(f) (in AHV mode). The corresponding filtered spectrograms using the OBSpol filter are shown in Fig. 5.14. Both filtered spectrograms can preserve precipitation, but the one with SHV $s\rho_{co}$ also retains more residual RFI, which is not the case of the one with AHV $s\rho_{co}$. When filtered spectrograms derived from both H_{2m-1} and V_{2m} and H_{2m} and V_{2m-1} are combined, which is equivalent to the full number of samples, precipitation without RFI con-

tamination can be obtained. Currently, the Doppler aliasing problem due to the selected half samples, is not solved yet. Thus, we will quantify the filtering performance in PPI in terms of power-related variables (e.g., reflectivity and differential reflectivity).

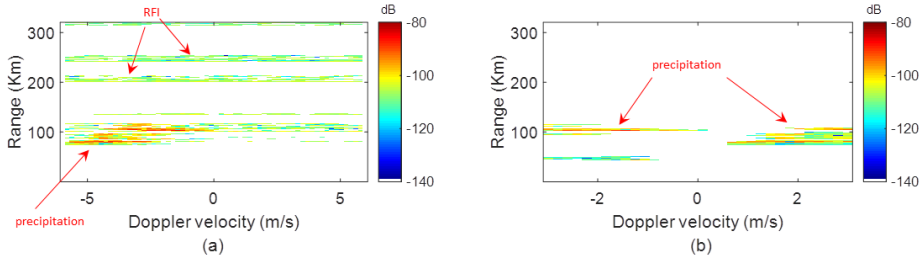

Figure 5.14: KNMI Herwijnen radar spectrogram comparison. (a) OBSpol filter with SHV $s\rho_{co}$; (b) OBSpol filter with AHV $s\rho_{co}$.

Considering another ray (Ray 160), the simulated RFI with INR 10 dB is added to the raw measurements. The raw spectrogram and the RFI contaminated one are shown in Fig. 5.15(a) and (b). Then, the OBSpol filter with SHV $s\rho_{co}$ and AHV $s\rho_{co}$ are implemented to the contaminated sP_{hh}, and their corresponding results are displayed in Fig. 5.15(c) and (d). Obviously, the filter with AHV $s\rho_{co}$ has better performance in RFI removal. Further, we calculate the $P_{hh} \cdot r^2$ values and compare with the true ones, and display the scatter plots in Fig. 5.15(e) and (f). Compared with the OBSpol filter with SHV $s\rho_{co}$, the one with AHV $s\rho_{co}$ can mitigate the RFI. In this case, the δZ_{hh} of the OBSpol filter with SHV $s\rho_{co}$ is 4.97 dBZ, while that of the OBSpol filter with AHV $s\rho_{co}$ is 0.71 dBZ.

The original and filtered PPIs of $P_{hh} \cdot r^2$ and Z_{dr} in both SHV and AHV modes are shown in Fig. 5.16. The simulated RFI is modeled as to be 45° polarized. As observed in Fig. 5.16(b), such a simulation has some deviation from the real measurements. However, as is discussed in Section 5.3.3, for RFI with arbitrary polarization (not strictly H or V) high values near 1 are expected in SHV mode, thus the deviation has no influence on the filter performance evaluation. Both filters can keep most of the precipitation and mitigate some RFI. Compared with the OBSpol filter with SHV $s\rho_{co}$, the filter with AHV $s\rho_{co}$ has better performance in RFI mitigation, real and simulated. In this case, the OBSpol filter with SHV $s\rho_{co}$ can mitigate all the RFI whose INR is less than 7 dB, namely the real RFI since the simulated one has an INR of 10 dB. While the one with AHV $s\rho_{co}$ can remove almost all the RFI. In addition, noise is mitigated in both filters. This spectral polarimetric filter can improve not only the observation (e.g., the weak precipitation at short range in Fig. 5.16(d) and (f) which is masked in the neighboring background in Fig. 5.16(b)), but also the radar observable quality (e.g., the precipitation overlapping with RFI in Fig. 5.16(b)). Using the same computational environment as described in Section 5.5.1, the processing time for Fig. 5.16(c) and (d) generation is 46.1 s, and that of Fig. 5.16(e) and (f) is 69.6 s. The time increase for the KNMI Herwijnen data is mainly because more rays need to be processed (227 rays compared with 143 rays in IDRA PPI). According to the time statistical analysis, Step 3 of the OBSpol filter is the most time consuming step. Additionally, implementing the AHV mode processing twice requires

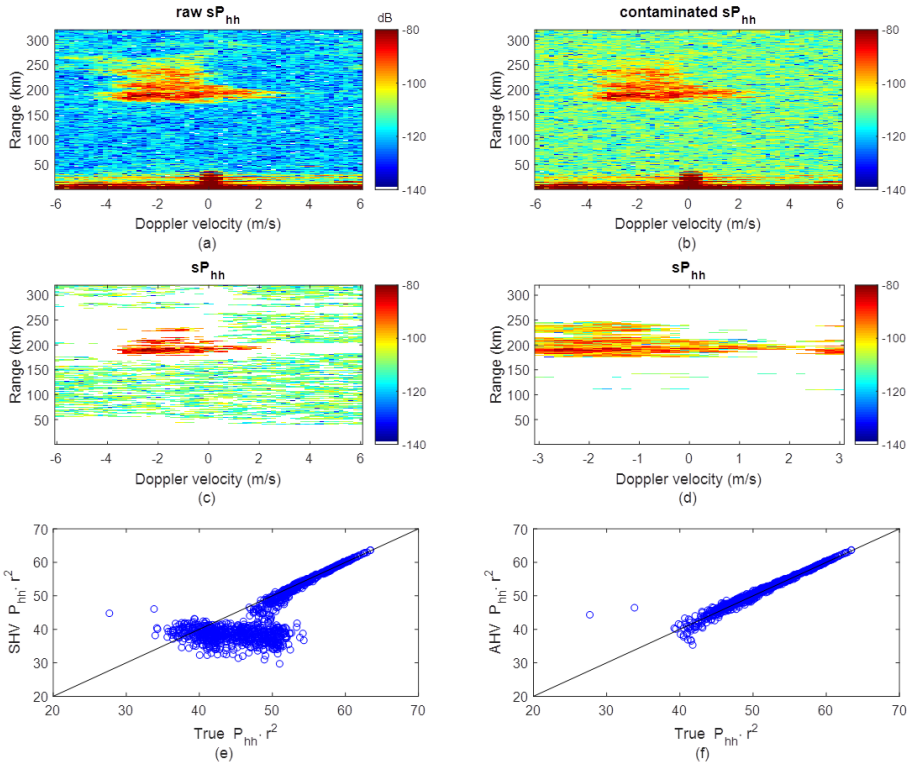

Figure 5.15: Performance comparison between the SHV $s\rho_{co}$ and the AHV $s\rho_{co}$ used in the OBSpol filter. (a) raw spectrogram; (b) spectrogram with INR 10 dB; (c) spectrogram filtered by the OBSpol with SHV $s\rho_{co}$; (d) spectrogram filtered by the OBSpol with AHV $s\rho_{co}$; (e) scatter plot between the true $P_{hh} \cdot r^2$ and the SHV $P_{hh} \cdot r^2$; (f) scatter plot between the true $P_{hh} \cdot r^2$ and the AHV $P_{hh} \cdot r^2$.

more time than that of the SHV mode processing once. However, with dedicated software and algorithm optimization, it may be possible to operate the adopted technique in real-time.

5.6. CONCLUSION

Radio frequency interference (RFI) has become a growing concern for weather radar. Aiming at mitigating RFI for polarimetric weather radar, spectral polarimetric filters (SPFs) are proposed in this paper. In this research, the real RFI measurements from an operational C-band weather radar, KNMI Herwijnen radar, are used to characterize the RFI spectral and polarimetric features. On one hand, RFI in polarimetric radar can be regarded as white noise in the spectral domain for each channel (also applied to single polarization radar). On the other hand, considering the correlation between two channels, different polarimetric radar types have different impacts. For SHV radar, the RFI sensed by the horizontal and vertical channels will be the same and correlated. While for AHV radar, RFI detected by the two consecutive channels will be independent.

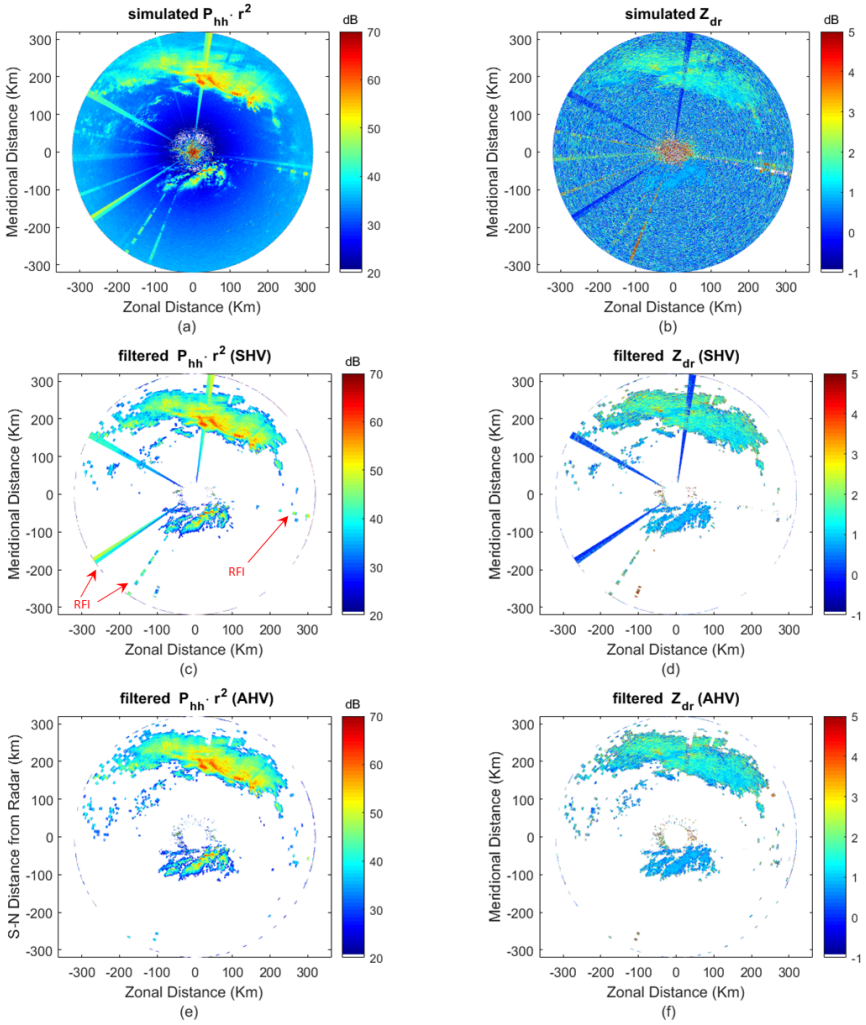

Figure 5.16: KNMI Herwijnen radar PPIs comparison. (a) raw $P_{hh} \cdot r^2$; (b) raw Z_{dr}; (c) filtered $P_{hh} \cdot r^2$ by using OBSpol with SHV $s\rho_{co}$; (d) filtered Z_{dr} by using OBSpol with SHV $s\rho_{co}$; (e) filtered $P_{hh} \cdot r^2$ by using OBSpol with AHV $s\rho_{co}$; (f) filtered Z_{dr} by using OBSpol with AHV $s\rho_{co}$.

Based on these features, the RFI is simulated in a full-polarimetric X-band radar, IDRA, to quantify the performances of SPFs. These SPFs are multi-functional for mitigating different types of clutter. Specifically, initially designed for removing narrow-band clutter (i.e., moving artifacts and ground clutter) and noise, the MDsLDR filter and the OBSpol filter are analyzed for the application of RFI mitigation. Based on the spectral polarimetric features and range-Doppler continuity of precipitation, the filters generate a filtering mask implemented on the raw range-Doppler spectrogram to retain the precipitation and remove the clutter.

Overall, both the OBSpol filters and the MDsLDR filter suppress clutter similarly well, while the OBSpol filters better preserve weak precipitation. The reason is that OBSpol filters have more advanced signal processing, which separates precipitation and clutter in different objects. For radar systems with full-polarimetric ability, all the SPFs can be used. The MDsLDR filter has less computational complexity than the OBSpol version. For polarimetric weather radar without cross-polar measurements, the OBSpol filter with $s\rho_{co}$ (combined with the notch filter around 0 m/s or another ground clutter mitigation technique in Step 1) is recommended. However, due to the high correlation between HH and VV measurements in SHV radar, generation of the AHV $s\rho_{co}$ as a replacement of SHV $s\rho_{co}$ is suggested for the filter design in RFI mitigation. The Doppler dealiasing technique (Unal and Moisseev, 2004) specific for the AHV mode, which allows the recovery of the SHV maximum unambiguous Doppler velocity, should be implemented next.

Both the MDsLDR filter and the OBSpol filters have the potential to be operated in real-time, and they are also applicable with different Doppler velocity resolutions (Yin *et al.*, 2017b, 2019). It is worth mentioning that the OBSpol filter has been applied to an operational C-band radar with pulse number 64 in this work, and good clutter mitigation performance is achieved. These properties are attractive for operational weather radar. However, the proposed SPFs cannot resolve the problem when clutter is embedded into the precipitation. For example, when precipitation and ground clutter overlap, it will result in some suppression of precipitation located at around 0 m s^{-1} in the range-Doppler spectrogram; this problem should be a focus of future research.

6

UAV-AIDED WEATHER RADAR CALIBRATION

This chapter has been submitted as:

Jiapeng Yin, Peter Hoogeboom, Christine Unal, Herman Russchenberg, Fred van der Zwan, Erik Oudejans. "UAV-aided Weather Radar Calibration.", *IEEE Trans. Geosci. Remote Sens.*, Under review.

From Chapter 2 to Chapter 5, the clutter mitigation methods are discussed, with which we are expecting to obtain "clean" precipitation measurements. However, for weather radar applications, it is also important to quantitatively get the "correct" precipitation estimation. The novel radar calibration technique presented in this chapter is for the purpose. The UAV-aided radar calibration technique is a general method which can adapt to different radar systems.

Except the introduction is given in Section 6.1, the reminder of this chapter is organized as follows. In Section 6.2, the basic principles including weather radar equation, calibration configuration and sphere positioning are introduced. The calibration measurements and their analysis are provided in Section 6.3, in which the UAV flying mode and radar measurements, antenna pointing calibration, along with antenna pattern fit and radar constant calculation are discussed. Some conclusions are drawn in Section 6.4.

6.1. INTRODUCTION

Weather radar is well recognized as an indispensable tool for atmospheric observation because it obtains the information of atmospheric phenomena at a large scale within a

short time (Bringi and Chandrasekar, 2001). According to different atmospheric applications, various types of radars in different configurations and platforms can be used. The key to using weather radar data is the sufficient measurement accuracy. However, radar system bias can be introduced from any radar component, which adds to the inestimable uncertainty in radar measurements. This system bias should be quantified through the process of "radar calibration" which aims to identify the unknown system error caused by the transmitter, receiver and antenna by using some standard objects (Richards *et al.*, 2010). The system errors can be estimated by inserting the test signal into the radar system or by using objects with known scattering property. The radar calibration can be divided into two parts: the internal calibration and the external calibration.

For the internal calibration, built-in test equipment is installed to act as the internal radar calibration loop to monitor the variability of the electronic components inside the radar system. However, since the radar system has many discrete components it is difficult to characterize every component. Internal calibration can help to measure the calibration drifts over time. These drifts are caused by the gradual degradation of the system performance (e.g., gain, loss in the transmitter and receiver), but not including the antenna (e.g., radome changes) (Anagnostou *et al.*, 2001). Hence, it may be more practical to evaluate and characterize the radar system as a whole using the external calibration. As for the internal calibration, it can be used to monitor the stability of the transmitter and receiver.

The external calibration, always regarded as end-to-end calibration, involves the measurement of backscattering of a calibrator with known radar cross section (RCS), such as a trihedral or metal sphere. To characterize the radar system error, external calibration which covers the full path of the transmitter, receiver and antenna is necessary. The current external calibration technique is mainly using a tethered balloon hanging metal sphere (Williams *et al.*, 2013) or trihedral locating on the top of a tower or mast (Bharadwaj *et al.*, 2013). However, there are some shortcomings with these methods. First of all, these methods are limited due to location. When conducting the external calibration, the calibrator needs to be positioned in the far-field, which seems impossible for some radars located at the top of high buildings or towers. Secondly, it is expensive to setup a tower or purchase a helium balloon. Thirdly, it is not easy to repeat the calibration process due to the inconvenience of the calibration equipment transportation. Also, for vertically pointing cloud radar or other radar with mechanical constraints, these calibration methods cannot be applied. Hence, it is urgent to find a portable, cost-effective and repeatable solution that replaces or complements the current methods.

Aiming at solving the mentioned problems, a novel calibration method using an unmanned aerial vehicle (UAV) as the platform to carry a metal sphere is proposed to act as an alternative to achieve the external radar calibration. This idea was intially proposed during the Aerosol, Clouds, and Trace gases (ACTRIS) workshop held in Cologne, Germany in 2015, in which the current and planned calibration methods as well as radar calibration phase classification were discussed (Russchenberg and Yin, 2015). Inspired by the workshop, a UAV-based external calibration technique was proposed to calibrate a dual intermediate-frequency frequency-modulation continuous-wave (FMCW) radar (Suh *et al.*, 2017). This Ku-band radar was developed to detect targets with small RCS

(e.g., drone). However, the antenna pointing calibration has not been done and the influence of antenna pattern was not fully discussed. Duthoit *et al.* (2017) introduced the operation and scanning modes for antenna characterization and radar calibration, focusing more on the concept description. However, the quantitative results were not provided.

In this work, the radar calibration technique is specifically designed for weather radar by considering the antenna pointing calibration, antenna pattern retrieval and calibration error quantification. Compared with other types of radar, weather radar aims to measure volume distributed targets (i.e., precipitation) where quantitative backscattering measurements of hydrometers are required. Thus, antenna pointing calibration is important because the location of the measured resolution volume of which backscattering is estimated should be known. The antenna pattern retrieval is also necessary for accurate quantification due to the fact that the radar constant of weather radar is related to the antenna pattern integration. Finally, the robustness of the proposed technique can be proved through the calibration error quantification.

6.2. BASIC PRINCIPLES

6.2.1. WEATHER RADAR EQUATION

Weather radar is designed to sample distributed targets such as precipitation and its range equation is (Bringi and Chandrasekar, 2001)

$$P_r(R) = \left[\frac{P_t G_0^2 \rho}{\lambda^2 (4\pi)^3}\right] \left(\int\int f^2(\theta,\phi)\, d\Omega\right) \frac{\pi^5 |K_w|^2 Z(R)}{R^2} \cdot \frac{1}{L} \cdot 10^{-18} \tag{6.1}$$

where $P_r(R)$ is the received power in range R, P_t is the transmitter power, G_0 is the peak boresight gain of the antenna, ρ is the range resolution, λ is the radar wavelength, $f(\theta,\phi)$ is the normalized antenna pattern function versus azimuth and elevation angles (θ,ϕ), $|K_w|^2$ is the dielectric factor of water and $Z(R)$ is the equivalent reflectivity factor in range R. L is the total loss of the radar system.

Eq. (6.1) can also be reformulated as

$$Z(R) = C \cdot P_r \cdot R^2 \tag{6.2}$$

where C is the radar constant, expressed as

$$C = \frac{\lambda^2}{\pi^5 |K_w|^2} \left[\frac{(4\pi)^3}{P_t G_0^2 \rho}\right] \left(\frac{1}{\int\int f^2(\theta,\phi)\, d\Omega}\right) \cdot L \cdot 10^{18} \tag{6.3}$$

For radar calibration, the estimation of the radar constant C can be obtained by measuring P_r and R corresponding to a calibrator whose Z is known. Usually, the calibrator will be chosen as a metal sphere for the reason that its RCS is kept constant for different incidence angles. A sphere, however, is a point target rather than a distributed target, and the equivalent RCS of a sphere treated as a distributed target will be derived next. The total loss L in Eq. (6.3) includes all the hardware and processing loss. The hardware loss can be quantified by inspecting each radar component, however, the processing loss is difficult to estimate. This research proposes a technique to calculate the radar constant

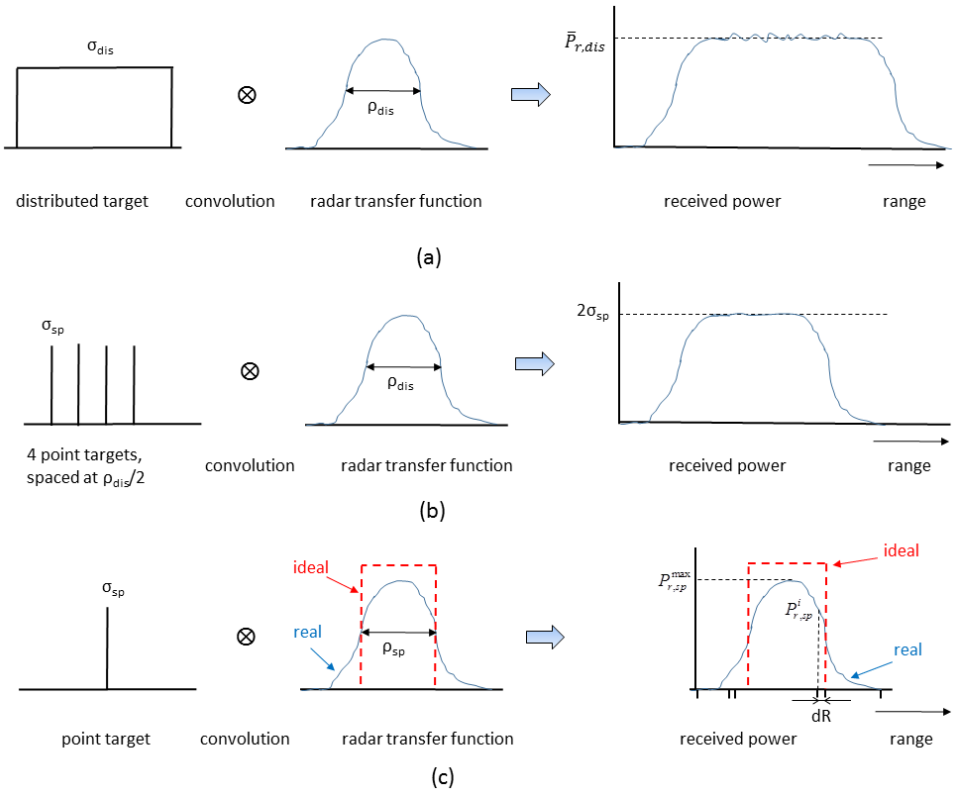

Figure 6.1: Radar response of distributed target and point target. (a) a distribute target; (b) several point targets mimic a distributed target; (c) a point target.

without estimating the total loss. However, the impact of the range resolution on the total loss L will be investigated. The reason is that the radar is calibrated using a higher range resolution (e.g., 3 m) than the operational one (e.g., 30 m) since the higher range resolution is required in practical calibration experiments. The radar constant estimated in a higher range resolution can be used for radar configured in other range resolutions with proper adjustment. The loss L may vary due to different range resolutions.

In the case of a distributed target, as is shown in Fig. 6.1(a), the average received power $\bar{P}_{r,dis}$ can be expressed as

$$\bar{P}_{r,dis} = \frac{P_t G_0^2 \lambda^2}{(4\pi)^3 R_{dis}^2} \cdot \frac{\sigma_{dis} \rho_{dis}}{L_{dis}} \left(\int\int f^2(\theta,\phi)\, d\Omega \right) \tag{6.4}$$

where R_{dis} is the range of the distributed target, σ_{dis} is the backscatter cross section per unit volume ($m^2 m^{-3}$) of the distributed target, ρ_{dis} is the range resolution, L_{dis} is the total loss of radar system in this case.

The correctness of Eq. (6.4) can be verified if the distributed target is replaced by several point targets which for instance are separated by $\rho_{dis}/2$, as shown in Fig. 6.1(b).

In this case, 3 point targets with RCS σ_{sp} contribute to the received power after the convolution with the radar transfer function. Their powers are summed, and the received power is approximately 2 times as large as a single point target. Specifically, in such situation, the equivalent σ_{dis} of a distributed target is related to $2\sigma_{sp}/\rho_{dis}$, which means when using point targets for weather radar calibration, the range resolution should be known.

Furthermore, if only one point target (i.e., one sphere) is considered, as illustrated in Fig. 6.1(c), the conventional radar equation of point target, referred to as the peak response, is defined as

$$P_{r,sp}^{max} = \frac{P_t G_0^2 \lambda^2 \sigma_{sp}}{(4\pi)^3 R_{sp}^4} \cdot \frac{1}{L_{sp}} \tag{6.5}$$

where $P_{r,sp}^{max}$ is the peak power, σ_{sp} is the RCS of the sphere, R_{sp} is the range of the sphere, and L_{sp} is the total loss of radar system in this case. The estimation of the range resolution ρ_{sp} is problematic because of the non-ideal condition of radar receiver bandwidth. As is shown in Fig. 6.1(c), the real radar transfer function deviates from the ideal one, making the measured peak power $P_{r,sp}^{max}$ deviate from the ideal peak power and such deviation cannot be quantified.

In addition, for a FMCW radar, the range information is obtained by the Fourier transform of the beat signal. When the target is moving during the measurements, the Fourier transform leakage leads to energy distributing in neighboring range gates. Therefore, the measured peak power method will underestimate the backscattering of the sphere.

To alleviate the problem of non-ideal radar transfer function and the Fourier transform leakage in FMCW radar, the integrated response is considered. Specifically, following the energy conservation theorem, for any actual range resolution ρ_{sp}, the integrated power $P_{r,sp}^{I}$ can be expressed as

$$P_{r,sp}^{I} = \int_0^{\infty} P_{r,sp}(R)\, dR = \frac{P_t G_0^2 \lambda^2 \sigma_{sp}}{(4\pi)^3 R_{sp}^4} \cdot \frac{\rho_{sp}}{L_{sp}} \tag{6.6}$$

where $P_{r,sp}(R)$ is the received power in function of different ranges. The integral form in Eq. (6.6) can be approximated by the numerical form as

$$P_{r,sp}^{I} = \sum_i P_{r,sp}^{i} \Delta R \tag{6.7}$$

where $P_{r,sp}^{i}$ is the i^{th} received power sampled by the sampling distance ΔR (i.e., the specified range resolution). Thus, the integrated power instead of the peak power is recommended in the weather radar constant calculation.

It is also worth noting that the angular dependency of the term $P_{r,sp}^{I} R_{sp}^4$ is related to the two-way antenna gain. Therefore, this term will be used afterwards to represent the two-way antenna gain. Combining Eq. (6.3) with Eq. (6.6), we obtain the radar constant C^I (the superscript I relates to the integrated antenna pattern):

$$C^I = \frac{\lambda^4}{\pi^5 |K_w|^2} \left[\frac{\sigma_{sp}}{P_{r,sp}^{I} R_{sp}^4} \right] \frac{L \rho_{sp}}{L_{sp} \rho} \left(\frac{1}{\int\int f^2(\theta,\phi)\, d\Omega} \right) 10^{18} \tag{6.8}$$

Hereby we define the loss-over-range-resolution ratio as

$$r_{L\rho} = \frac{L\rho_{sp}}{L_{sp}\rho} \tag{6.9}$$

Then Eq. (6.8) can be expressed as

$$C^I = \frac{\lambda^4}{\pi^5 |K_w|^2} \left[\frac{\sigma_{sp}}{P^I_{r,sp} R^4_{sp}} \right] r_{L\rho} \left(\frac{1}{\int\int f^2(\theta,\phi)\, d\Omega} \right) 10^{18} \tag{6.10}$$

The value of $r_{L\rho}$ equals to 1 when the same range resolution is used for calibration and atmospheric measurements. Otherwise, the value of $r_{L\rho}$ can be quantified by the measurements of a distributed target (i.e., precipitation) at the same range R but with the range resolution setting ρ and ρ_{sp}, and the corresponding received powers are

$$\bar{P}_{r,\rho} = \frac{P_t G_0^2 \lambda^2}{(4\pi)^3 R^2} \cdot \frac{\sigma_{dis}\rho}{L} \left(\int\int f^2(\theta,\phi)\, d\Omega \right) \tag{6.11}$$

$$\bar{P}_{r,\rho_{sp}} = \frac{P_t G_0^2 \lambda^2}{(4\pi)^3 R^2} \cdot \frac{\sigma_{dis}\rho_{sp}}{L_{sp}} \left(\int\int f^2(\theta,\phi)\, d\Omega \right) \tag{6.12}$$

where σ_{dis} is the backscatter cross section per unit volume ($m^2 m^{-3}$) of precipitation (the precipitation is assumed to be homogeneous in the measurement period). Combining Eq. (6.11) and (6.12), the loss-over-range-resolution ratio can be estimated by

$$r_{L\rho} = \frac{\bar{P}_{r,\rho_{sp}}}{\bar{P}_{r,\rho}} \tag{6.13}$$

When the assumption is made that the antenna pattern can be approximated by a Gaussian function (Bringi and Chandrasekar, 2001), the radar constant is expressed as C^A (the superscript A relates to the approximated antenna pattern)

$$C^A = \frac{\lambda^4}{\pi^5 |K_w|^2} \left[\frac{\sigma_{sp}}{P^I_{r,sp} R^4_{sp}} \right] r_{L\rho} \left(\frac{8ln2}{\pi\theta_1\phi_1} \right) 10^{18} \tag{6.14}$$

where θ_1 and ϕ_1 are the 3 dB beam widths. Hereby the antenna constant A is defined, which represents the contribution of the antenna in the radar constant calculation, and corresponding to Eq. (6.10) and Eq. (6.14), we have

$$A^I = 1/\int\int f^2(\theta,\phi)\, d\Omega \tag{6.15}$$

$$A^A = 8ln2/\pi\theta_1\phi_1 \tag{6.16}$$

The antenna constant and radar constant are calculated based on field measurements. In this research, two different measurements, namely from UAV and transponder, are used to calculate the corresponding values. For the terminology with respect to antenna constant and radar constant, we will have A^x_y and C^x_y, where x being I or A (the integrated

or approximated antenna pattern) and y being UAV or ref (the measurements are from the UAV or the transponder aided calibration experiments). The antenna beam pattern measurements using a transponder (Aubry and Zijderveld, 1999) can be considered as a reference to evaluate the performance of the proposed UAV-aided radar calibration technique.

In addition, radar calibration is used to identify the uncertainty in the radar constant, and in this work, C^I is the target radar constant, whose uncertainty is expressed as

$$\frac{\delta C^I}{C^I} = \sqrt{\left(\frac{\delta \sigma_{sp}}{\sigma_{sp}}\right)^2 + \left(\frac{\delta P^I_{r,sp}}{P^I_{r,sp}}\right)^2 + 16 \cdot \left(\frac{\delta R_{sp}}{R_{sp}}\right)^2 + \left(\frac{\delta A^I}{A^I}\right)^2 + \left(\frac{\delta r_{L\rho}}{r_{L\rho}}\right)^2} \tag{6.17}$$

where $\delta X / X$ means the relative error of variable X. Note that the terms in Eq. (6.17) are all in linear scale. Combined with radar measurements, more details will be provided in Section 6.4.2.

Since the radar constant shown in Eq. (6.10) is related to a specific volume, it is necessary to know where the volume locates, which is the antenna pointing accuracy. This can be done by either fixing the antenna pointing to one direction and making the calibrator (e.g., metal sphere) move along the elevation or azimuth angle axis, or fixing the calibrator and scanning the radar antenna along the elevation or azimuth angle direction. Due to the mechanical limitation of the radar used, the former is selected in this work. Considering the azimuth angle of the radar antenna pointing as an example, when the calibrator moves continuously from sidelobe to mainlobe and then to sidelobe of antenna pattern in different elevation angles, the measured $P^I_{r,sp} R^4_{sp}$ term will approximate the antenna pattern. It is expected that when all the peaks of $P^I_{r,sp} R^4_{sp}$ are chosen and outputting their azimuth and elevation angles in the azimuth-elevation plane, they tend to have the same azimuth angle but different elevation angles. The averaged azimuth angle deviating from 0° is regarded as the azimuth offset. Similar work can be done to estimate the elevation angle of the antenna pointing.

When the antenna pointing calibration is done, the $P^I_{r,sp} R^4_{sp}$ values measured in different elevation and azimuth angles are used to interpolate the antenna pattern. With the retrieved antenna pattern, the antenna constant in Eq. (6.15) can be obtained. It is expected that the radar constant C^I based on the antenna integration is more accurate than the conventional one (i.e., the approximated C^A) and the reasons are twofold. One is that C^I is based on real measurements and C^A relies on a model-based approximation. The other reason is that enough measurements are used in C^I to eliminate some random variations. More results are given in Section 6.4.2 to support such statement.

6.2.2. CALIBRATION CONFIGURATION

In Cabauw Experimental Site for Atmospheric Research (CESAR) Observatory, the Netherlands, there are two FMCW radars, one S-band Transportable Atmospheric Radar (TARA) and one X-band IRCTR Drizzle Radar (IDRA) (Yin *et al.*, 2017b). The two radars were designed by the Delft University of Technology for atmospheric research, and their measurements are displayed online in real-time. The data provide a long-term observation to monitor the trends of precipitation changes. Particularly, TARA is considered in the calibration campaign, and its specifications are shown in Table 6.1. In addition, the bore-

sight cut of the antenna beam pattern of TARA along the azimuth direction measured by a radar transponder (Aubry and Zijderveld, 1999) is shown in Fig. 6.2. This is the one-way antenna pattern. A similar pattern is obtained along the elevation axis. Therefore, $\theta_1 \approx \phi_1$ for TARA and estimated to be 2.1°, which will be used in Eq. (6.16) to calculate the antenna constant. The transponder-aided radar calibration experiment took place after TARA was built in 1999.

Table 6.1: S-band radar TARA specifications.

Radar	TARA
Type	FMCW radar (solid state)
Frequency	3.298 GHz
Transmit power	100 W
Antenna diameter	3 m (parabolic)
Beam width	2.1°
1^{st} side lobe	-20 dB
Polarization	HH/HV/VV
pulse repetition frequency	2 KHz
Bandwidth	2 - 50 MHz
Antenna rotation	Elevation 0°- 90°, Azimuth fixed

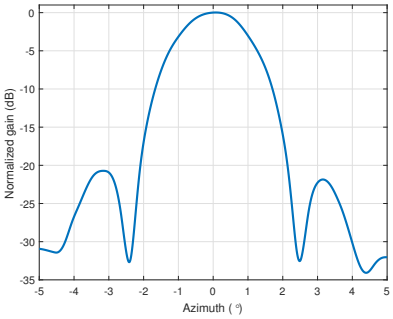

Figure 6.2: TARA antenna beam pattern obtained by a radar transponder.

During the radar calibration campaign, a UAV named DJI Matrice 600 serves as the stable aerial platform carrying a metal sphere, flying over the radar illumination areas to complete the calibration process. The UAV is displayed in Fig. 6.3(a) where the UAV is placed on the ground next to a metal sphere, and the specifications of the UAV are shown in Table 6.2. This is a powerful UAV with a maximum payload of 6 kg. The UAV should fly at small speed to guarantee the data quality for TARA Doppler processing, and we choose the minimum flying velocity (1 m s^{-1}). In addition, there is GPS on board and the positioning accuracy is in meter, which fulfills the requirement for radar ranging. GPS information in the UAV can be used to calculate the distance between the sphere and radar R_{sp} when the connecting line between the UAV and sphere is short enough. How-

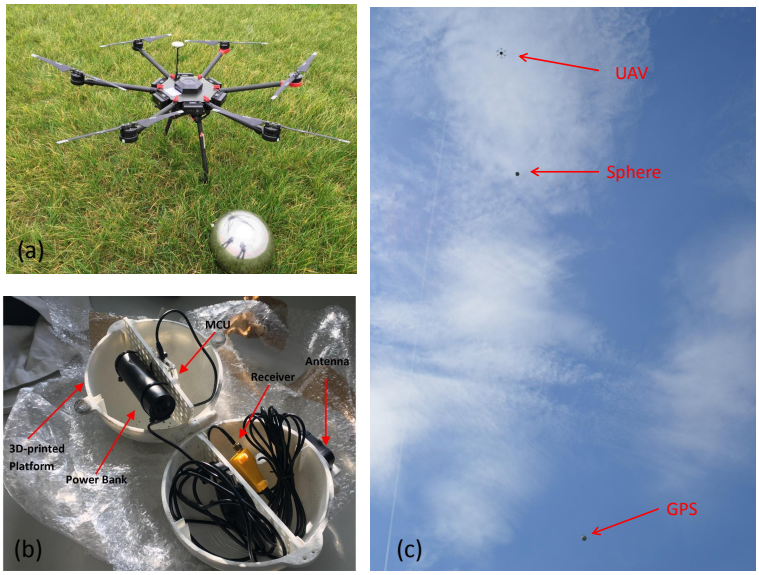

Figure 6.3: The calibration hardware and setup. (a) UAV DJI Matrice 600 and the metal sphere; (b) external GPS box; (c) scene of UAV, sphere and external GPS box.

Table 6.2: UAV specifications.

MATRICE 600	Manufacturer: DJI, China
Type	Micro-drone hexacopter
Dimension	Diameter 167 cm, height 62 cm
Weight	9.1 kg with batteries
Payload	Max 6 kg
Flight mode	Automatic with waypoint or based on radio control
Hovering Accuracy	P-Mode: Vertical ± 0.5 m, Horizontal ± 1.5 m
Max Speed	18 m/s (No wind)
Endurance	No payload: 35 min, 6 kg payload: 16 min

ever, to avoid the backscattering of UAV contaminating that of the sphere in the radar measurements, the connecting line should be long enough to separate the UAV from the sphere in different range bins. In this case, an external GPS box which is located underneath the sphere is required. The connecting line between the UAV and the sphere and that between the sphere and the external GPS device is set to the same. Thus, the coordinates of the sphere can be retrieved with the coordinate outputs of GPS on UAV and external GPS box. The details of the external GPS device will be given later. Sometimes, due to the influence of wind, UAV, sphere and external GPS may not be one line, which results in sphere positioning errors. Therefore, the calibration campaign requires quiet meteorological conditions: weak wind and no precipitation.

The UAV-aided radar calibration diagram is shown in Fig. 6.4. The calibration campaign is now conducted in the high-resolution mode instead of operational mode (i.e., 30 m). During the experiment, TARA was configured with the elevation angle 12°, bandwidth 50 MHz corresponding to the range resolution 3 m, and the connecting line length was 50 m. The connecting line between the UAV and the sphere was a fishing line which is light and firm. Such configuration mainly results from the legal UAV flying height in the Netherlands (i.e., 120 m). It guarantees a clear range separation between the backscattering of the UAV, sphere and GPS box. With proper flying routine design, the sphere can only be placed in the antenna main beam while UAV and external GPS device are outside of the main beam. The scene of the calibration is shown in Fig. 6.3(c), where UAV, metal sphere and GPS box are visible from top to bottom in the sky.

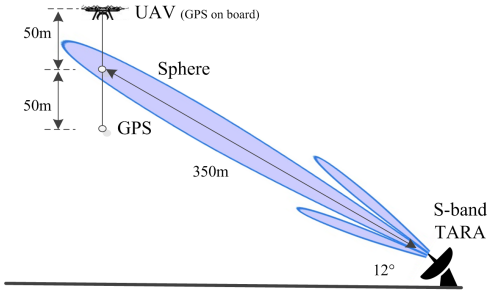

Figure 6.4: Schematic diagram of UAV-aided radar calibration technique.

6.2.3. SPHERE POSITIONING

The range R_{sp} can be obtained through various Global Navigation Satellite System (GNSS) processing techniques. Some of the most precise positioning techniques consist of differential GNSS solutions. For differential solutions, the spatial stability of major GNSS signal delay sources, such as the troposphere and ionosphere, are necessary. For this assumption to hold, we are dependent on a moderate to short baseline. Introducing such a baseline dependency means that the user would either need to operate their own base station or use a nearby permanent GNSS station, for instance, those linked to the IGS GNSS network. This is not always the most practical solution, especially for the calibration of mobile radar systems. Therefore, we adapted the real-time single frequency precise point positioning (RTSFPPP) algorithm developed at the Mathematical Geodesy and Positioning group at the Delft University of Technology (de Bakker and Tiberius, 2017). Instead of making use of a base station, we rely on a broad network of permanent stations through which we obtain predicted satellite orbits, predicted global ionospheric maps, and real-time satellite clock corrections. We expect a position standard deviation of 0.15 m in the horizontal direction and 0.30 m in the vertical direction. Although RTSFPPP can be used in real-time, in the light of this research post-processing is used.

The hardware of the external GPS box is displayed in Figure. 6.3(b), and the details of each component are shown in Table 6.3. All the components can be placed in the GNSS platform which is a custom 3D printed sphere. Our objective is to obtain a location invariant calibration method. Therefore, we make sure that everyone can obtain

Table 6.3: GNSS positioning hardware

Part	Specification
MCU	Raspberry Pi 2
Power	Anker powercore 1500 mAh
Receiver	Ublox M8T
Receiver case	Custom 3D-printed
Antenna	Taoglass Magma X 171
Platform	Custom 3D-printed

our GNSS platform, that the positioning is base-line independent and the UAV software works off-line. In the future, all 3D designs will be available online, and anyone who has the hardware at hand can be self-sufficient by using a 3D printer.

6.3. CALIBRATION MEASUREMENTS AND ANALYSIS

6.3.1. UAV FLYING MODE AND RADAR MEASUREMENTS

A proper flight mode is designed to measure the antenna beam pattern. Since the flying routine of the UAV can be programmed in advance according to the input of the GPS coordinates, which is referred to the waypoint operational mode, the horizontal and vertical zig-zag flying modes can be designed in the calibration campaign. The example of a horizontal zig-zag movement is shown in Fig. 6.5. The UAV starts at the home position where TARA locates, and flies to the far field conducting the horizontal movement in the plane perpendicular to the antenna pointing direction. Each time the UAV reaches the programmed end left or right position, it will go down or go up several meters. The enlarged flight mode with the horizontal zig-zag movement is visible in Fig. 6.5(b). For each horizontal flight routine in Fig. 6.5, the sphere moves with a fixed elevation angle and continuously changeable azimuth angles. With the completion of such movement, it is expected that if the antenna pattern can be approximated by the Gaussian function, the $P^I_{r,sp}R^4_{sp}$ term will also have a Gaussian shape because it relates to the antenna gain in different angles. Similarly, the vertical zig-zag movements will generate several cuts along the elevation angles with a fixed azimuth angle. With the measured elevation, azimuth angles as well as the $P^I_{r,sp}R^4_{sp}$ values, proper antenna pattern fitting methods can be used to obtain the 3-dimension antenna normalized gain, which will be discussed in Section 6.3.3.

To better characterize the radar measurements, the measured signal is inspected in both time domain and frequency domain, as shown in Fig. 6.6. In addition, the GPS output of UAV (blue line), sphere (black line) and GPS box (red line) are displayed in these figures. The data discussed here are from the case with a vertical zig-zag movement on March 6, 2018. Firstly, when the measurements are observed in the time domain as displayed in Fig. 6.6(a), the movements of UAV, sphere and GPS box are visible. Fig. 6.6(a) shows a good match of the range information between the radar-measured and GPS-measured ones, sharing the same movement pattern but some range deviation. In this case, the mean and standard deviation of the sphere absolute range difference between

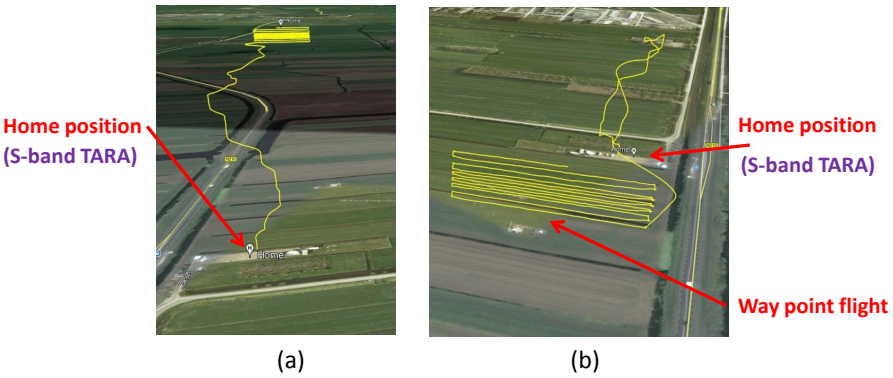

Figure 6.5: Horizontal zig-zag movement of the UAV.

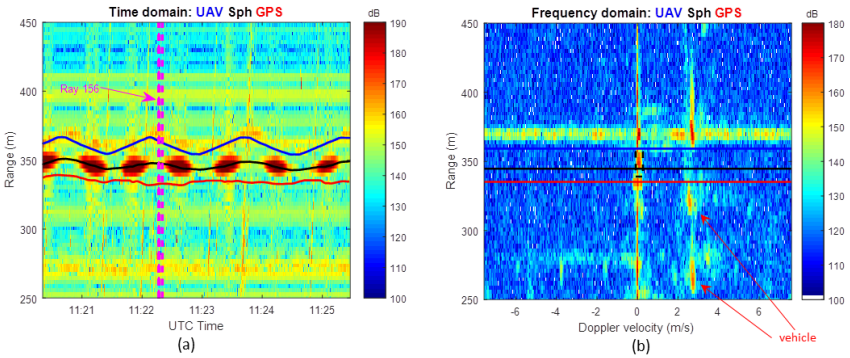

Figure 6.6: Radar and GPS measurements of UAV, sphere and GPS box. (a) range-time image; (b) range-Doppler spectrogram of Ray 156.

the GPS-retrieved and the radar-measured ranges are 2.2 m and 3.9 m, respectively.

Furthermore, some of the data are visualized in the frequency domain which is obtained by taking 512 time samples in Fig. 6.6(a) and applying the Fourier transform at fixed range. Specifically, range-Doppler spectrogram of Ray 156 is considered. As shown in Fig. 6.6(b), the top signature represents the echoes from the UAV, which is consistent with the rotating blades of the UAV. In this case, the position of the sphere is indicated by a black line and the backscattering of the sphere centers around 0 m/s. Moreover, we can see the echoes from the GPS box in the bottom of Fig. 6.6(b), indicated by the red line. The separation in range of the UAV, sphere and GPS box is sufficient, otherwise, the estimation of the backscattering from the sphere would be biased. The estimation of the backscattered power of the sphere is by taking one rectangular window in the spectral domain to integrate the entire sphere signature. Recall the statement in Section 6.2.1, the integrated power is used to compensate the influence of the non-ideal radar transfer function and the Fourier transform leakage. Estimating the backscattered power of the sphere in the range-Doppler domain helps to eliminate the contamination from clut-

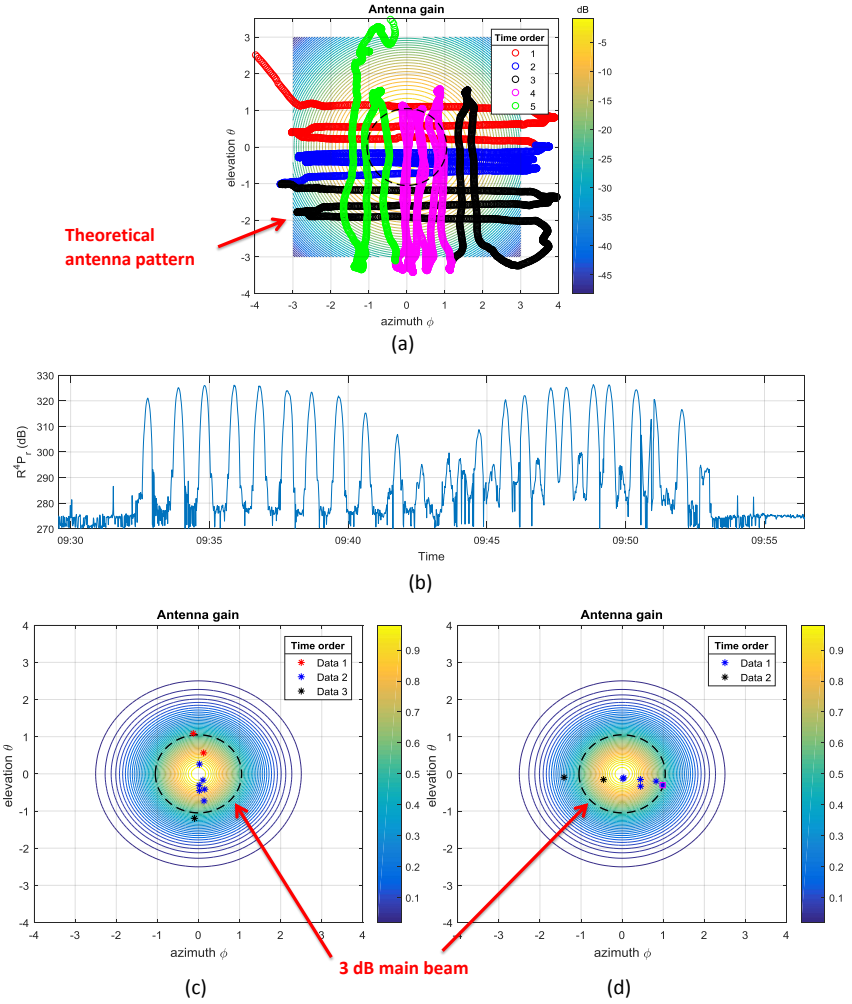

Figure 6.7: GPS output and radar measurements of the sphere. (a) azimuth and elevation angles; (b) $P^I_{r,sp}R^4_{sp}$ values; (c) angles of $P^I_{r,sp}R^4_{sp}$ peak values of the horizontal movement; (d) angles of $P^I_{r,sp}R^4_{sp}$ peak values of the vertical movement.

ter, such as vehicle echoes as shown in Fig. 6.6(b). In addition, only the data related to the sphere which are not contaminated by the ground clutter are selected for the radar constant calculation. In practice, before the launch of the UAV, radar measurements of the environment are collected to quantify the clutter. These clutter measurements lead to the selection of the range of about 350 m. In the case of the TARA calibration, the signal to clutter ratio varies from 20 dB to 50 dB. The ground clutter contamination is not so severe compared with the backscattering of the sphere. Thus, we consider all the measurements including the ones with the sphere located at 0 m s^{-1}.

6.3.2. ANTENNA POINTING CALIBRATION

The verification of antenna pointing is part of weather radar calibration. The coordinates of the sphere in terms of radar should also be checked. We consider another data set measured on May 15, 2018 with a sphere diameter of 20 cm, where the UAV flew at the velocity of 1 m/s with a horizontal zig-zag flight followed by a vertical one. We transform the GPS coordinates to the azimuth and elevation angles in radar line of sight, and output them chronologically (from red points to green points) as shown in Fig. 6.7(a). Since the data were obtained by both a horizontal and vertical zig-zag movement, it can be observed that there are several lines across the 3 dB antenna main beam (indicated as black dash line) along both the azimuth and elevation axis, which is consistent with the designed flight. Those measurements close to the antenna main beam can be used to retrieve the antenna pattern. Accordingly, we calculate the variable $P^I_{r,sp}R^4_{sp}$ as shown in Fig. 6.7(b). From the frequency-domain derived results, several Gaussian-shaped patterns are visible. The left values of Fig. 6.7(b) are from the horizontal movement and the right ones are from the vertical flight. The difference between the maximum power value and the minimum power floor is around 50 dB. This means that the first antenna sidelobes are expected to be visible, but this is not so obvious. This is due to the short staying interval (not enough measurements) when the sphere is located in the antenna sidelobes.

Moreover, all the peaks related to the horizontal movement (left parts) are taken in Fig. 6.7(b) to output them in the azimuth-elevation plane, as shown in Fig. 6.7(c). It is observed that these peaks have very close azimuth angle but their elevation angle vary. Taking all the azimuth angles, the average angle is calculated as 0.1°, which means the offset in azimuth is 0.1°. Similarly, all the peaks from the vertical movement (right parts) are taken in Fig. 6.7(b) and displayed in Fig. 6.7(d). The calculated elevation offset is −0.2°. In addition, the same UAV flight mode is conducted by using a sphere of diameter 18 cm, the calculated azimuth and elevation angle offset is 0.1° and −0.3°, respectively. With the zig-zag horizontally and vertically, it is concluded that the antenna pointing calibration for weather radar can be achieved.

6.3.3. ANTENNA PATTERN FIT

With the radar-based $P^I_{r,sp}R^4_{sp}$ values and their corresponding GPS-based azimuth and elevation angles, it is possible to retrieve the antenna pattern. In the following analysis, all the values of $P^I_{r,sp}R^4_{sp}$ larger than 300 dB are taken for the antenna pattern fitting. Note that the $P^I_{r,sp}R^4_{sp}$ measurements include the two-ways (both transmit and receive) antenna pattern.

Considering the data measured from the horizontal movement on May 15, 2018, the retrieved antenna pattern is shown in Fig. 6.8. As displayed in Fig. 6.8(a), the measured values are indicated by the blue circles, and the 2D triangulation-based linear interpolation is conducted in Matlab using the function named “griddata” as shown in Fig. 6.8(b). The maximum point locates at (0.1°, −0.1°) in the azimuth-elevation plane, as is labeled with a blue filled circle. We recommend to take this angle point as the antenna pointing offset because antenna pointing has an impact on antenna pattern retrieval. Currently, we find that fitting results based on data from either horizontal movement or vertical movement are better than using combined data (both horizontal and vertical ones). In

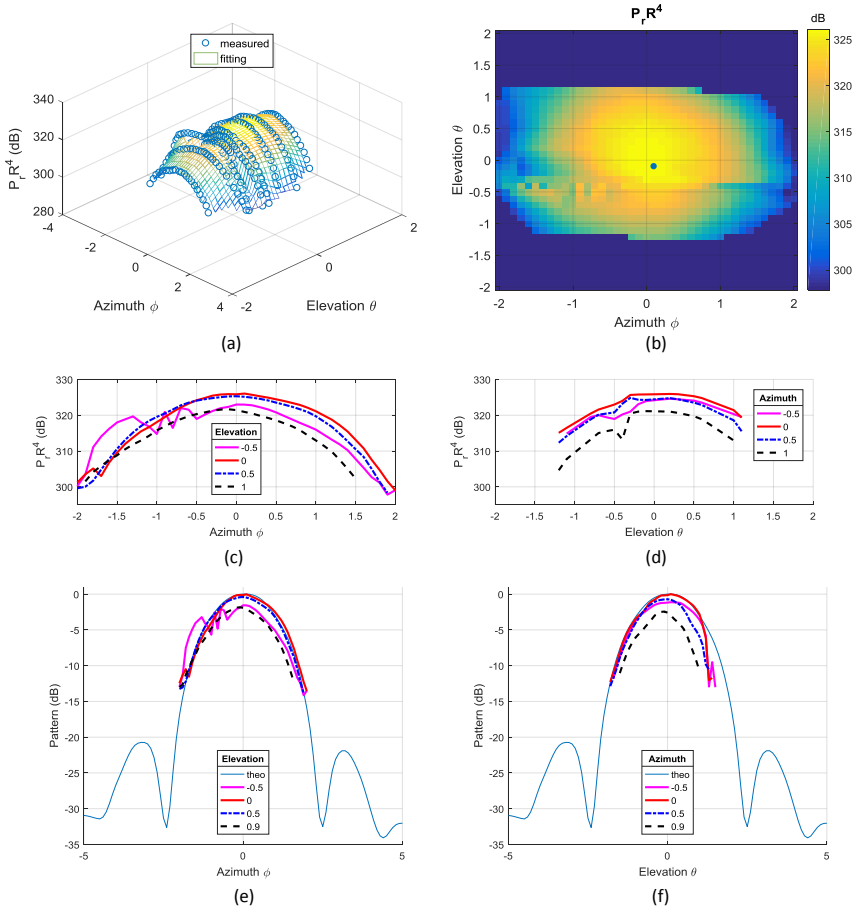

Figure 6.8: 2D antenna pattern fit. (a) 3D view of measured and interpolated values; (b) 2D view of interpolated values; (c) sectional view of interpolated two-way antenna pattern with fixed elevation angles; (d) sectional view of interpolated two-way antenna pattern with fixed azimuth angles; (e) interpolated one-way antenna pattern fits the reference one with fixed elevation angles; (f) interpolated one-way antenna pattern fits the reference one with fixed azimuth angles.

addition, Fig. 6.8(c) and (d) are the sectional views of Fig. 6.8(b) with fixed elevation and azimuth angles, from which near-Gaussian shapes are observed. Compared with Fig. 6.8(d), Fig. 6.8(c) has a larger dynamic range and more complete antenna pattern, which is consistent with more measurements with a fixed elevation angle. Furthermore, to qualitatively compare the antenna patterns (the UAV-aided and transponder-aided), we normalize the two-ways interpolated antenna pattern of Fig. 6.8(c) (more reliable for the horizontal movement), compensate the azimuth offset, and shift it to the reference antenna pattern in Fig. 6.2. The result is displayed in Fig. 6.8(e). Similar work has been done with the vertical movement and the outcome is shown in Fig. 6.8(f). We can observe that the derived antenna pattern fits quite well with the reference one. Since

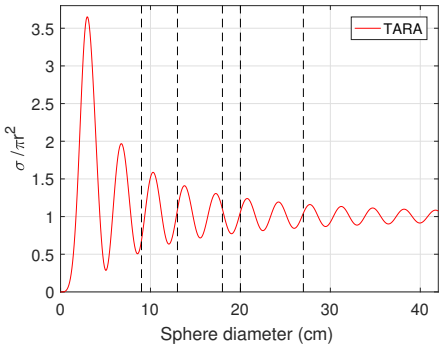

Figure 6.9: Sphere diameters versus normalized RCS of metal sphere for S-band TARA.

TARA is an FMCW radar with separate antennas, the fitting results show that the transmit antenna and receive antenna have a good overlap at the location where the sphere is. However, there are some antenna fitting deviations in the vertical movement, which may be caused by the sphere displacement due to different horizontal wind speed at different heights during the experiment. As is indicated in Fig. 6.7(a), the flying routine of the sphere in the vertical direction is not as straight as that in the horizontal direction.

6.4. EXPERIMENTAL RESULTS AND DISCUSSION

As is mentioned in Section II A, radar constants obtained from different range resolutions differ. In practice, radar calibration experiments require a high range resolution mode. This allows to easily separate the backscattering of the sphere from the backscattering of other targets such as the UAV and the GPS box. With proper adjustment (i.e., estimating the loss-over-range-resolution ratio), the radar constant of the operational mode can be derived from the one of the high range resolution mode. The following discussion is based on the radar measurements obtained in high range resolution (i.e., 3 m).

The relationship between the sphere diameters and the RCS for the TARA wavelength is shown in Fig. 6.9. During the whole experiments, we had spheres of diameter 9 cm, 13 cm, 18 cm, 20 cm and 27 cm, which relate to the Mie scattering region. Different spheres were used in different experiments, and the campaign details and results are shown in Table 6.4. The calibration experiments were conducted for 4 days of the occasional measurements of 7 months, nevertheless several measurements were obtained each day. In Table 6.4, we only list A^I_{UAV} and A^A_{UAV} for the antenna constant, and C^I_{UAV} and C^A_{ref} for the radar constant. The two radar constants represent the proposed calibration technique and the conventional technique (for most radar, the manufacturer does not provide the antenna pattern, but only the specification of the 3 dB beam width).

We started the experiment on October 3 2017 labeled as Case 1, and initially the transmitter power was attenuated with 30 dB to avoid the problem of receiver saturation, however, it turned out to be not a problem with the calibration setting. We introduced a possible error on the attenuation and the sphere signal-to-noise ratio decreased. A large

Table 6.4: Campaign configuration and radar constant calculation.

Case No	Date	Zig-zag direction	Sphere size (cm)	Attenuation (dB)	A^I_{UAV} (dB)	A^A_{UAV} (dB)	C^I_{UAV} (dB)	C^A_{ref} (dB)
1	2017.10.03	horizontal	9	30	32.3	30.8	-205.5	-206.7
		horizontal	13	30	32.3	31.2	-206.0	-207.2
2	2018.03.06	vertical	20	0	32.0	32.1	-201.0	-201.7
		horizontal	20	0	33.1	33.5	-199.8	-201.7
3	2018.04.19	horizontal	20	0	NA	NA	NA	-201.7
		horizontal	20	0	NA	NA	NA	-201.4
		horizontal/vertical	20	0	NA	NA	NA	-202.1
		horizontal	20	0	NA	NA	NA	-201.4
		vertical	27	0	NA	NA	NA	-203.1
		horizontal/vertical	27	0	NA	NA	NA	-203.3
		horizontal/vertical	27	0	NA	NA	NA	-202.4
4	2018.05.15	horizontal	20	0	32.0	32.1	-199.8	-200.6
		vertical	20	0	32.5	32.1	-199.5	-200.8
		horizontal	18	0	32.6	32.5	-200.3	-201.7
		vertical	18	0	32.1	32.1	-201.0	-201.9

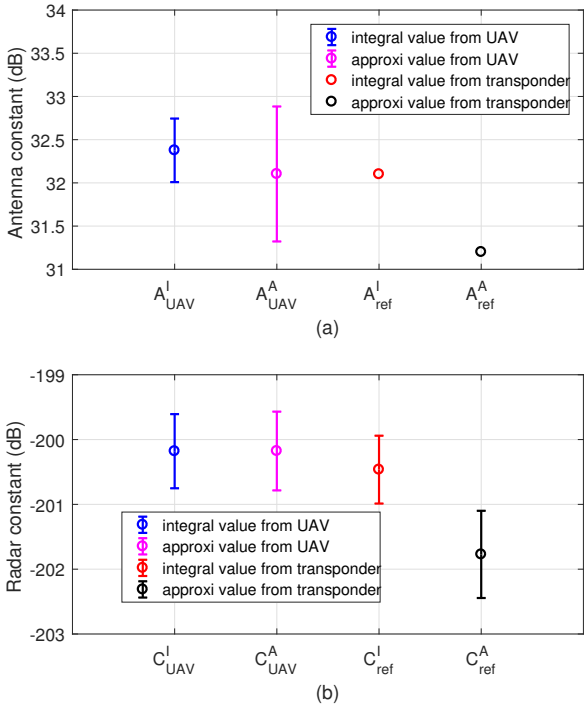

Figure 6.10: Radar constant calculation. (a) antenna constant; (b) radar constant.

difference in the calculated radar constant from other experiments without attenuation has been found. However, the antenna constant of this campaign can still be used to assess the influence of the antenna approximation on the radar constant estimation. In addition, the external GPS box did not work during the experiment on April 19 2018 labeled as Case 3, which impaired the retrieval of the antenna constant A^I_{UAV} and A^A_{UAV}, and radar constant C^I_{UAV} (they are labeled as not available (NA) in the table), but C^A_{ref} could still be calculated.

6.4.1. ANTENNA CONSTANT

As is mentioned in Section 6.2.1, the antenna constant can be obtained from the measurements of UAV and transponder. Note that the experiments measuring the antenna beam pattern by using a transponder was conducted 20 years ago, and unfortunately the data are not available. Based on the report (Aubry and Zijderveld, 1999), we derive the radar antenna pattern as shown in Fig. 6.2. We have $A^I_{ref} = 32.1\,\text{dB}$ and $A^A_{ref} = 31.2\,\text{dB}$ with $\theta_1 = \phi_1$, however, the standard deviation of these measurements can not be provided. Around 1 dB offset exists when the integration is replaced by the approximation using the specified 3 dB beam width in the antenna constant calculation.

In addition, the antenna constants A^I_{UAV} and A^A_{UAV} derived from the UAV measurements can be obtained by the interpolated antenna pattern. Specifically, A^I_{UAV} is calcu-

lated by integrating the interpolated antenna pattern and A^A_{UAV} is calculated by taking the 3 dB beam width of the interpolated antenna pattern. The antenna pattern fitting is based on the data measured either from horizontal movement (more measurements along the azimuth) or vertical movement (more measurements along the elevation). We consider the interpolated azimuth angles using the horizontal movement and the interpolated elevation angles using the vertical movement. Optimally, the horizontal and vertical movement displayed in Fig. 6.7(a) should be implemented to compare the antenna retrieved pattern in azimuth and elevation. This sequence, however, was not carried out in all the cases shown in Table. 6.4. In order to treat all the data the same way, we have to assume the two 3 dB beam width equal. Furthermore, due to the lack of the GPS data in Case 3, all the measurements expect Case 3 are used to calculate A^I_{UAV} and A^A_{UAV}. Note that data from Case 1 are also involved, because the antenna constants are relative values rather than absolute values (e.g., radar constants).

We display A^I_{UAV}, A^A_{UAV}, A^I_{ref}, and A^A_{ref} together in Fig. 6.10(a). The mean of A^I_{UAV} is 32.4 dB and the standard deviation is 0.4 dB, while the mean of A^A_{UAV} is 32.1 dB with a standard deviation of 0.8 dB. The antenna constant A^I_{UAV} has a smaller standard deviation than A^A_{UAV}, which is attributed to the integration decreasing the impact of random variation. Therefore, the integration technique is recommended. The mean differences between UAV derived antenna constants and A^I_{ref} are much less than the differences between UAV derived antenna constants and A^A_{ref}. Such inter-comparison between independent measurements demonstrates the advantage of acquiring antenna pattern measurements rather than using the Gaussian approximation with specified 3 dB beam width (A^A_{ref}). The agreement between A^I_{UAV}, A^A_{UAV} and A^I_{ref} indicates the robustness of the proposed UAV-aided methodology.

6.4.2. RADAR CONSTANT

Before the discussion of the measured radar constants, the theoretical relative error of the radar constant is analyzed using Eq. (6.17). The RCS of the spheres used in the calibration campaigns can be quantified by the anechoic chamber measurements or provided by the manufacturer. Referring to Kent (2001), the measured standard deviation of sphere RCS is 0.25 dB, which corresponds to the relative error 5.9%. In our case, we assume that the relative error of the sphere RCS used in the calibration campaigns is the same. The relative error of R_{sp} can be calculated by using the radar-measured range and the GPS-retrieved one (an example is shown in Fig. 6.6), and its value is estimated to be 0.6%. Note that the calibration campaigns were conducted in the condition of weak wind and no precipitation because as mentioned in Section 6.2.2, the wind will influence the sphere positioning accuracy. As for the relative error of $P^I_{r,sp}$, it is related to the signal to noise ratio (SNR). Recall that all the values of $P^I_{r,sp}R^4_{sp}$ larger than 300 dB are considered for the radar constant calculation, which correspond to SNR larger than 30 dB. So the relative error of $P^I_{r,sp}$ is negligible. Based on the experimental results of Table 6.4, the relative error of A^I_{UAV} is 8.8%. Last but not the least, the relative error of $r_{L\rho}$ can be quantified, similar to that of A^I_{UAV}, by calculating the standard deviation of several measurements. In this research, the target radar constant is obtained for the radar configured in a high range resolution (the same as the one for radar calibration), so $r_{L\rho}$

equals to 1 and its relative error equals to 0. Overall, the relative error of C^I_{UAV} can be calculated based on Eq. (6.17), and the theoretical standard deviation of C^I_{UAV} is 0.45 dB.

Next, the radar constants C^I_{UAV}, C^A_{UAV}, C^I_{ref}, and C^A_{ref}, which are displayed in Fig. 6.10(b), will be discussed. Specifically, the measurements of Case 2 and Case 4 are used to calculate C^I_{UAV}, C^A_{UAV} and C^I_{ref}, while all the data expect Case 1 are used to estimate C^A_{ref}. The mean and standard deviation of C^I_{UAV} are -200.2 dB and 0.6 dB, while that of C^I_{ref} are -200.5 dB and 0.5 dB. In addition, C^A_{UAV} has a mean of -200.2 dB with a standard deviation of 0.6 dB, while C^A_{ref} has a mean of -201.8 dB with a standard deviation of 0.7 dB. It is worth noting that C^I_{UAV}, C^A_{UAV} and C^I_{ref} have close value distributions. Both C^I_{UAV} and C^A_{UAV} are obtained based on the retrieved antenna pattern, and they have close value distributions when the antenna pattern has a Gaussian shape. The reason that C^I_{UAV} and C^I_{ref} have similar value distributions is straightforward: both of them are estimated based on antenna pattern integration and the TARA antenna pattern does not seem to have significantly changed in 20 years. The mean difference between C^I_{UAV} and C^I_{ref} is only 0.3 dB, and that between C^A_{UAV} and C^A_{ref} is 1.6 dB. This further confirmed that the radar constant from the integration is more reliable, namely C^I_{UAV} and C^I_{ref} are more robust than C^A_{UAV} and C^A_{ref}.

All the radar constants have small standard deviation, within 1 dB, which is obtained by the occasional measurements of 7 months. In addition, the spheres used in the experiments have different sizes. These consistencies indicate the reliability of the radar system and no serious anomaly in the RCS of the sphere considered. There is a small difference between the theoretical (0.4 dB) and measured (0.6 dB) standard deviation of C^I_{UAV}. In the analysis of the theoretical standard deviation of C^I_{UAV}, the assumption that the relative error of the sphere RCS is 5.9% is made. When this relative error is increased to 11.7%, the theoretical standard deviation of C^I_{UAV} will also be 0.6 dB. This means that the sphere RCS quantification is necessary for accurate radar calibration.

In summary, these quantitative comparisons and analyses show the good performance of the proposed calibration technique, namely dual GPS information (UAV and GPS box), range separation of the targets, sphere power integration in the range-Doppler domain, and antenna pattern retrieval and integration.

6.5. CONCLUSION

This paper demonstrates a novel external radar calibration technique — UAV-aided radar calibration. The basic principles and the configuration of the calibration experiments are documented, and the S-band radar TARA is used as the to-be-calibrated radar in this work. Specifically, using a UAV to carry a metal sphere with an external GPS box underneath the sphere, the proper flying modes namely horizontal and vertical zig-zag movements are designed to intercept the antenna gain pattern at several points. With the GPS coordinates obtained from the UAV and the external GPS box, it is possible to obtain the positions of the sphere and output its azimuth and elevation angles. Then, the antenna pointing calibration can be conducted. Finally, with the radar and GPS measurements, the interpolated 2D antenna pattern can be retrieved. To quantify the influence of an-

tenna pattern on the radar constant calculation, the antenna constant is defined and it shows that the antenna constant based on the retrieved interpolated antenna pattern is more reliable than the conventional one (i.e., the approximated one). In addition, the calculated radar constants have small standard deviations within 1 dB. These results are based on the usage of different sphere sizes in different experiments. The consistency demonstrates the robustness and effectiveness of the proposed calibration technique.

However, the calibration in this paper is not implemented on weather radar in operational mode (range resolution should be 30 m instead of 3 m). The main reason is due to the legal UAV flying height limitation in the Netherlands. Now specific UAV license application for higher flying heights is in progress, and more calibration tests of weather radar in operational mode can be done in the future. In addition, we propose one way to obtain the radar constant in operational mode derived from the one calculated at high range resolution. The validation of such technique is underway. In addition, the proposed calibration technique can also be used for cloud radars, most of which have narrow beamdwidth (less than 1°) and vertically point to the troposphere. Such work is now under investigation at Site Instrumental de Recherche par Télédétection Atmosphérique (SIRTA) (Haeffelin *et al.*, 2005), Palaiseau, France.

7

CONCLUSION AND RECOMMENDATIONS

This dissertation aims to develop advanced techniques in clutter mitigation and calibration for weather radar to improve radar measurement accuracy, as is outlined in Chapter 1. This work is presented to the radar and remote sensing community to show the latest developments related to weather radar data quality control. Several research questions are stated under the research objectives, which are addressed throughout Chapter 2 - 6. The main findings derived from the research questions are summarized in Section 7.1. Section 7.2 recommends some future work.

7.1. MAIN FINDINGS

Moving clutter mitigation based on low-rank matrix optimization

A technique combining low-rank matrix optimization (LRMO) and a decision tree for single-polarization weather radar to mitigate narrow-band moving clutter and noise is proposed. Similar to the moving object detection in the field of automated video analysis, the proposed separation method, which is carried out in the range-Doppler domain, makes use of different motion variation of radar target and clutter in the spectrogram sequence. The first step in implementing this method is the generation of a range-Doppler spectrogram sequence. Then, the LRMO is applied to the obtained sequence to divide target and moving clutter into foreground and background. The technique is very general but the focus is on narrow-band moving clutter suppression in weather radar. Target and clutter separation in weather radar by using LRMO algorithm has been introduced for the first time. From the foreground sequence which is obtained by solving the LRMO, foreground frequency and spectral width are combined in the decision tree to obtain a filtering mask to mitigate the narrow-band moving clutter and noise.

Narrow-band clutter mitigation based on moving double spectral depolarization ratio filter

The moving double spectral linear depolarization ratio (MDsLDR) filter for full polarimetric weather radar is designed to remove narrow-band clutter (i.e., ground clutter and narrow-band moving clutter) and noise in real-time. The narrow-band clutter observed in the Doppler domain includes: 1) stationary clutter such as ground clutter and 2) non-stationary clutter such as artifacts caused by the radar system itself or external sources. These artifacts are difficult to remove because they are not confined to specific azimuth and range bins. Based on the difference of the spectral polarimetric features and the spectral continuity of precipitation and clutter, the MDsLDR filter generates a filtering mask operating on the range-Doppler spectrogram to remove the clutter and noise, and keep the precipitation. Furthermore, the implementation of the MDsLDR filter requires relatively low computational complexity, so that the MDsLDR filter can be operated in real time.

Clutter mitigation based on object-orientated spectral polarimetric filter

The object-orientated spectral polarimetric (OBSpol) filter for dual-polarization weather radar without cross-polar measurements is put forward to remove narrow-band clutter (i.e., ground clutter and narrow-band moving clutter) and noise in real-time. Based on the spectral polarimetric features and the range-Doppler continuity of precipitation, the OBSpol filter generates a filtering mask operating on the raw range-Doppler spectrogram to mitigate the clutter and noise. The filter can be general and the OBSpol filter is evaluated with radar data contaminated by narrow-band clutter. Additionally, the OBSpol filter is proved to be effective with different Doppler velocity resolutions. This technique can be applied in real-time due to its low computational complexity. The proposed clutter mitigation technique can be implemented for operational dual-polarization weather radar

Radio frequency interference mitigation based on spectral polarimetric filter

Spectral polarimetric filters (SPFs) are put forward to mitigate the radio frequency interference (RFI) for polarimetric weather radar. RFI has become a growing concern for weather radar, distorting radar variable estimation. Observed in the Doppler domain, RFI presents as a raised white noise. The SPFs consist of the moving double spectral linear depolarization ratio (MDsLDR) filter and the object-orientated spectral polarimetric (OBSpol) filter, which have been previously proposed to mitigate narrow-band clutter (both stationary and moving) for polarimetric radar with and without cross-polar measurements, respectively. In this work, these filters are applied to remove the RFI. Based on the spectral polarimetric feature and range-Doppler continuity of precipitation and clutter, the SPFs are implemented in the range-Doppler spectrogram to generate one filtering mask to keep the precipitation and mitigate the clutter.

UAV-aided weather radar calibration

In this thesis, a portable, cost-effective and repeatable radar calibration technique, namely UAV-aided radar calibration is proposed. A UAV serves as stable aerial platform carrying a metal sphere, flying over the radar illumination areas to complete the calibration process. The flying routine of the UAV can be pre-programmed, thus the antenna pattern regarding different elevation and azimuth angles can be retrieved. To obtain the position of the sphere, real-time single-frequency precise point positioning type Global Navigation Satellite System solution is used. In addition, the radar constant is calculated in the range-Doppler domain, and only the data where metal sphere separates from the clutter and other objects are selected. The S-band polarimetric Doppler Transportable Atmospheric Radar (TARA) is used in the calibration campaign. The experiments demonstrate the following results: 1) antenna pointing calibration can be completed; 2) antenna pattern can be retrieved and weather radar constant can be accurately calculated.

7.2. RECOMMENDATIONS

In this section, several recommendations for future research are provided. These recommendations are regarded as the extension of the work presented in the dissertation.

The first research suggestion is to apply the proposed SPFs to mitigate other types of clutter, such as sea clutter and wind turbine clutter. In the thesis, we can conclude that the SPFs can remove both stationary and moving clutter, both narrow-band (i.e., radar artifacts) and broad-band clutter (i.e., radio frequency interference). Due to the complex operational environment of weather radar, it will encounter different types of clutter. It will be very attractive that SPFs can be multi-functional and they can mitigate all clutter and preserve precipitation for weather radar.

The second recommendation is to implement the SPFs in X-band IDRA as the real-time clutter mitigation technique. The narrow-band moving clutter has been an interference of IDRA since its installation. As the performance of SPFs is already proved and the real-time operation capability is verified, the SPFs, specifically the OBSPol filter with sLDR, can replace the current standard processing of IDRA. With such implementation, it can provide radar measurements with better quality for further application.

The third direction is to explore one technique which can recover the clutter-contaminated precipitation in the range-Doppler spectrogram. As is discussed, the limitation of SPFs is that it cannot resolve the problem when clutter and precipitation overlap, which means more precipitation will be removed or extra clutter will be kept. By taking advantage of the autocorrelation of precipitation in the range-Doppler domain, geostatistical interpolation techniques, such as kriging, can be applied. With the help of proper recovery technique, it is possible to preserve complete precipitation information.

The fourth research direction is to adapt the developed UAV-aided radar calibration technique in TARA in the operational mode (range resolution is 30 m instead of 3 m). The solution can be either finding a way to get the scaling factor between two range resolutions, or calibrating TARA in the range resolution of 30 m. The latter depends on

the UAV flying license which is under application now. When the radar calibration is done, more inter-comparison by using light rain (self-consistent method) can be done. In addition, more analysis in differential reflectivity calibration can be conducted.

Last but not least, the proposed calibration technique should be extended to other weather radar systems, such as the horizontally scanning IDRA in Cabauw or other vertically pointing cloud radar systems. Such tests are undergoing at SIRTA, Palaiseau, France within the project of the European Research Infrastructure for the observation of Aerosol, Clouds and Trace Gases (ACTRIS). Two experiments together with colleagues from Institution Pierre Simon Laplace, France, to calibrate W-band cloud radars were already conducted, and more data analysis will be done afterwards.

REFERENCES

I. Douglas, K. Alam, M. Maghenda, Y. Mcdonnell, L. McLean, and J. Campbell, *Unjust waters: climate change, flooding and the urban poor in* Africa, Environment and urbanization **20**, 187 (2008).

S. H. Cannon, J. E. Gartner, R. C. Wilson, J. C. Bowers, and J. L. Laber, *Storm rainfall conditions for floods and debris flows from recently burned areas in southwestern* Colorado *and southern* California, Geomorphology **96**, 250 (2008).

E. Morin, W. F. Krajewski, D. C. Goodrich, X. Gao, and S. Sorooshian, *Estimating rainfall intensities from weather radar data: The scale-dependency problem,* J. Hydrometeorology **4**, 782 (2003).

M. I. Skolnik, *Radar handbook, Third Edition* (McGraw-Hill Education, 1970).

V. Bringi and V. Chandrasekar, *Polarimetric Doppler weather radar: principles and applications* (Cambridge University Press, 2001).

D. Atlas, *Radar calibration: Some simple approaches,* Bull. Amer. Meteorol. Soc. **83**, 1313 (2002).

E. Williams, D. Smalley, *et al.*, *End-to-end calibration of* NEXRAD *differential reflectivity with metal spheres,* in *36th Conf. on Radar Meteorology* (2013).

N. Bharadwaj, K. Widener, L. Andrei, and V. Venkatesh, *Calibration system for* ARM *radars,* in *36th Conf. on Radar Meteorology* (2013).

G. Zhang, *Weather radar polarimetry* (CRC Press, 2016).

D. J. Stensrud, M. Xue, L. J. Wicker, K. E. Kelleher, M. P. Foster, J. T. Schaefer, R. S. Schneider, S. G. Benjamin, S. S. Weygandt, J. T. Ferree, *et al.*, *Convective-scale warn-on-forecast system: A vision for 2020,* Bull. Amer. Meteorol. Soc. **90**, 1487 (2009).

M. Dixon and G. Wiener, *Titan: Thunderstorm identification, tracking, analysis, and nowcasting—a radar-based methodology,* J. Atmos. Ocean. Technol. **10**, 785 (1993).

Y. Wang and V. Chandrasekar, *Quantitative precipitation estimation in the* CASA X*-band dual-polarization radar network,* J. Atmos. Ocean. Technol. **27**, 1665 (2010).

J. Eaves and E. Reedy, *Principles of modern radar* (Springer Science & Business Media, 2012).

M. Nolan, *Fundamentals of air traffic control* (Cengage Learning, 2010).

J. N. Briggs, *Target detection by marine radar* (IET, 2004).

T. D. Crum and R. L. Alberty, *The* WSR-88D *and the* WSR-88D *operational support facility,* Bull. Amer. Meteorol. Soc. **74**, 1669 (Sep. 1993).

P. M. Stepanian, K. G. Horton, V. M. Melnikov, D. S. Zrnić, and S. A. Gauthreaux, *Dual-polarization radar products for biological applications,* Ecosphere **7** (2016).

H. Liu and V. Chandrasekar, *Classification of hydrometeors based on polarimetric radar measurements: Development of fuzzy logic and neuro-fuzzy systems, and in situ verification,* J. Atmos. Ocean. Technol. **17**, 140 (Feb. 2000).

F. Uysal, I. Selesnick, and B. M. Isom, *Mitigation of wind turbine clutter for weather radar by signal separation,* IEEE Trans. Geosci. Remote Sens. **54**, 2925 (May. 2016).

S. M. Torres and D. S. Zrnic, *Ground clutter canceling with a regression filter,* J. Atmos. Ocean. Technol. **16**, 1364 (Oct. 1999).

A. Siggia and R. Passarelli Jr, *Gaussian model adaptive processing (*GMAP*) for improved ground clutter cancellation and moment calculation,* in *European Conf. Radar Meteorol. Hydrol. (ERAD)*, Vol. 2 (2004) pp. 421–424.

D. A. Warde and S. M. Torres, *The autocorrelation spectral density for* D*oppler-weather-radar signal analysis,* IEEE Trans. Geosci. Remote Sens. **52**, 508 (Jan. 2014).

S. Torres, D. Warde, and D. Zrnic, *Signal design and processing techniques for* WSR-88D *ambiguity resolution: Part 15 The* CLEAN-AP *filter*, Tech. Rep. (Nat. Severe Storms Lab., Norman, OK, USA, 2012).

P. M. Stepanian and K. G. Horton, *Extracting migrant flight orientation profiles using polarimetric radar,* IEEE Trans. Geosci. Remote Sens. **53**, 6518 (Dec. 2015).

D. S. Zrnic and A. V. Ryzhkov, *Observations of insects and birds with a polarimetric radar,* IEEE Trans. Geosci. Remote Sens. **36**, 661 (Mar. 1998).

V. Melnikov, M. Leskinen, and J. Koistinen, *Doppler velocities at orthogonal polarizations in radar echoes from insects and birds,* IEEE Geosci. Remote Sens. Lett. **11**, 592 (Mar. 2014).

V. M. Melnikov, M. J. Istok, and J. K. Westbrook, *Asymmetric radar echo patterns from insects,* J. Atmos. Ocean. Technol. **32**, 659 (Apr. 2015).

L. Alku, D. Moisseev, T. Aittomaki, and V. Chandrasekar, *Identification and suppression of nonmeteorological echoes using spectral polarimetric processing,* IEEE Geosci. Remote Sens. **53**, 3628 (Jul. 2015).

J. Yin, O. Krasnov, C. Unal, S. Medagli, and H. Russchenberg, *Spectral polarimetric features analysis of wind turbine clutter in weather radar,* in *11th European Conf. Antennas Propagat. (EUCAP),* (IEEE, Mar. 2017) pp. 3351–3355.

B. Isom, R. Palmer, G. Secrest, R. Rhoton, D. Saxion, T. Allmon, J. Reed, T. Crum, and R. Vogt, *Detailed observations of wind turbine clutter with scanning weather radars,* J. Atmos. Ocean. Technol. **26**, 894 (May. 2009).

L. Norin and G. Haase, *Doppler weather radars and wind turbines,* in *Doppler Radar Observations-Weather Radar, Wind Profiler, Ionospheric Radar, and Other Advanced Applications* (InTech, 2012).

D. Webster, *The effects of wind turbine farms on* ATC *radar*, Tech. Rep. (AWC/WAD/72/665/TRIALS, MAY 05, 2005).

L. Rashid and A. Brown, *Impact modelling of wind farms on marine navigational radar,* in *IET Int. Confer. Radar Syst.* (2007) pp. 1–5.

F. Kong, Y. Zhang, and R. Palmer, *Wind turbine clutter mitigation for weather radar by adaptive spectrum processing,* in *IEEE Radar Conf. (RADAR)* (2012) pp. 0471–0474.

F. Nai, S. Torres, and R. Palmer, *On the mitigation of wind turbine clutter for weather radars using range-*D*oppler spectral processing,* IET Radar, Sonar Navig. **7**, 178 (Feb. 2013).

F. Uysal, I. Selesnick, U. Pillai, and B. Himed, *Dynamic clutter mitigation using sparse optimization,* IEEE Aerosp. Electron. Syst. Mag. **29**, 37 (Jul. 2014).

R. Nepal, J. Cai, and Z. Yan, *Micro-*D*oppler radar signature identification within wind turbine clutter based on short-*CPI *airborne radar observations,* IET Radar, Sonar Navig. **9**, 1268 (Dec. 2015).

A. Huuskonen, E. Saltikoff, and I. Holleman, *The operational weather radar network in* E*urope,* Bull. Amer. Meteorol. Soc. **95**, 897 (Jun. 2014).

E. Saltikoff, J. Y. Cho, P. Tristant, A. Huuskonen, L. Allmon, R. Cook, E. Becker, and P. Joe, *The threat to weather radars by wireless technology,* Bull. Amer. Meteorol. Soc. **97**, 1159 (Jul. 2016).

J. Yin, C. M. Unal, and H. W. Russchenberg, *Narrow-band clutter mitigation in spectral polarimetric weather radar,* IEEE Geosci. Remote Sens. **55**, 4655 (Aug. 2017b).

J. Yin, C. Unal, and H. Russchenberg, *Object-orientated filter design in spectral domain for polarimetric weather radar,* IEEE Geosci. Remote Sens. **57**, 2725 (May, 2019).

O. Krasnov and A. Yarovoy, *Polarimetric micro-*D*oppler characterization of wind turbines,* in *10th European Conf. Antennas Propagat. (EuCAP)* (2016) pp. 1–5.

J. Yin, C. Unal, and H. Russchenberg, *Polarimetric optimization for clutter suppression in spectral polarimetric weather radar,* in *European Radar Conf. (EuRAD)* (2016) pp. 205–208.

G. Liu, Z. Lin, S. Yan, J. Sun, Y. Yu, and Y. Ma, *Robust recovery of subspace structures by low-rank representation,* IEEE Trans. Pattern Anal. Mach. Intell. **35**, 171 (Jan. 2013).

H. Ji, C. Liu, Z. Shen, and Y. Xu, *Robust video denoising using low rank matrix completion.* in *Conf. Comput. Vis. Pattern Recog.(CVPR)* (2010) pp. 1791–1798.

K. Min, Z. Zhang, J. Wright, and Y. Ma, *Decomposing background topics from keywords by principal component pursuit,* in *19th ACM int. conf. on Inf. knowle. manag.* (2010) pp. 269–278.

Y. Peng, A. Ganesh, J. Wright, W. Xu, and Y. Ma, RASL*: Robust alignment by sparse and low-rank decomposition for linearly correlated images,* IEEE Trans. Pattern Anal. Mach. Intell. **34**, 2233 (Nov. 2012).

X. Zhou, C. Yang, and W. Yu, *Moving object detection by detecting contiguous outliers in the low-rank representation,* IEEE Trans. Pattern Anal. Mach. Intell. **35**, 597 (Mar. 2013).

Y. Zhang and T. Xia, *In-wall clutter suppression based on low-rank and sparse representation for through-the-wall radar,* IEEE Geosci. Remote Sens. Lett. **13**, 671 (2016).

S. Z. Li, *Markov random field modeling in image analysis* (Springer Science & Business Media, 2009).

B. Recht, M. Fazel, and P. A. Parrilo, *Guaranteed minimum-rank solutions of linear matrix equations via nuclear norm minimization,* SIAM review **52**, 471 (May. 2010).

J. Figueras i Ventura, *Design of a High Resolution* X*-band* D*oppler Polarimetric Radar*, Ph.D. thesis, Delft Univ. Technol., Delft, The Netherlands (2009).

C. S. Morse, R. K. Goodrich, and L. B. Cornman, *The* NIMA *method for improved moment estimation from* D*oppler spectra,* J. Atmos. Ocean. Technol. **19**, 274 (2002).

J. Y. Cho, *A new radio frequency interference filter for weather radars,* J. Atmos. Ocean. Technol. **34**, 1393 (2017).

A. Melzer, A. Onic, F. Starzer, and M. Huemer, *Short-range leakage cancelation in* FMCW *radar transceivers using an artificial on-chip target,* IEEE J. Sel. Topics Signal Process. **9**, 1650 (Dec. 2015).

J. Hubbert, M. Dixon, and S. Ellis, *Weather radar ground clutter.* P*art* II*: Real-time identification and filtering,* J. Atmos. Ocean. Technol. **26**, 1181 (Jul. 2009a).

C. Stauffer and W. E. L. Grimson, *Adaptive background mixture models for real-time tracking,* in *IEEE Comput. Soc. Conf. Comput. Vis. and Pattern Recog.*, Vol. 2 (IEEE, 1999) pp. 246–252.

S. Fukao, K. Hamazu, and R. J. Doviak, *Radar for meteorological and atmospheric observations* (Springer, 2014) p. 537.

H. L. Groginsky and K. M. Glover, *Weather radar canceller design,* in *19th Conf. Radar Meteorol.*, Vol. 1 (1980) pp. 192–198.

J. Hubbert, M. Dixon, S. Ellis, and G. Meymaris, *Weather radar ground clutter. part* I*: Identification, modeling, and simulation,* J. Atmos. Ocean. Technol. **26**, 1165 (2009b).

R. L. Ice, R. Rhoton, J. Krause, D. Saxion, O. Boydstun, A. Heck, J. Chrisman, D. Berkowitz, W. Zittel, and D. Warde, *Automatic clutter mitigation in the* WSR-88D*, design, evaluation, and implementation,* in *34th Conf. Radar Meteorol., Williamsburg, VA* (2009).

Y. Li, G. Zhang, R. J. Doviak, L. Lei, and Q. Cao, *A new approach to detect ground clutter mixed with weather signals,* IEEE Trans. Geosci. Remote Sens. **51**, 2373 (2013).

Q. Cao, G. Zhang, R. D. Palmer, M. Knight, R. May, and R. J. Stafford, *Spectrum-time estimation and processing (*STEP*) for improving weather radar data quality,* IEEE Trans. Geosci. Remote Sens. **50**, 4670 (2012).

H. S. Park, A. Ryzhkov, D. Zrnic, and K.-E. Kim, *The hydrometeor classification algorithm for the polarimetric* WSR-88D*: Description and application to an* MCS, Weather and Forecasting **24**, 730 (2009).

V. N. Mahale, G. Zhang, and M. Xue, *Fuzzy logic classification of* S*-band polarimetric radar echoes to identify three-body scattering and improve data quality,* J. Applied Meteo. Climato. **53**, 2017 (2014).

D. N. Moisseev and V. Chandrasekar, *Polarimetric spectral filter for adaptive clutter and noise suppression,* J. Atmos. Ocean. Technol. **26**, 215 (2009).

B.-Y. Ye, G. Lee, and H.-M. Park, *Identification and removal of non-meteorological echoes in dual-polarization radar data based on a fuzzy logic algorithm,* Advances in Atmospheric Sciences **32**, 1217 (2015).

P. Joe, J. Scott, J. Sydor, A. Brandão, and A. Yongacoglu, *Radio local area network (*RLAN*) and* C*-band weather radar interference studies,* in *32nd Conf. Radar Meteorol.* (2005).

L. Najman and H. Talbot, *Mathematical morphology* (John Wiley & Sons, 2013).

T. Otto and H. W. Russchenberg, *High-resolution polarimetric* X*-band weather radar observations at the* C*abauw* E*xperimental* S*ite for* A*tmospheric* R*esearch,* Geoscience Data Journal **1**, 7 (2014).

C. Unal, *Spectral polarimetric radar clutter suppression to enhance atmospheric echoes,* J. Atmos. Ocean. Technol. **26**, 1781 (2009).

F. Yanovsky, *Inferring microstructure and turbulence properties in rain through observations and simulations of signal spectra measured with* D*oppler–polarimetric radars,* Polarimetric Detection, Characterization and Remote Sensing , 501 (2011).

F. Yanovsky, *Spectral-polarimetric method of objects and phenomena observation,* in *Proceedings Fifth World Congress "Aviation in the XXI Century*, Vol. 2 (2012) pp. 3–7.

R. J. Doviak and D. S. Zrnic, *Doppler Radar & Weather Observations* (Academic press, 2014).

M. Hagen and P. Meischner, *Estimation of rainfall parameters from polarimetric radar measurements with* POLDIRAD, Physics and Chemistry of the Earth, Part B: Hydrology, Oceans and Atmosphere **25**, 849 (2000).

L. Li, G. M. Heymsfield, P. E. Racette, L. Tian, and E. Zenker, *A 94-GHz cloud radar system on a NASA high-altitude ER-2 aircraft,* J. Atmos. Ocean. Technol. **21**, 1378 (2004).

K. Sato and H. Okamoto, *Characterization of Ze and LDR of nonspherical and inhomogeneous ice particles for 95-GHz cloud radar: Its implication to microphysical retrievals,* J. Geophys. Res.: Atmos. **111** (2006).

R. M. Beauchamp and V. Chandrasekar, *Robust linear depolarization ratio estimation for dual-polarization weather radar,* IEEE Trans. Geosci. Remote Sens. **54**, 1462 (2016).

J. J. Gourley, P. Tabary, and J. Parent du Chatelet, *Data quality of the Meteo-France C-band polarimetric radar,* J. Atmos. Ocean. Technol. **23**, 1340 (2006).

R. Doviak, V. Bringi, A. Ryzhkov, A. Zahrai, and D. Zrnić, *Considerations for polarimetric upgrades to operational WSR-88D radars,* J. Atmos. Ocean. Technol. **17**, 257 (2000).

H. Chen and V. Chandrasekar, *The quantitative precipitation estimation system for Dallas–Fort Worth (DFW) urban remote sensing network,* J. Hydrology **531**, 259 (2015).

H. Chen, V. Chandrasekar, and R. Bechini, *An improved dual-polarization radar rainfall algorithm (DROPS2.0): Application in NASA IFloodS Field Campaign,* J. Hydrometeorology **18**, 917 (2017).

D. Rezacova, Z. Sokol, and P. Pesice, *A radar-based verification of precipitation forecast for local convective storms,* Atmospheric Research **83**, 211 (2007).

H. Huong and A. Pathirana, *Urbanization and climate change impacts on future urban flooding in Can Tho city, Vietnam,* Hydrol. Earth Sys. Sci. **17**, 379 (2013).

A. Hamidi, N. Devineni, J. F. Booth, A. Hosten, R. R. Ferraro, and R. Khanbilvardi, *Classifying urban rainfall extremes using weather radar data: an application to the Greater New York Area,* J. Hydrometeorology **18**, 611 (2017).

T. F. Stocker, D. Qin, G.-K. Plattner, M. Tignor, S. K. Allen, J. Boschung, A. Nauels, Y. Xia, V. Bex, P. M. Midgley, *et al.*, *Climate change 2013: The physical science basis,* Intergovernmental Panel on Climate Change, Working Group I Contribution to the IPCC Fifth Assessment Report (AR5)(Cambridge Univ Press, New York) (2013).

J. Yin, C. Unal, M. Schleiss, and H. Russchenberg, *Radar target and moving clutter separation based on the low-rank matrix optimization,* IEEE Trans. Geosci. Remote Sens. **56**, 4765 (2018).

S. Bachmann and D. Zrnić, *Spectral density of polarimetric variables separating biological scatterers in the vad display,* J. Atmos. Ocean. Technol. **24**, 1186 (2007).

I. R. Ivić, C. Curtis, and S. M. Torres, *Radial-based noise power estimation for weather radars,* J. Atmos. Ocean. Technol. **30**, 2737 (2013).

P. Soille, *Morphological image analysis: principles and applications* (Springer Science and Business Media, 2013).

R. Fisher, S. Perkins, A. Walker, and E. Wolfart, *Connected Components Labeling,* (2018).

U. C. Benz, P. Hofmann, G. Willhauck, I. Lingenfelder, and M. Heynen, *Multi-resolution, object-oriented fuzzy analysis of remote sensing data for* GIS *-ready information,* ISPRS J. Photogram. Remote Sens. **58**, 239 (2004).

C. Unal and D. Moisseev, *Combined* D*oppler and polarimetric radar measurements: Correction for spectrum aliasing and nonsimultaneous polarimetric measurements,* J. Atmos. Ocean. Technol. **21**, 443 (2004).

ITU-R Resolution 229, *Use of the bands 5150-5250*MHz*, 5250-5350*MHz *and 5470-5725*MHz *by the mobile service for the implementation of wireless access systems including radio local area networks.* (2003).

P. Tristant, RLAN *5* GHz *interference to* C*-band meteorological radars in* E*urope: solutions, lessons, follow-up,* in *Proc. 34th AMS Radar Conf. Radar Meteorol.* (2009).

J. E. Carroll, F. H. Sanders, R. L. Sole, and G. A. Sanders, *Case Study: Investigation of Interference Into 5* GHZ *Weather Radars from Unlicensed National Information Infrastructure Devices,* Tech. Rep. (US Department of Commerce, National Telecommunications and Information Administration, 2010).

J. Lake, M. Yeary, and C. Curtis, *Adaptive radio frequency interference mitigation techniques at the national weather radar testbed: First results,* in *IEEE Radar Conf.* (IEEE, 2014) pp. 0840–0845.

Vaisala, *User's manual:* RVP900 *digital receiver and signal processor,* , 513 (2016).

M. A. Richards, J. Scheer, W. A. Holm, and W. L. Melvin, *Principles of modern radar* (Citeseer, 2010).

L. Rojas, D. N. Moisseev, V. Chandrasekar, J. Sezler, and R. Keränen, *Dual-polarization spectral filter for radio frequency interference suppression,* (European conf. Radar Meteorol. Hydrol. (ERAD), 2012).

KNMI radar specifications, (2018a).

Precipitation map from KNMI weather radars, (2018).

KNMI Data, (2018b).

Selex ES *signal processor,* (2018).

V. M. Melnikov and D. S. Zrnić, *On the alternate transmission mode for polarimetric phased array weather radar,* J. Atmos. Ocean. Technol. **32**, 220 (2015).

F. J. Meyer, J. B. Nicoll, and A. P. Doulgeris, *Correction and characterization of radio frequency interference signatures in* L*-band synthetic aperture radar data,* IEEE Trans. Geosci. Remote Sens. **51**, 4961 (2013).

T. Fawcett, *An introduction to roc analysis,* Pattern recognition letters **27**, 861 (2006).

E. N. Anagnostou, C. A. Morales, and T. Dinku, *The use of* TRMM *precipitation radar observations in determining ground radar calibration biases,* J. Atmos. Ocean. Technol. **18**, 616 (2001).

H. Russchenberg and J. Yin, *Deliverable* D*2.3: Radar calibration and standardization concepts,* in *Aerosol, Clouds, and Trace gases (ACTRIS) workshop* (2015) pp. 1–7.

J.-S. Suh, L. Minz, D.-H. Jung, H.-S. Kang, J.-W. Ham, and S.-O. Park, *Drone-based external calibration of a fully synchronized* K*u-band heterodyne* FMCW *radar,* IEEE Trans. Instrum. Meas. **66**, 2189 (2017).

S. Duthoit, J. L. Salazar, W. Doyle, A. Segales, B. Wolf, C. Fulton, and P. Chilson, *A new approach for in-situ antenna characterization, radome inspection and radar calibration, using an unmanned aircraft system (*UAS*),* in *IEEE Radar Conf.* (IEEE, 2017) pp. 0669–0674.

P. Aubry and J. Zijderveld, TARA *reflector radiation pattern measurements*, Tech. Rep. (International Research Center for Telecommunication and Radar, Delft, the Netherlands, 1999).

P. F. de Bakker and C. C. Tiberius, *Real-time multi*-GNSS *single-frequency precise point positioning,* GPS Solutions **21**, 1791 (2017).

B. M. Kent, *Comparative measurements of precision radar cross section (*RCS*) calibration targets,* in *Antennas and Propagation Society International Symposium, 2001. IEEE*, Vol. 4 (IEEE, 2001) pp. 412–415.

M. Haeffelin, L. Barthès, O. Bock, C. Boitel, S. Bony, D. Bouniol, H. Chepfer, M. Chiriaco, J. Cuesta, J. Delanoë, *et al.*, SIRTA*, a ground-based atmospheric observatory for cloud and aerosol research,* in *Annales Geophysicae*, Vol. 23 (2005) pp. 253–275.

ACKNOWLEDGEMENTS

The moment that I am going to finalize my thesis finally comes! It is a great pleasure to express my gratitude to those who have helped me during my PhD journey.

Foremost, I would like to thank my promoter Herman who gave me this chance to do the research in the group. Herman is willing to give full freedom to his PhD students, and he is always there to help if you encounter any problems. I took full advantage of this, starting with discussing one well-known weather radar monograph chapter by chapter, then giving me feedback on my research progress, introducing right persons to speed up the research and experiments, etc. Every meeting with him was enjoyable, in which I always benefited from his knowledge and insights. Special thanks go to my daily supervisor, Christine as well! Christine is so nice and patient, and she guided me on how to do research hand by hand. Her profession and carefulness helped me publish smoothly. We cooperated in harmony. She assisted me a lot in English proofreading for each word and sentence, which was a big favor for a Chinese researcher. However, this also biased and decreased her English level. I am sorry about this! Thanks, Christine, for treating me like a friend and family. I learn a lot from you.

The thesis would not be a success without the support of Peter. Without his selfless assistance in my research, I am afraid I can not have the "RFI" paper and "calibration" paper. Peter is now an emeritus professor in our department, and I started to "bother" him in October 2017, after when I talked to him weekly. It was very productive to work and discuss together with Peter. He always inspired me, guided me and sometimes provided the possible solutions! These moments being together were enjoyable and unforgettable. I also appreciate the help from Marc who is enthusiastic and knowledgeable. Marc gave me a lot of useful suggestion to modify the paper we cooperated, and even helped me to prepare one letter to the editor to respond to one of the reviewers who insisted that the novelty of the paper was not sufficient. His inputs and efforts are greatly appreciated. In addition, I am grateful to Fred who helped me a lot in the field experiments. We went to Cabauw 10 times for weather radar calibration and Palaiseau 3 times for cloud radar calibration, bringing his lovely toy — the DJI micro-drone hexacopter. The experimental work of radar calibration cannot be completed with the assistance of the excellent technician! Thanks, Fred.

I would like to thank my colleagues from the ATMOS Group: Ricardo, Dimitra, Yunlong, Lukas, Igor, Yann, Julien, Christos, Albert; from the GRS Department: Reenu, Marcel, Thomas, Gert, Floris, Veronica, Taco, Karen, Stephanie, Lorenzo, Monica, Edouard, Vincent, Prabu, Antoon, Steven, Jonathan, Raymond, Kevin, Mariska, Beatrice, Laura, Elyta, Jinliang, Xiaojun, Han, Kaixuan, Ling, Yuanhao, Yueqian, Mengshi, Jie, Haolu, Junchao, Yerong, Jinhu, Yu, Hao, Fengming, Hongyang, Bowen, Weiran and more; from the MS3 group: Oleg and Faruk. Also special thanks to Minke, Debbie, Lidwien, Suzanne for

the administrative assistance. I am so lucky to have all of you around on the campus.

The greatest gift of life is friendship, and many friends around make my oversea life colorful. Laobing, Xingxing, Shuai, Pengling, Hai, Weijian, Yamin, Lingying, Jian, Xiang, Yue, Shanshan, Jintao, Yazhou, Siqi, Mingxin, Yu, Shilong, Shengzhi, Nannan, Jianping, Da, Huan, Xiaoxiao, Bingying and others, I cannot list all of your names here but I do remember all of you, and thanks to your companion.

We may have our differences, but nothing is more important than family. Thanks to my parents and parents-in-law for their selfless support and truly love. My mother, Mrs. Huang Yuechai and mother-in-law, Mrs. Li Huan took turns to come to the Netherlands to help us to take care of our newly-born daughter. I sincerely appreciate this huge favor. Elly, my little girl, thanks for your coming, giving me more excuses to stay with you and stopping working in spare time. Yuan, my lovely wife, thanks for being around all the time. I met you on May 14, 2011 and fell in love with you at first sight! You went to Aachen, Germany for your master degree in August 2012 and we separated in different continents for 2 years. In September 2014, when I started my PhD in Delft, I traveled to Aachen every weekend to visit you. The east-to-west journey lasted for one year until you found your first job in Groningen, the Netherlands after when the trip became the north-to-south for another year. Eventually, you decided to move back to Delft, and we got married and built our small home. I cannot imagine how my life will be without your companion all these years. Grow old along with me, the best is yet to be!

Jiapeng

Delft, January 2019

CURRICULUM VITÆ

Jiapeng YIN

Jiapeng was born on May 29, 1990, Zhejiang Province, China. He received his BSc degree in Information Engineering in 2012 from National University of Defence Technology. In 2012, he started his MSc degree and was recommended to start his Ph.D. program ahead of time due to his excellent performance in 2014. In 2014, Jiapeng was awarded a 4-year scholarship from the China Scholarship Council to pursue his Ph.D. in the Delft University of Technology (TU Delft), the Netherlands. From September 2018, he is a post-doc researcher at TU Delft, working on cloud radar calibration.

His research interests include radar polarimetry, polarimetric weather radar, radar signal processing and radar calibration.

JOURNAL PUBLICATIONS

1. **Jiapeng Yin**, Christine Unal, Herman Russchenberg. Narrow-band Clutter Mitigation in Spectral Polarimetric Weather Radar. *IEEE Trans. Geosci. Remote Sens.*, 55(8):4655-4667, 2017.

2. **Jiapeng Yin**, Christine Unal, Marc Schleiss, Herman Russchenberg. Radar Target and Moving Clutter Separation based on the Low-rank Matrix Optimization. *IEEE Trans. Geosci. Remote Sens.*, 56(8):4765-4780, 2018.

3. **Jiapeng Yin**, Christine Unal, Herman Russchenberg. Objected-orientated Filter Design in Spectral Domain for Polarimetric Weather Radar. *IEEE Trans. Geosci. Remote Sens.*, 57(5):2725-2740, 2019.

4. **Jiapeng Yin**, Peter Hoogeboom, Christine Unal, Herman Russchenberg. Radio Frequency Interference Characterization and Mitigation for Polarimetric Weather Radar. *IEEE Trans. Geosci. Remote Sens.*, Under review.

5. **Jiapeng Yin**, Peter Hoogeboom, Christine Unal, Herman Russchenberg, Fred van der Zwan, Erik Oudejans. UAV-aided Weather Radar Calibration. *IEEE Trans. Geosci. Remote Sens.*, Under review.

6. Yabin Gou, Yingzao Ma, Haonan Chen, **Jiapeng Yin**. Utilization of a C-band Polarimetric Radar for Severe Rainfall Event Analysis in Complex Terrain over Eastern China. *Remote Sens.* 2019,11(1):22.

CONFERENCE PUBLICATIONS

1. Herman Russchenberg, **Jiapeng Yin**. Deliverable D2.3: Radar Calibration and Standardization Concepts. ACTRIS Cloud Radar Calibration Workshop, 28 - 29 September 2015, Cologne, Germany.

2. **Jiapeng Yin**, Christine Unal, Herman Russchenberg. Polarimetric Optimization for Clutter Suppression in Spectral Polarimetric Weather Radar. 13th European Radar Conference (EuRAD), 3 - 7 October 2016, London, UK.

3. **Jiapeng Yin**, Oleg Krasnov, Christine Unal, Stefano Medagli, Herman Russchenberg. Signatures Study of Wind Turbine Clutter in Polarimetric Doppler Weather Radar. Specialist Meeting about Electromagnetic Waves and Wind Turbines, 6 -7 December 2016, Fraunhofer FHR, Wachtberg, Germany.

4. **Jiapeng Yin**, Oleg Krasnov, Christine Unal, Stefano Medagli, Herman Russchenberg. Spectral Polarimetric Features Analysis of Wind Turbine Clutter in Weather Radar. 11th European Conference on Antennas and Propagation (EuCAP), 19-24 March 2017, Paris, France. (**Best Paper Finalist**)

5. **Jiapeng Yin**, Christine Unal, Herman Russchenberg. Object-based Filter Design for Spectral Polarimetric Weather Radar. 38th AMS Conference on Radar Meteorology, 28 August - 1 September 2017, Chicago, USA.

6. **Jiapeng Yin**, Fred van der Zwan, Erik Oudejans, Christine Unal, Herman Russchenberg. UAV-based Absolute Radar Calibration. 38th AMS Conference on Radar Meteorology, 28 August - 1 September 2017, Chicago, USA.

7. **Jiapeng Yin**, Fred van der Zwan, Erik Oudejans, Christine Unal, Herman Russchenberg. UAV-aided Absolute Calibration of Weather Radar. Weather Radar Calibration Workshop, 18 - 20 October 2017, Deutscher Wetterdienst DWD, Offenbach, Germany.

8. **Jiapeng Yin**, Fred van der Zwan, Erik Oudejans, Christine Unal, Herman Russchenberg. UAV-aided Absolute Radar Calibration. 3rd ACTRIS-2 WP2 Workshop, 13 - 17 November 2017, Delft, the Netherlands.

9. **Jiapeng Yin**, Christine Unal, Herman Russchenberg. Object-orientated Filter Design in Spectral Domain for Polarimetric Weather Radar. The International Workshop on Small Weather Radars, 6 - 8 June 2018, Colorado, USA.

10. **Jiapeng Yin**, Fred van der Zwan, Erik Oudejans, Peter Hoogeboom, Christine Unal, Herman Russchenberg. UAV-aided Weather Radar Calibration. 10th European Conference on Radar in Meteorology and Hydrology, 1 - 6 July 2018, The Netherlands.

11. **Jiapeng Yin**, Christine Unal, Herman Russchenberg. Specrtral Polarimetric Filters Design for Broad-band Weather Clutter Mitigation. 10th European Conference on Radar in Meteorology and Hydrology, 1 - 6 July 2018, The Netherlands.

12. Felipe Toledo, **Jiapeng Yin**, Julien Delanoe, Jean-Charles Dupont, Martial Haeffelin, Herman Russchenberg. Center for Cloud Remote Sensing: Doppler Cloud Radar Calibration Campaign. 10th European Conference on Radar in Meteorology and Hydrology, 1 - 6 July 2018, The Netherlands.

13. **Jiapeng Yin**, Fred van der Zwan, Erik Oudejans, Peter Hoogeboom, Christine Unal, Herman Russchenberg. UAV-aided Weather Radar Calibration. ACTRIS Cloud Radar Calibration Workshop, 29 - 30 November 2018, Paris, France.

14. **Jiapeng Yin**, Christine Unal, Herman Russchenberg. Spectral Polarimetric Filter Design for Wind Turbine Clutter Suppression. Specialist Meeting about Electromagnetic Waves and Wind Turbines, 6 -7 December 2018, Delft, The Netherlands.